UNIVERSITY OF TOYAMA

A dissertation

submitted to the Graduate school of science and engineering

Department of Nano and functional material sciences

University of Toyama, Japan

In partial fulfilment of the requirements

for the degree of

Doctor of Philosophy

September 2024

Strong nonlinear phenomena in resonant tunneling diode oscillators and their effects on the frequency delta sigma modulation sensors

by

Umer Farooq

Supervised by

Professor Koichi Maezawa

Professor Masayuki Mori

Abstract

Terahertz (THz) waves, also known as T-rays, have attracted a great deal of attention in recent years because of their potential applications in high-speed wireless communications, biomedical imaging and diagnostic, security, and pharmaceutical fields. The THz region in the electromagnetic spectrum is usually referred to as an unexplored region, primarily due to the technological challenges of practically realizing the THz sources. Currently, many devices that generate and detect THz waves are being actively researched. Among them, one of the most promising devices is the resonant tunneling diode (RTD) which is a nano-scale quantum effect semiconductor device for the THz frequency range. Its unique current-voltage (IV) characteristics exhibit negative differential resistance (NDR) at room temperature, where the current decreases as the voltage increases. This NDR serves as the foundation for oscillators, and 1.98 THz oscillation has already been reported employing RTD. Most of the research on RTD oscillators is primarily focused on radio communication applications, but since the THz band has a distinctive absorption spectrum to molecules, illicit drugs, cancer cells, gases, and drugs, sensor applications in various fields are also promising. Sensors that use RTD oscillators to detect frequency changes due to external parameters have already been proposed and demonstrated. These sensors employ the frequency delta-sigma modulation technique (FDSM), which allows for measuring frequency changes with ultrahigh dynamic range and wide bandwidth. However, to take advantage of the FDSM, several challenges need to be addressed, as described below.

It is important to note that RTD is a two-terminal device, which has an inherent drawback. It makes the behavior of the RTD oscillators highly sensitive to minor parasitic effects resulting in frequency fluctuation and spurious oscillations. Also, nonlinear IV characteristics provide the

foundation for generating nonlinear phenomena known as chaos. Chaotic signals have a noise-like appearance, but they are deterministic. In fact, Chaos itself has a broad range of applications in secure communication, signal processing, image encryption, and chaos-based mobile robots. However, chaos is an undesired phenomenon in many applications to impedes proper operation. In particular, the nonlinearities of RTD oscillators can pose challenges in implementing them for sensor applications.

The purpose of this research is to investigate the nonlinear phenomena in RTD oscillators and their impact on FDSM sensors. First, the nonlinear phenomena in RTD oscillators were investigated extensively by applying an external sinusoidal signal while operating the RTD in its NDR region. Under these conditions, the device's response is highly nonlinear, resulting in complex chaotic behavior. The frequency range in this study is higher than the microwave frequencies, so that, the chaotic signals are essential to observe on a sampling oscilloscope. For this, a periodic reset mechanism was adopted to output an identical chaos signal. Though this mechanism was shown to be effective in previous papers, the length of the waveforms to observe was limited to a rather short period, and it was unclear if this technique could be used for the detailed characterization of such high-frequency chaos. In this study, the circuit design was improved to observe longer waveforms, and demonstrated that detailed characterization of the circuit’s nonlinearities is possible using this periodic resetting technique (PRT) with a sampling oscilloscope.

Secondly, the behavior of RTD oscillators was studied when a transmission line (TL) stub was added. The TL stub acts as a delayed feedback unit, resulting in unstable and complex oscillation behavior including chaos. The complex oscillations in the experiments were successfully observed by implementing the improved PRT described earlier. Thus, these circuits work as simple chaos generators with potential applications in the THz frequency range. On the other hand, this finding

is also significant for designing RTD oscillators for THz sensors, since even a small metal pattern can cause such an unwanted feedback effect in the THz frequency range that can impede sensor performance.

While considering the nonlinear effects discussed earlier, the scanning near-field terahertz microscope (SNFTM) was proposed as a promising application of FDSM sensors using RTD oscillators. The simulation results of the SNFTM circuit showed how the effects of the TL can interfere with the proper operation of such sensors. Another difficulty in implementing SNFTM is that the direct sampling of THz signals is not possible because the FDSM relies on ultra-high frequency sampling. To overcome this difficulty, two ways of down-converting the THz signals using the RTDs as sampler/mixer are proposed and demonstrated their working by performing simulation. Finally, to verify the basic working principle of the SNFTM experimentally, a prototype device was fabricated in the microwave frequency region for ease of measurement. A very clear image of Phoenix-Hall was obtained by scanning the surface of a 10-yen coin. It was demonstrated that a high-resolution image beyond the diffraction limit can be obtained with this prototype device.

In conclusion, the improved circuit design of PRT contributed to providing profound insight into the nonlinearities that occurred in RTD oscillators when subjected to externally applied sinusoidal signals, and a TL stub was added. While effectively dealing with nonlinearities associated with RTD oscillators, the results of SNFTM imply the potential of the RTD oscillators for realizing the unprecedented THz sensors in conjunction with a superior FDSM AD conversion technique.

Contents

Chapter 1 Introduction

1.1 Introduction

Terahertz (THz) waves, also known as T-rays [1], have attracted a great deal of attention in recent years because of their potential applications in high-speed wireless communications, biomedical imaging and diagnostic, security, and pharmaceutical fields [2–8]. The THz region in the electromagnetic spectrum is usually referred to as an unexplored region [9], primarily due to the technological challenges of practically realizing the THz sources [10]. Currently, many devices that generate and detect THz waves are being actively researched [11]. Among electronic devices, one of them is the resonant tunneling diode (RTD) which is a quantum effect semiconductor device for the THz frequency range [12]. It exhibits unique nonlinear IV characteristics showing a negative differential resistance (NDR), where current decreases by increasing voltage. These nonlinear IV characteristics are the basis for oscillator circuits and oscillations of 1.98 THz have already been confirmed with RTD oscillators [13]. So far, the RTD oscillators research is more focused on radio communication applications [14–16], but sensor applications are also promising.

On the other hand, RTD nonlinear dynamics owing to inherent nonlinear IV characteristics can lead to chaos upon interaction with external unwanted/unavoidable signals or parasitic effects. This chaotic phenomenon of RTD oscillators can be both a challenge and an opportunity. While chaotic signals, which look like noise but are deterministic in nature [17], [18], have broad applications in secure communications and signal processing [19–24], but can impede the performance of the sensors as well as conventional radio communication.

The purpose of this research is to investigate the nonlinear phenomena in RTD oscillators and their impact on sensors. In this study, I focus on the frequency delta-sigma modulation (FDSM) type sensors as an application of the RTD oscillators. FDSM is a promising analog-to-digital (AD) conversion technique that allows for measuring frequency changes with ultrahigh dynamic range and wide bandwidth [25–28]. Using RTD oscillators for sensing frequency change in response to external physical parameters has significant advantages in realizing high-performance sensors with numerous applications.

In this chapter, the significance of THz waves for a wide range of applications and THz sources are discussed. It also describes why RTD is a promising candidate as a potential THz source. Also, the purpose of this research and thesis is outlined in the final section.

1.2 THz waves and their applications

Electromagnetic waves cover a wide spectrum of frequencies, each with distinct properties and applications. Depending on the frequency, there are regions with the characteristics of light waves and radio wave regions that are transparent. Among them, THz waves are electromagnetic waves in the frequency band of 100 GHz to 10 THz [29–34]. In terms of wavelength, it ranges from 3 mm to 30 μm which is a region sandwiched between millimeter waves and infrared rays as shown

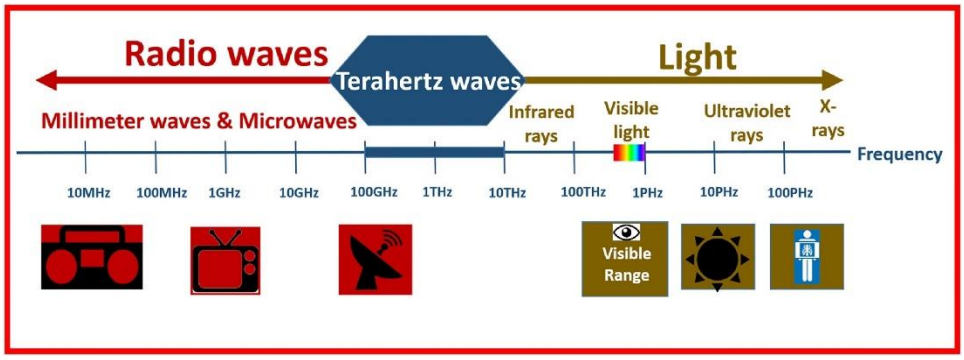

Figure 1.1 Electromagnetic spectrum depicting the THz region (Adopted from [251] *)*

in Fig. 1.1. Mostly, THz waves have wavelengths less than 1 mm, hence they are often referred to as submillimeter waves. Furthermore, the upper limit of the THz frequency range is also referred to as far infrared.

THz waves have photon energy from 0.4 to 40 meV which is very less as compared to the X-ray photon energy which ranges from 100 eV to several tens keV [35]. This lower photon energy level of THz waves does not cause ionization, making them safe for human medical diagnostic and treatment [36]. Additionally, their low photon energy level makes them well-suited for non-destructive and non-invasive inspection applications [37].

THz waves possess a unique characteristic of interacting with molecules [38–41]. Their electric fields exhibit strong interactions with polar molecules like H_2O_2, CO_2, O_2, and N_2. This strong interaction with polar molecules, especially water molecules, results in significant atmospheric attenuation during free space propagation [42]. Consequently, THz waves are suitable for short to medium-range applications [43], [44] So, this characteristic also makes THz waves valuable for spectroscopy applications [45], [46].

However, THz waves lack interaction with non-polar materials such as paper, clothing, and plastic, enabling them to penetrate through such substances [47], [48]. Penetrating through these non-conductive materials, paving the way for THz imaging [5], [49], [50] that can be used for inspection [51]. THz waves provide superior spatial resolution than microwaves and millimeter waves due to their shorter wavelength. THz imaging is expected to provide higher resolution than millimeter waves [5]. As previously stated, THz waves are safe for human usage due to their low photon energy, hence THz imaging can be employed in a variety of body-scanning applications [7], [52], including medical diagnostics [4] and security scanning [53]. One of the significant achievements of THz imaging is the capability of imaging and sensing non-invasive cancer

detection [6], [54–56]. THz technology is also gaining popularity in the information and communication field because of its tens and hundreds of gigahertz bandwidths available and low health risks [2]. As millimeter-wave communication technologies are already mature, research is shifting to THz wireless communication [3], [57], [58]. Initially, the generation of THz waves was possible with bulky, costly, and high-power consumption systems which were a huge hindrance to the widespread commercialization of this technology [59]. A wide range of THz wave applications in numerous fields have attracted the attention of the scientific community to realize an inexpensive, efficient, and compact THz source.

1.3 THz sources

Many efforts have been made to fill the THz gap which resulted in the investigation and proposal of numerous THz source candidates [60]. Since the THz range is sandwiched between light and

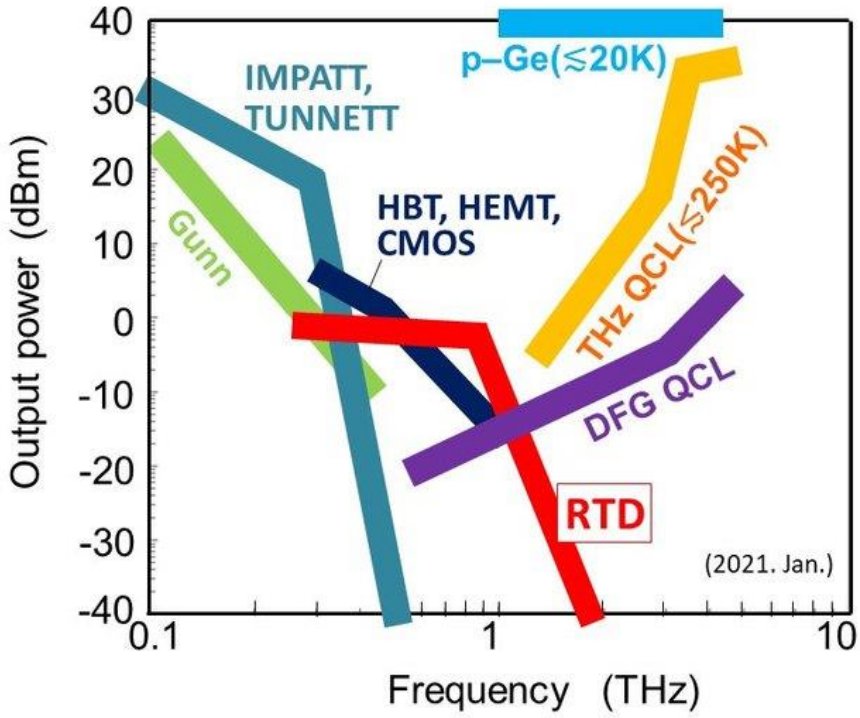

Figure 1.2 Status of semiconductor on-chip devices capable of generating THz waves. Devices that do not have a temperature indicator run at room temperature. (Adopted from [252] *)*

radio waves. So, its generation is possible with both photonic and electronic oscillators [61]. Initially, THz waves were generated primarily by photonic technology. Photonic-based THz generators provide tremendous output power, such as free electron lasers [62], [63], gas lasers [64], backward-wave oscillators [65–67], gyrotrons [68], [69], and uni-traveling carrier photodiodes (UTC-PD) [70], [71]. These sources have aided research in exploring the vast THz applications. However, their bulky size and expensive manufacturing cost restrict them from employment in commercial THz applications.

With recent advancements in the field of semiconductor fabrication techniques, several potential THz source candidates have been reported. Because of their compact size and simplicity of mass production, semiconductor THz source candidates, including both photonic and electronic techniques, have recently received substantial attention. Figure 1.2 summarizes the status of semiconductor THz source candidates [72] which can generate THz waves employing a DC power source. Here, the THz sources that need external microwave or light sources in order to generate THz waves are excluded.

In the field of developing THz optical devices, research has been focused on p-germanium (p-Ge) lasers [73] and quantum cascade lasers (QCL) [74–78]. However, low/cryogenic temperature is required for their operation. Recently, room-temperature THz sources based on mid-infrared QCLs with differential frequency generation have been reported [79–82] but still challenging its continuous wave operation. Electronic devices that have been studied as THz sources include impact ionization avalanche transit-time (IMPATT) diodes [83], tunnel transit time (TUNNET) diodes [84], and Gunn diodes [85], [86]. Although the output power of these devices is high, these electronic devices still need an efficient heatsink method for their optimal performance.

Furthermore, these diodes have lower oscillation frequencies compared to other electronic devices, such as transistor-based and RTD-based oscillators.

Subsequently, electronic transistor-based oscillators as THz sources include high electron mobility transistors (HEMT) [87], [88], heterojunction bipolar transistors (HBT) [89–91], and complementary metal oxide semiconductor (CMOS) transistors [92]. The output power and frequency are still lower than RTD-based oscillators, but it is expected to increase further which makes them promising candidates for commercial THz sources.

1.3.1 Resonant tunneling diode

Reviewing above mentioned THz sources, RTD oscillators have the highest oscillation frequency among electronic oscillators. RTDs are potential candidates for THz sources featuring room temperature operation [93–100]. At present, oscillations up to 1.98 THz at room temperature have been realized [13], and oscillations up to 2.77 THz are expected [101], while higher frequency and high output power structures are being investigated [101], [102]. A single RTD-based oscillator can be realized on a millimeter-sized chip [103]. The output power up to 0.4mW at 530-590 GHz employing a single RTD-oscillator [104], and a large-scale array configuration of RTD oscillators generate 0.73 mW at 1 THz has already been reported [105]. The DC-RF conversion efficiency in the terahertz band is approximately 1% [104].

1.3.1.1 RTD development stages

The RTD concept was first proposed by R. Tsu and L. Esaki in 1973 [106] as a finite superlattice, and then experimentally observed in GaAs-AlGaAs double-barrier heterostructures at low temperatures [107]. M. Tsuchiya et al. first demonstrated a practically important operation at room temperature in 1985 [108], paving the way for a new research field.

Since then, the development of RTD oscillators has been updated, reaching an operating frequency of 712 GHz in 1991 [109]. A new era of RTD oscillator development began when the oscillation frequency reached 831 GHz in 2009 [110] and 1 THz in 2010 [111]. Subsequently, by structural optimization, the highest oscillation frequency was updated to 1.31 THz [112], 1.46 THz [113], 1.55 THz [114], 1.92 THz [115], and 1.98 THz [13]. In addition, the frequency tuning capabilities of RTD oscillators have also been studied [111], [116], [117].

While making efforts to increase the oscillation frequency, many researchers are also working to increase the much-needed output radiation power. Performance enhancement is achieved by using biased feed slots [118], [119], rectangular cavities as resonators [120], [121], and array configurations [122–124]. Employing RTD oscillators, research has begun on a variety of applications, including imaging, spectroscopy, wireless communication, and radar [125–132].

1.3.1.2 RTD structure and operating principle

Recently, advancement in epitaxial growth technology has helped to make extremely small semiconductor structures. The wave-like nature of electrons is usually prominent in such structures

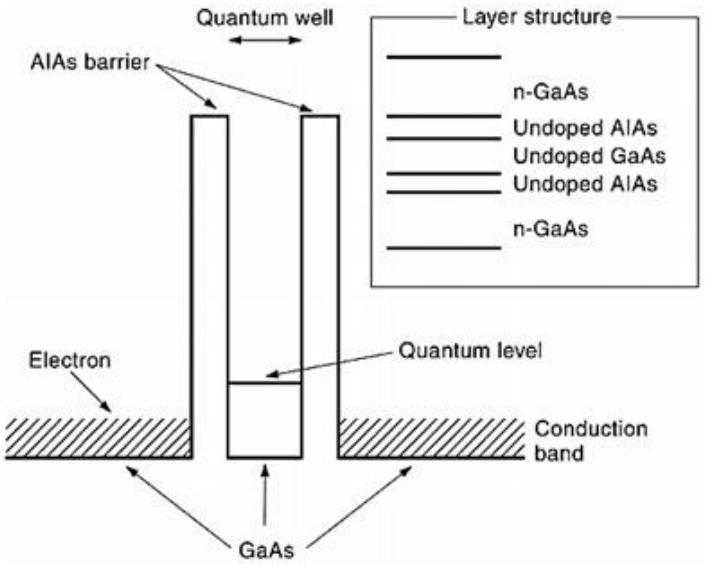

Figure 1.3 Example of RTD structure along with conduction band diagram (Adopted from [253] *)*

due to quantum and tunneling effects. Electrons can tunnel through these thin structures and generate standing waves. RTD also belongs to these kinds of tunneling devices which exhibit quantum effects. RTD is a heterolayer element in which the thickness of layers is between 1nm to 10 nm.

The heterostructure of RTD and the conduction band diagram is shown in Fig. 1.3. The heterostructure layers comprise narrow bandgap and wide bandgap semiconductors. The wide bandgap layers are typically made of $Al_xGa_{x-1}As$ or $In_{0.52}Al_{0.48}As$ semiconductors and narrow bandgap layers are $GaAs$ or $In_{0.53}Al_{0.47}As$ semiconductors. The narrow band gap layer is sandwiched between two wide band gap layers resulting in the formation of a quantum well. Electrons confined in a quantum well exhibit distinct energy levels known as resonance levels. When electrons tunnel through the quantum well their energy is quantized owing to wave-like nature. The resonant tunneling phenomenon occurs when electrons from the emitter tunnel through resonant energy levels to reach the collector. That's why RTD possesses unique current-voltage

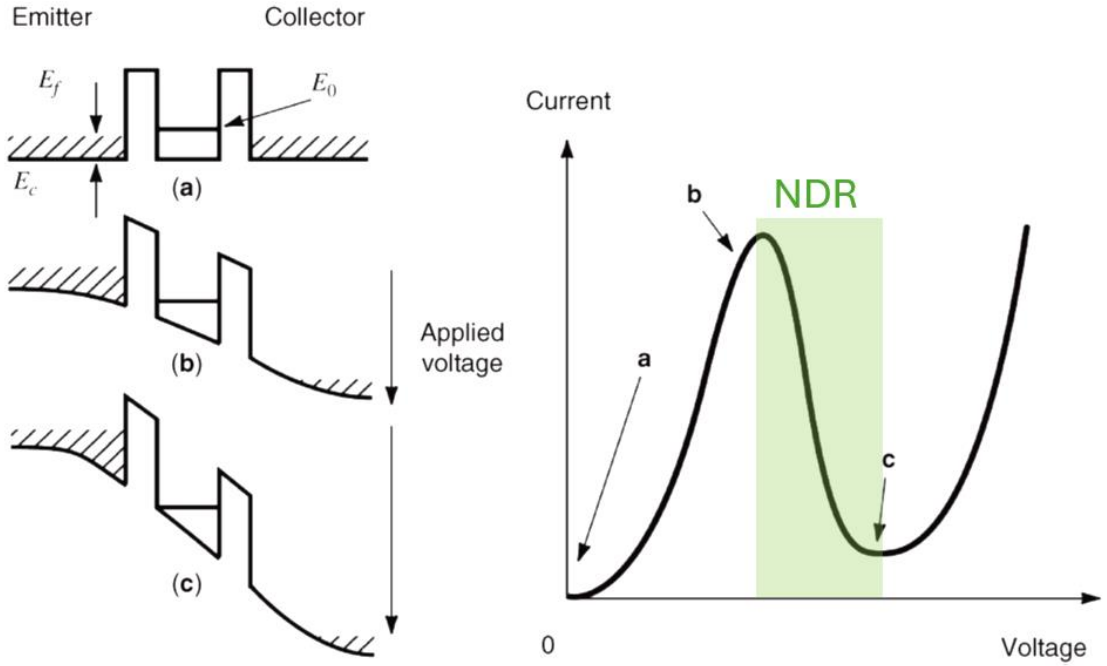

Figure 1.4 Conduction band diagram and IV characteristics of RTD at different applied voltages. (Adopted from [253] *)*

characteristics that show negative differential resistance (NDR) as shown in Fig. 1.4. At zero bias voltage, the emitter's Fermi level is lower than the quantum well's resonance level. As a result, there is no tunneling current as electrons cannot move from the emitter to the collector as shown in Fig. 1.4 (a). Fig. 1.4 (b) depicts the state when the applied voltage increases. In this case, the electrons in the emitter gain kinetic energy and move faster, which results in an increase in the tunneling current. When both the tunneling probability and the incident electron density from the emitter reach their peaks, the tunneling current reaches its maximum known as peak current $I_{p,}$ and voltages at that level are called peak voltages V_p. When applied voltages surpass the V_p, the conduction band of the emitter rises above the resonant energy level of the quantum well. Owing to a mismatch of energy bands, the tunneling current starts decreasing. This range is called negative differential resistance in RTD IV characteristics as shown in Fig. 1.4 (c).

A simple equivalent circuit diagram of RTD is shown in Fig. 1.5. It contains a series resistance and voltage-dependent capacitor parallel with the voltage-dependent current source. Its current and capacitance vary with applied voltages due to which the equivalent circuit has voltage-dependent elements.

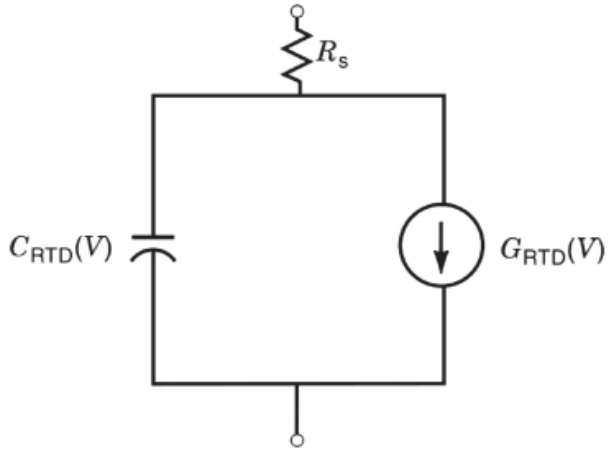

Figure 1.5 Equivalent Circuit diagram of RTD. where R_s is series resistance, C_{RTD} (V) is voltage dependent capacitor and G (V) is voltage-dependent current source.

The basic RTD oscillators consist of a resonator circuit and the RTD as shown in Fig. 1.6. The resonator circuit incorporates Inductor L, Capacitor C, and Resistor R. The NDR of the RTD is the basis of RTD oscillators which provides the gain. This gain compensates for the resonator losses, resulting in sustaining the resonator oscillations.

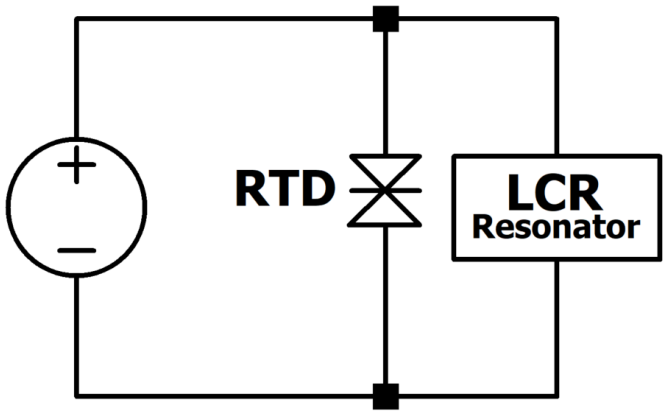

Figure 1.6 Basic RTD oscillator circuit

1.4 Research Motivation, Purpose, and Composition

Resonant tunneling diode (RTD) is a highly promising nonlinear nano-semiconductor device for the THz frequency range. Its current-voltage (IV) characteristics exhibit NDR at room temperature which serves as the foundation for oscillators, and 1.98 THz oscillation has already been reported employing RTD. Most of the research on RTD oscillators is primarily focused on radio communication applications, but since the THz band has a distinctive absorption spectrum to molecules, illicit drugs, cancer cells, gases, and drugs [51], sensor applications in various fields are also promising. Sensors that use RTD oscillators to detect frequency changes due to external parameters have already been proposed and demonstrated [133], [134]. These sensors employ the FDSM technique, which allows for measuring frequency changes with ultrahigh dynamic range and wide bandwidth. However, to take advantage of the FDSM, several challenges need to be addressed, as described below.

It is important to note that RTD is a two-terminal device, which has an inherent drawback. It makes the behavior of the RTD oscillators highly sensitive to minor parasitic effects resulting in frequency fluctuation and spurious oscillations [135–137]. Also, nonlinear IV characteristics provide the foundation for generating chaos. Chaotic signals have a noise-like appearance, but they are deterministic. In fact, Chaos itself has a broad range of applications in secure communication, signal processing, image encryption, and chaos-based mobile robots. On the other hand, it is important to recognize that chaos is an undesired phenomenon in many applications. In particular, the performance of sensors based on RTD oscillators suffers from chaos. Therefore, the nonlinearities of RTD oscillators can pose challenges in implementing them for sensor applications.

The purpose of this research is to investigate the nonlinear phenomena in RTD oscillators and their impact on frequency delta sigma modulation (FDSM) sensors. First, the nonlinear phenomena in RTD oscillators is investigated extensively by applying an external sinusoidal signal while operating the RTD in its NDR region. RTDs have a distinct current-voltage characteristic, including an NDR area in which the current reduces as the voltage increases. When a sinusoidal signal is introduced to an RTD oscillator operating in the NDR region, the device's response is highly nonlinear, resulting in complex chaotic behavior. Subsequently, the nonlinear effects of transmission line (TL) stub on RTD oscillators are also studied. The TL stub can be considered as a delayed feedback unit, introducing a strong nonlinearity in the circuit, leading to chaos. Thus, these circuits work as simple chaos generators with potential applications in the THz frequency range. On the other hand, understanding the effects of such a TL stub and the effects of introducing an external signal is also important for designing RTD oscillator circuits for THz sensors. While considering these effects, scanning near field terahertz microscope (SNFTM) is also proposed based on RTD oscillators as a promising application employing the FDSM technique. The FDSM

relies on ultra-high frequency sampling, so direct sampling is not possible for SNFTM. To solve this problem, two methods using an RTD as a sampler/mixer are proposed and demonstrated through simulation. The basic operation of the sampler is also demonstrated at a lower frequency for ease of measurement. Finally, to realize the potential of RTD oscillator-based FDSM sensors, the impressive results of the fabricated SNFTM prototype device at microwave frequency are presented. It has been demonstrated that a high-resolution image beyond the diffraction limit can be obtained with the fabricated prototype device of SNFTM. Thus, the unprecedented type sensors are anticipated in the THz range using RTD oscillators for FDSM sensors.

The outline of this thesis is shown in Fig. 1.7. In Chapter 2, nonlinear phenomena are investigated in RTD oscillators. In chapter 3, a brief overview of FDSM sensors using high-frequency oscillators is presented followed by the FDSM sensors using RTD oscillators presented in chapter 4. In chapter 5, the findings are concluded of my research work mentioned in this thesis.

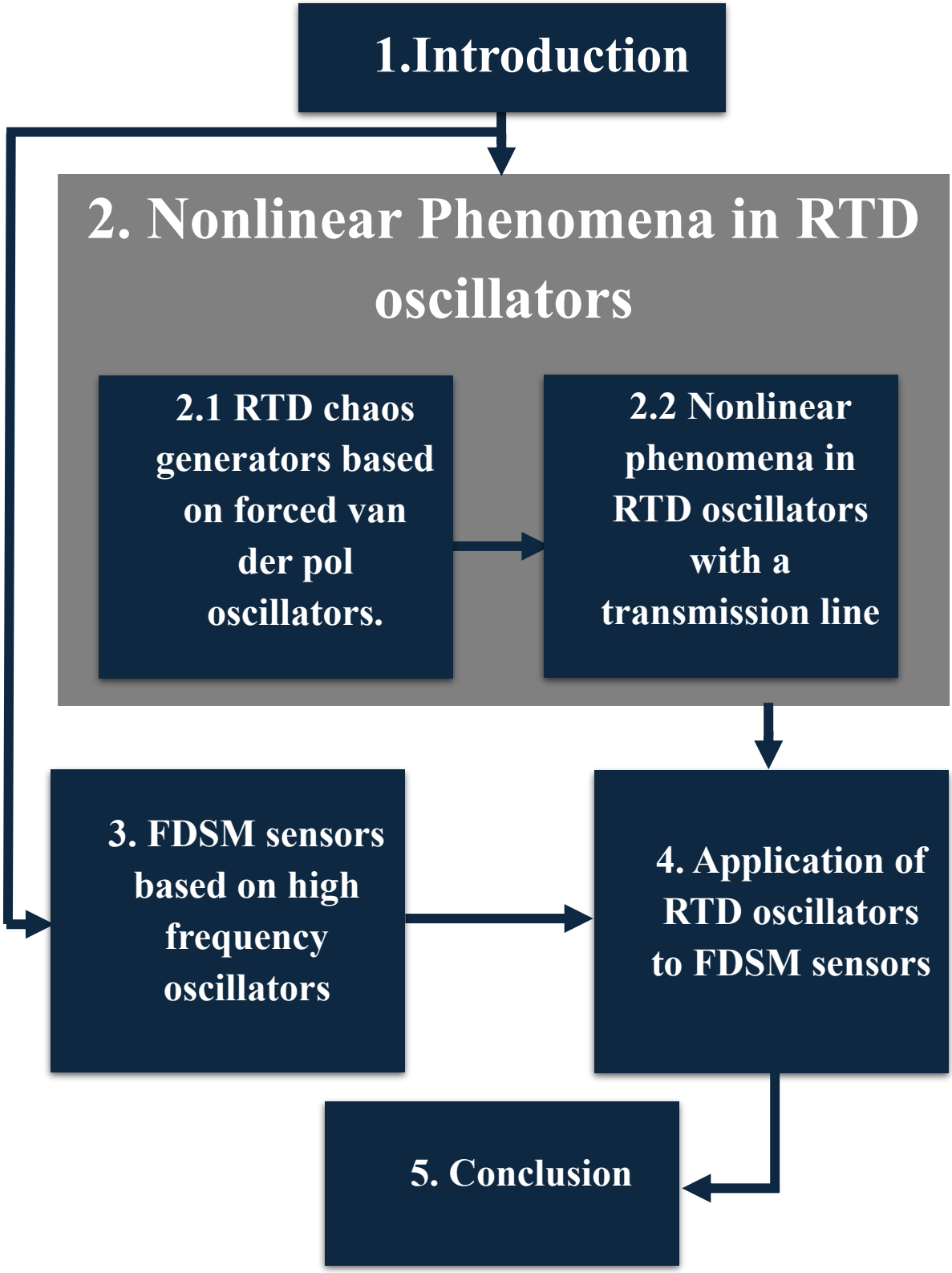

Figure 1.7 Outline of the thesis

Chapter 2 Nonlinear phenomena in RTD oscillators

2.1 Introduction

In this chapter nonlinear phenomena in RTD oscillators have been demonstrated in detail. Here, nonlinear phenomena are referred to as chaos. A brief introduction to chaos and its existence in nonlinear circuits is discussed. Chaos can be a challenge and an opportunity at the same time in oscillator circuits. As an opportunity, it has broad applications. Conversely, it can be treated as an obstacle in the case of conventional applications of oscillators. Two types of RTD oscillator circuits are investigated in this study.

First, the RTD chaos generators based on forced Van der Pol oscillators have been investigated. This circuit is fed by an external sinusoidal signal along with DC bias voltage. It shows both periodic and complex, including chaotic, behavior due to the interplay between the externally applied periodic forcing signal and the intrinsic nonlinear dynamics of the RTD, which are primarily attributed to its negative differential resistance. The circuit design has been improved, which allows an in-depth characterization of the circuit's dynamics.

Second, the nonlinear phenomena in RTD oscillators have been examined when the transmission line (TL) stub is added. The TL stub can be considered as a delayed feedback unit, introducing a strong nonlinearity in the circuit, leading to chaos. Since RTD oscillators operate at high frequencies, the impact of parasitic effects arises substantially, which can significantly reduce the oscillator's performance. So, understanding the effects of such a TL stub and the effect of introducing an external signal is also important for designing RTD oscillator circuits for THz sensors.

2.2 Chaos and its existence in nonlinear circuits

Chaos is a non-linear phenomenon that is usually observed in various kinds of non-linear systems [138]. It is completely deterministic in nature [18]. Also, mathematical models explicitly state the behavior of chaotic systems [139]. Sensitive to initial conditions is one of the significant properties of chaos [140]. Very small changes in initial conditions grow rapidly and lead to complete changes in its future behavior. Figure 2.1 depicts two chaotic signals with slightly different initial conditions that remained the same initially but changed their pattern rapidly from t_1 as the effect of initial conditions dominated. Chaos has its existence in nature, i.e. weather is a chaotic phenomenon [141]. Chaos theory has a profound impact on fields such as physics, biology, and economics, providing insights into understanding complex and nonlinear behavior [142].

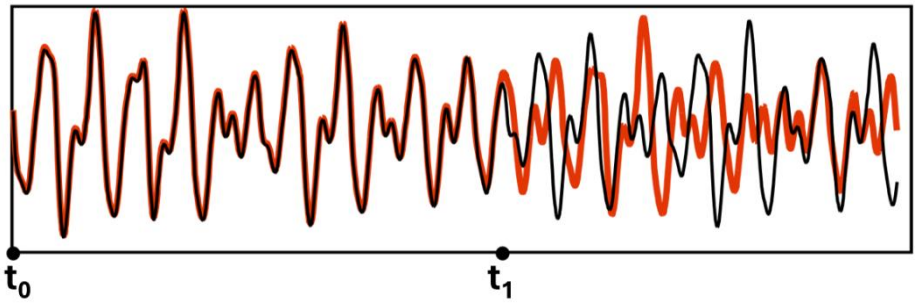

Figure 2.1 Two chaotic signals with slightly difference in initial conditions. (Adopted from [169]*)*

Chaos in nonlinear systems often arises from the nonlinear interactions of system elements, resulting in complex dynamics that cannot be easily predicted. Depending on their parameters and initial conditions, nonlinear systems can exhibit various behaviors, from periodic to chaotic. The existence of chaos in nonlinear systems has been thoroughly studied and verified by mathematical models, computer simulations, and experimental observations [139], [142], [143].

In recent years, potential applications of practically implemented non-linear electronic circuits [144] possessing chaotic dynamics have been increased in many fields such as secure

communications [20–22], signal processing [19], [23], [24], [145], image encryption [17], [146], chaos engineering for chaos-based technical applications [147–150], and even chaos based mobile robots [151–153]. Recently, circuits generating microwave/millimeter-wave/terahertz wave chaos have also gained considerable attention with possible applications of high-speed secure communication [154], [155], terahertz spectroscopy with high resolution [156–159], and chaos-based cryptography to encrypt information [160], [161]. Chaos, which was earlier intuitively declared as a bizarre and random phenomenon because of its noise-like appearance, is rigorously deterministic in nature [17], [18], [162], [163]. Since chaos is extremely sensitive to initial conditions, and errors in initial conditions are inevitable in real [164], controlling chaos is challenging, especially, at high frequency. Chaos must be controlled for possibilities of unprecedented applications in numerous fields [143], [165–168].

2.3 RTD chaos generators based on forced van der pol oscillators

In this section, a detailed characterization of resonant tunneling chaos generator circuits is demonstrated in the microwave frequency range. The circuit is analogous to the Duffing oscillator, where the third-order nonlinear potential term is emulated by the nonlinear current-voltage curve of the resonant tunneling diode. The circuit includes a periodic reset mechanism to output identical chaos signals, which is essential for observing chaos signals on a sampling oscilloscope. Though this was shown to be effective previously [169], [170], the length of the waveforms to observe is limited to rather a short period, and it was unclear if this technique can be used for detailed characterization of such high-frequency chaos. In this chapter, the circuit design is improved to observe longer waveforms, and demonstrated that detailed characterization is possible using this periodic resetting technique with a sampling oscilloscope. The hybrid integration scheme is also used in this chapter, which allows the easiest and shortest way to mimic a circuit as per circuit

design, and precise estimation of circuit parameters aiming to eliminate circuit-related abnormalities. A deep insight is provided into the dynamics associated with our circuit, starting from the single-period, double-period, chaos, and triple-period regimes, by extracting power spectra, return maps, phase portraits, and bifurcation diagrams from acquired time series using a sampling oscilloscope. Our method to study microwave chaotic signals can be applied to much higher frequency ranges, such as the THz frequency range.

2.3.1 Chaos in the negative resistance oscillator circuit

Chaotic phenomena had been confirmed in forced negative resistance oscillator [171]. That circuit had a negative resistance element along with a capacitor, inductor, and resistor as shown in Fig. 2.2. It is a non-linear self-oscillatory circuit in which non-linearities arise due to a negative resistance element. When periodic forcing is injected to this circuit it generates synchronized periodic signals or unsynchronized output. Among non-periodic output signals, most of them are chaotic in nature. The behavior of the circuit was checked by altering the parameters of external sinusoidal forcing. Chaotic oscillations had been confirmed which occurred in non-periodic output

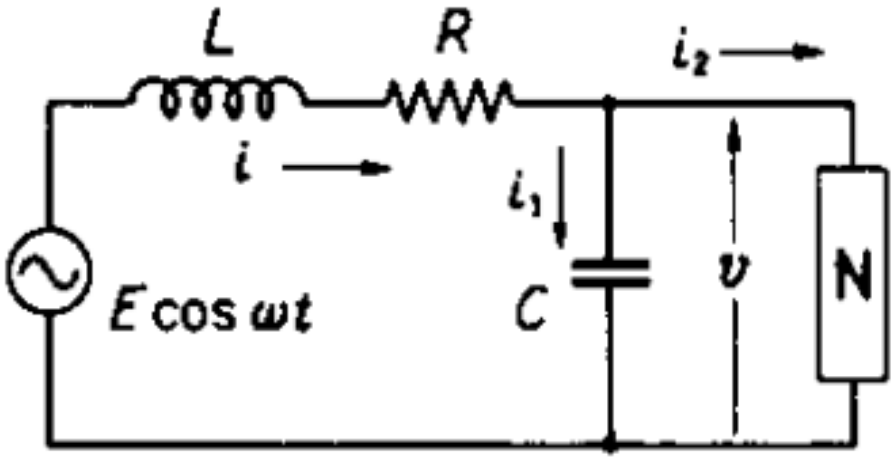

Figure 2.2 Forced negative resistance oscillator (Adopted from [171] *)*

regions. The operating speed limit of such circuits is regulated by a negative difference element. So, the maximum frequency of chaotic signals is solely dependent on the operating speed of the negative resistance element.

2.3.2 Resonant tunneling chaos generator

RTDs are nonlinear nanodevices that own very high operational speed with the prime feature of depicting negative differential resistance (NDR) in their current-voltage characteristics [12]. For high-frequency chaos applications, a very simple chaos generator circuit employing an RTD was proposed, and also demonstrated its frequency divider operation based on the bifurcation phenomenon [172], [173]. 1/2 frequency divider operation at high frequencies up to 88 GHz has already been reported for this circuit [174].

The basic circuit configuration of the resonant tunneling chaos generator is shown in Fig. 2.3. This simple chaos generator consists of an inductor *L*, a capacitor *C*, and an RTD which acts as a negative differential resistance element. A brief illustration of circuit operation is discussed below [175].

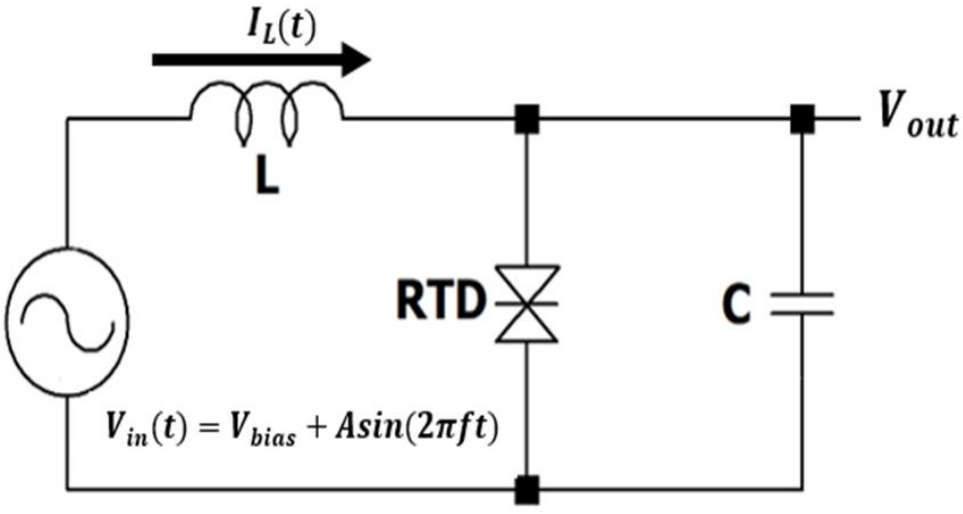

Figure 2.3 Basic circuit of resonant tunneling chaos generator

This circuit is identical to the Duffing oscillators in terms of the underlying mechanism. Third-order polynomial potential in the Duffing oscillator is replaced by the folded I-V curve of the RTD. The circuit is fed by DC voltage to bias the RTD in its NDR region, which causes the circuit to oscillate. So, when the circuit's oscillations are perturbed by external sinusoidal forcing then it generates either synchronized or unsynchronized output, depending on operating conditions. As a result, the circuit depicts the period-adding bifurcation phenomenon in the synchronized region, which works as a frequency divider, i.e., f_{in}, $f_{in}/2$, $f_{in}/3$ [172]. In the unsynchronized region, high-frequency chaotic oscillations appear. This circuit aims to produce microwave chaotic oscillations by taking advantage of the high-speed operation of an RTD. The following equations represent the circuit mathematically if parasitic elements and the voltage-dependent RTD capacitance are not taken into account.

$$\frac{dI_L(t)}{dt} = \frac{V_{in}(t) - V_{out}(t)}{L} \tag{2.1}$$

$$\frac{dV_{out}(t)}{dt} = \frac{I_L(t) - I_{RTD}(t)}{C} \tag{2.2}$$

$$V_{in}(t) = V_{bias} + Asin(2\pi ft) \tag{2.3}$$

Where I_{RTD} (V) represents the I-V curve of the RTD.

First, the simulation was performed to understand the behavior of the circuit. This uses the I-V model proposed by Schulman [176] carrying identical characteristics to the fabricated InP-based RTD used for experiments. The RTD model consists of a voltage-controlled current source and capacitance connected in parallel as shown in Chapter 1 section 1.3.1.2. The RTD capacitance value is based on the assumption of a parallel plate capacitance from the thickness of the collector

depletion layer. The RTD I-V characteristic model and collector depletion layer capacitance are defined by Equation 2.4 to Equation 2.7, respectively.

$$\boldsymbol{I_{RTD}(V) = I_{PDR}(V) + I_{NDR}(V)} \quad \textbf{(2.4)}$$

$$\boldsymbol{I_{PDR}(V) = \mathrm{sgn}(V) A j_p \{a_0 \log\left[\frac{1+\exp(-a_1+a_2|V|)}{1+\exp(-a_1-a_2|V|)} \times \left(\frac{\pi}{2} + tan^{-1}(a_3 - a_4|V|)\right)\right]\}} \quad \textbf{(2.5)}$$

$$\boldsymbol{I_{NDR}(V) = sgn(V) A j_p b_1 (\exp\left(\frac{|V|}{b_2}\right) - 1)} \quad \textbf{(2.6)}$$

$$\boldsymbol{C_{RTD} = A C_0} \quad \textbf{(2.7)}$$

where j_p is the current density, a_0, a_1, a_2, a_3, a_4, $b_{1, \text{and}}$ b_2 are fitting parameters, and A is the RTD area. The parameters are listed in Table 2.1, and the I-V characteristics of the RTD model are shown in Fig. 2.4.

Table 2.1 Parameters of the RTD model used in the simulation

Parameters	**Values**	**Parameters**	**Values**
a_0	9.4546×10^{-10}	b_1	5.792×10^{-12}
a_1	0.59	b_2	0.17
a_2	13	$C_0(\mathrm{fF/\mu m^2})$	2
a_3	14	$j_p(\mathrm{A/cm^2})$	1×10^5
a_4	35	$A(\mu\mathrm{m}^2)$	15

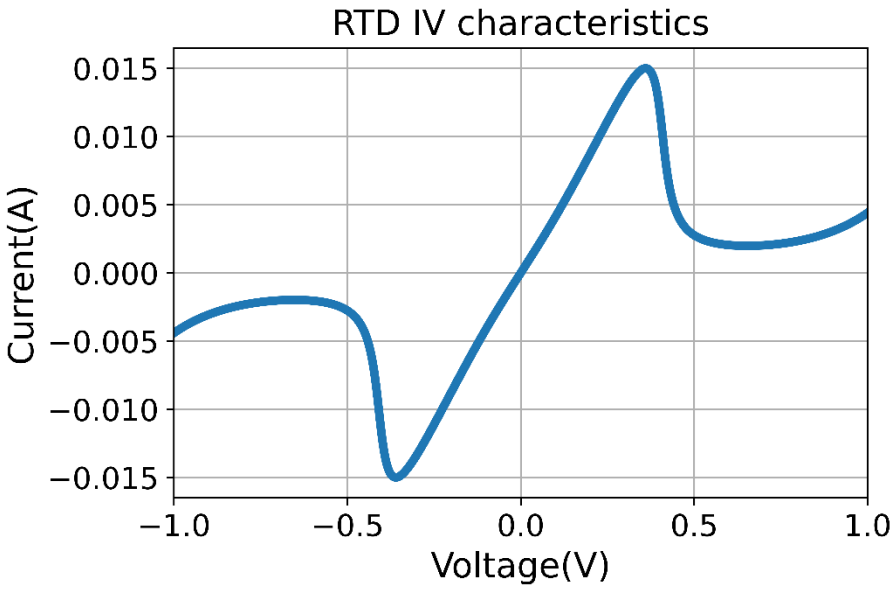

Figure 2.4 IV characteristics of the RTD model employed in simulation

To illustrate the basic behavior of the above circuit, an example of a bifurcation diagram obtained from simple simulation is shown in Fig. 2.5. The resonant frequency of the LC resonator with chosen parameters, L = 1.3 nH and C = 10 pF, was 1.4 GHz. Figure 3 illustrates the period adding

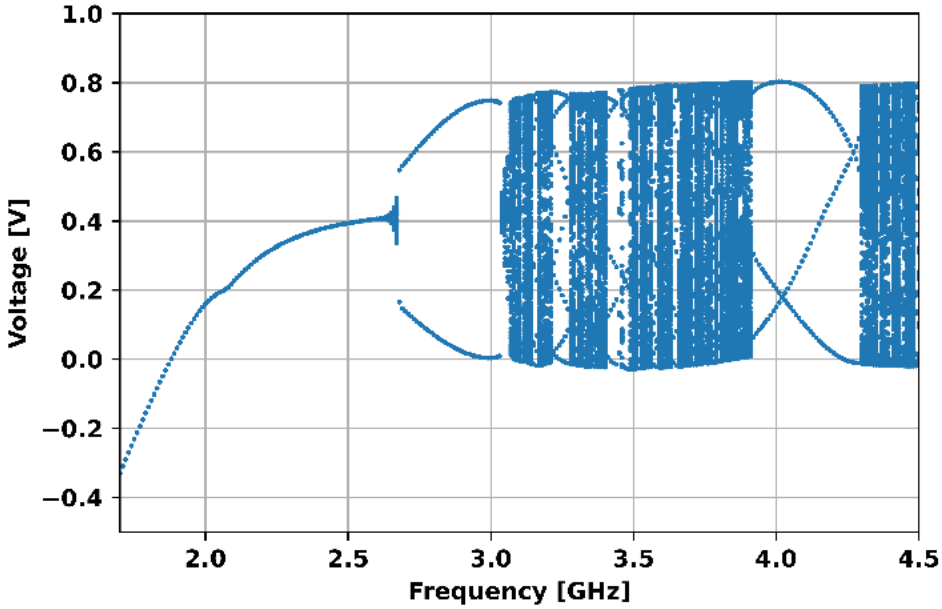

Figure 2.5 Example of a bifurcation diagram of a simple RTD chaos generator

bifurcation diagram by plotting input frequency versus output voltage from simulation results. It represents a cascade of synchronized and unsynchronized regimes. The Densely filled spaces in the figure indicate nonperiodic zones which include chaos. Conversely, solid distinct lines exhibit periodic regions. A sequence of single period, double period, nonperiodic (chaos and quasi-periodic), triple period, and non-periodic states appears by sweeping input frequency as a bifurcation parameter. This behavior is similar to that of the Duffing oscillators.

2.3.3 Constraints in observing high frequency signals

For high-frequency signals such as micro/millimeter/THz wave frequency range, one generally uses a sampling oscilloscope to observe their waveforms, however, there are constraints in using it for non-periodic signals. For example, microwave chaotic signal becomes blurred on the sampling oscilloscope as shown in Fig. 2.6. This is due to the superposition of various signals. Chaotic signals are non-periodic, which impedes observation with a sampling oscilloscope. However, one can observe such signals, if it is controlled to output identical signals repeatedly

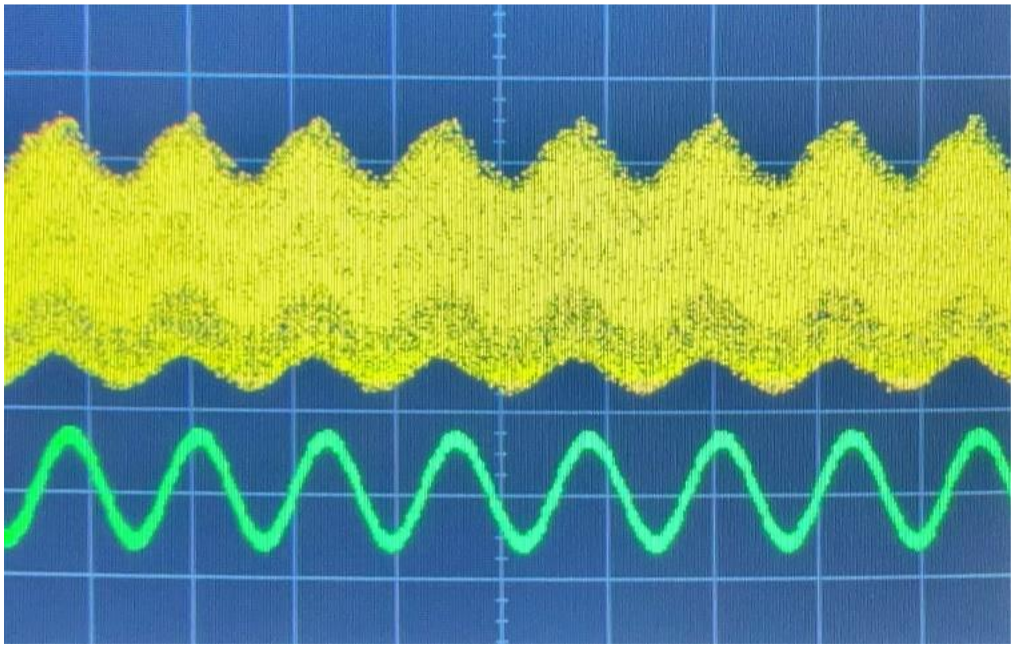

Figure 2.6 An example of the blurred output waveform of the chaos signal on the sampling oscilloscope. Upper figure: the output signal. Lower figure: the input signal. Horizontal axis 200 ps/div, Vertical axis 100 mV/div.

[169]. Of course, chaos signals are sensitive to initial condition errors, and practically such errors are inevitable, so it is impossible to output identical sequences. However, if we limit the period to reset sufficiently shorter than the time for substantial growing of the initial condition errors, such sequence can be observed on a sampling oscilloscope.

2.3.4 Circuit design for high-frequency chaos characterization

Here a simple and improved circuit configuration is proposed that permits chaotic signals to be observed on a sampling oscilloscope for detailed characterization of chaos as shown in Fig. 2.7. The circuit for reset is different from the previous reports. In the previous papers, switching to reset the circuit was achieved by incorporating a high electron mobility transistor (HEMT) in parallel to the RTD. To mask the NDR of the RTD for reset, the HEMT must have large current drivability. For this reason, a very wide-gate HEMT was used. This consumes much area, and has large parasitic elements. It also makes designing the circuit pattern/layout difficult for the high-frequency circuit. In the current circuit configuration, the reset pulse signal is applied directly to

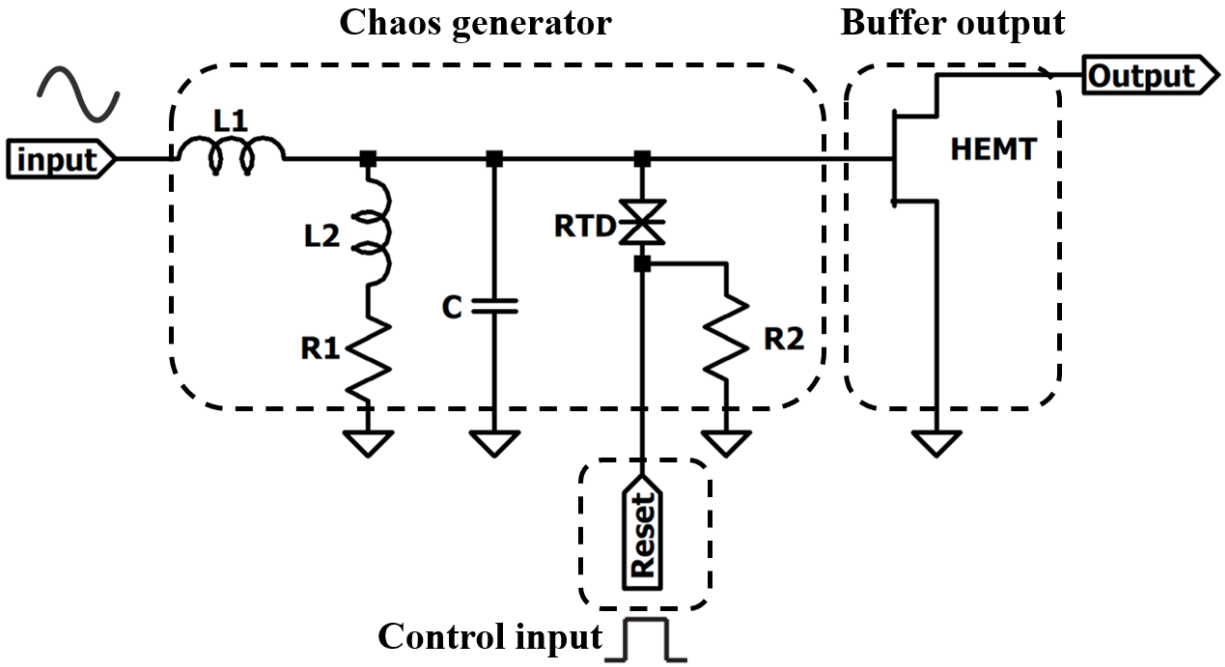

Figure 2.7 Improved design of the resonant tunneling chaos generator and control circuit

RTD, thus circuit complexity is reduced as well. The advantage of the high-speed switching capability of RTD is also taken for resetting the circuit. Moreover, low-frequency noises due to the HEMT switch are avoided in this circuit. This scheme assists in prolonging the observable period due to the reduction of parasitic effects, which made optimization of circuit parameters difficult. This is also applicable for the THz frequency region, even when the conventional device switch is difficult to use. The shunt resistor is connected parallel to the chaos generator for the prevention of spurious oscillations induced by RTD. Moreover, two inductors are used here, one for the resonator and one for the input. This makes better isolation of the signal source impedance and easier design of the Q-factor of the resonator. The HEMT in common source configuration behaves as a buffer device to isolate the circuit's output from interference caused by measurement devices as well as amplify the output signals.

2.3.5 Prototype circuit fabrication

The circuit was fabricated with a hybrid integration scheme on a printed circuit board (PCB) using a small RTD chip fabricated in the lab and commercially available chip elements. This method allows an easy, short, and compact fabrication process to emulate the circuit according to the circuit design with easy optimization of the circuit's parameters. The RTD was fabricated on an InP substrate with a double-barrier quantum well structure grown by molecular beam epitaxy. It contained a strained subwell of an InAs in the core of an $In_{0.53}Ga_{0.47}As$ well. Fabrication was realized by conventional photolithography, wet etching, and lift-off process.

The current-voltage characteristics are illustrated in Fig. 2.8. The NDR region of the RTD is utilized for introducing non-linearities in the circuit. Figure 2.9 depicts the circuit realized on the

PCB substrate on the right and the SEM image of the RTD on the left. The circuit was fabricated on a double-sided glass epoxy FR-4 PCB substrate.

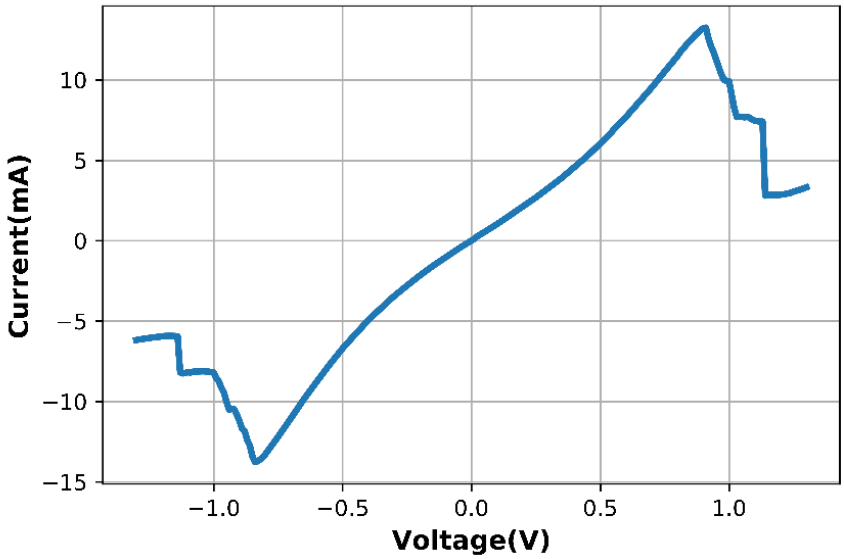

Figure 2.8 Current-Voltage characteristics of the fabricated RTD. The RTD mesa area was 10.4μm²

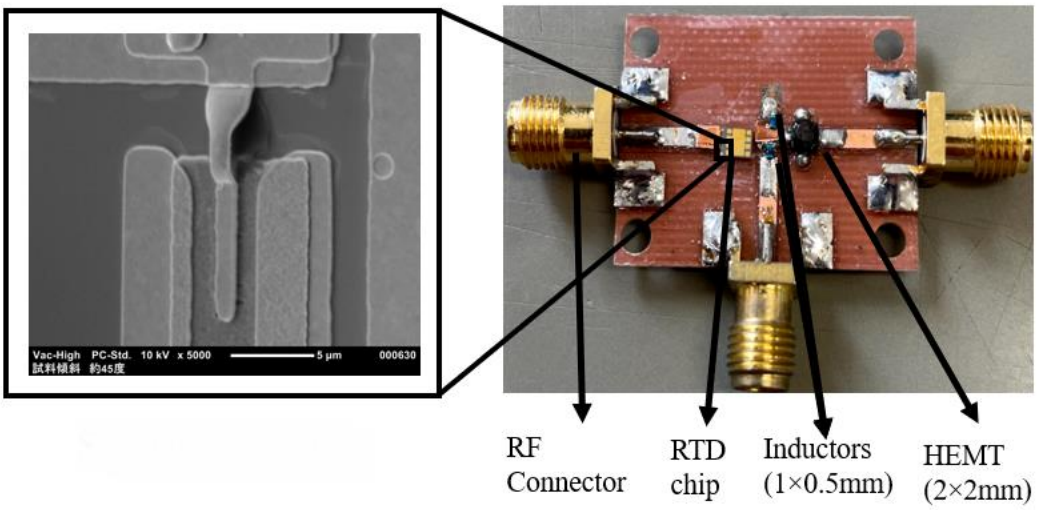

Figure 2.9 Fabricated prototype circuit (right), and the SEM image of the RTD (left)

The dimensions of the PCB substrate were opted for 28 mm × 22 mm with a thickness of 0.8 mm. The RTD chip was interconnected with the help of bonding wires. To reduce the impact of bonding wires, shorter-length multiple wires were used. 1.0 mm × 0.5 mm-type wire wound RF inductors, chip multilayer ceramic capacitor, and chip resistor were used. A low-noise GaAs HEMT (Renesas

Electronics, NE3514S02) was opted for the buffer amplifier. The nominal values of the elements are illustrated in Table 2.2.

Table 2.2 Device parameters used for the fabricated circuit.

Elements	**Values**
L_1	4 nH
L_2	1.3 nH
C	10 pF
R_1	5 Ω
R_2	24 Ω

2.3.6 Experimental setup

Measurement setup for detailed characterization of resonant tunneling chaos generators is depicted in Fig. 2.10. In this circuit, the pulse signal (reset signal) is directly transmitted from the pulse pattern generator (ANRITSU MP1761C) at the reset node of the circuit with DC voltage via Bias T. At pulse ON state the DC voltage level rises up to the NDR voltage range of the RTD, thus circuit starts oscillating with its natural frequency. The oscillations are perturbed by an external sinusoidal signal which is supplied to the input port by a synthesized sweeper. (Keysight technology 83650L). In the case of the pulse OFF state, the voltage of the circuit drops down from the NDR voltage range, and circuit nonlinearity becomes weaker. This resets the circuit to non-oscillation state. When the pulse returns to ON state, an identical signal appears at the output port. Thus, a sequence of chaos can be observed on the sampling oscilloscope (HEWLETT PACKARD 54750A). In order to lock the reset pulse with sinusoidal input, which is indispensable, the pulse pattern generator is synchronized with the synthesized sweeper via a 10 MHz clock signal. To

observe the circuit output corresponding to the input signal, a power splitter is inserted in the input sinusoidal signal line, and it is connected to channel 2 (Ch2) of the sampling oscilloscope. For data acquisition, a computer was connected to the sampling oscilloscope.

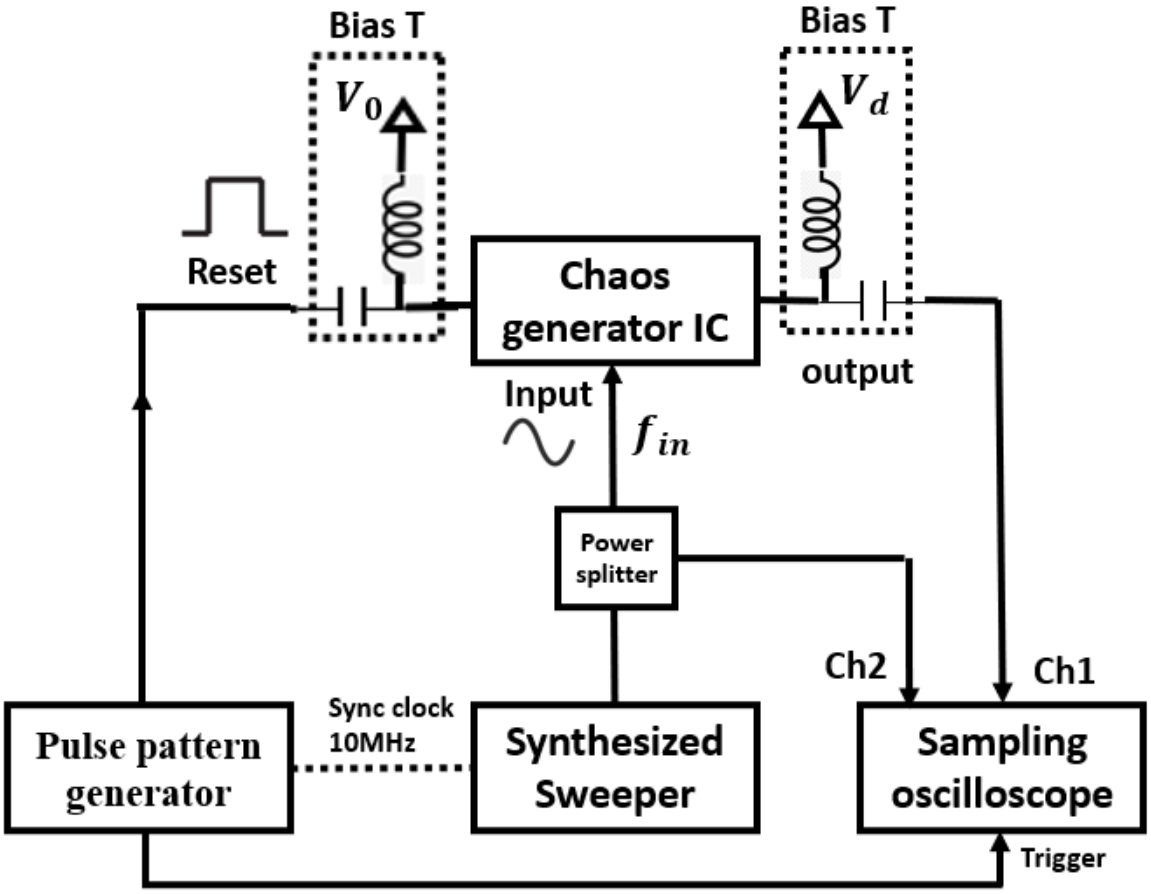

Figure 2.10 Measurement setup for detailed characterization of circuit's output

2.3.7 Results and discussion

Initially, the circuit is tested as an autonomous system without an external forcing signal to determine the NDR region of the RTD and the circuit's natural frequency, which were 810 mV to 910 mV and 2.5 GHz, respectively. Under this condition, the circuit worked as a harmonic oscillator, showing stable oscillations.

2.3.7.1 Bifurcation diagram plotting method

A bifurcation diagram is a graphical representation of how the behavior of a dynamical system changes as system parameters change. It often depicts the emergence of complex behaviors such as periodicity, chaos, or the creation and destruction of stable solutions. Solid lines show the stable values (Periodic) and filled condensed areas represent unstable values which are often chaotic.

To get a bifurcation diagram of the resonant tunneling chaos generator circuit, externally provided sinusoidal signal frequency was swept as a bifurcation parameter while keeping the rest of the operating conditions same. The method used to plot the bifurcation diagram involves the sampling of the output signal at the fundamental period of the input signal. If the period of the output signal is the same as the input signal, a single dot appears, if the output signal's period is double than the input signal, two dots appear by sampling the output signal at the input signal's period, and so on. If it is a complex output then multiple dots appear on the bifurcation diagram. For a better

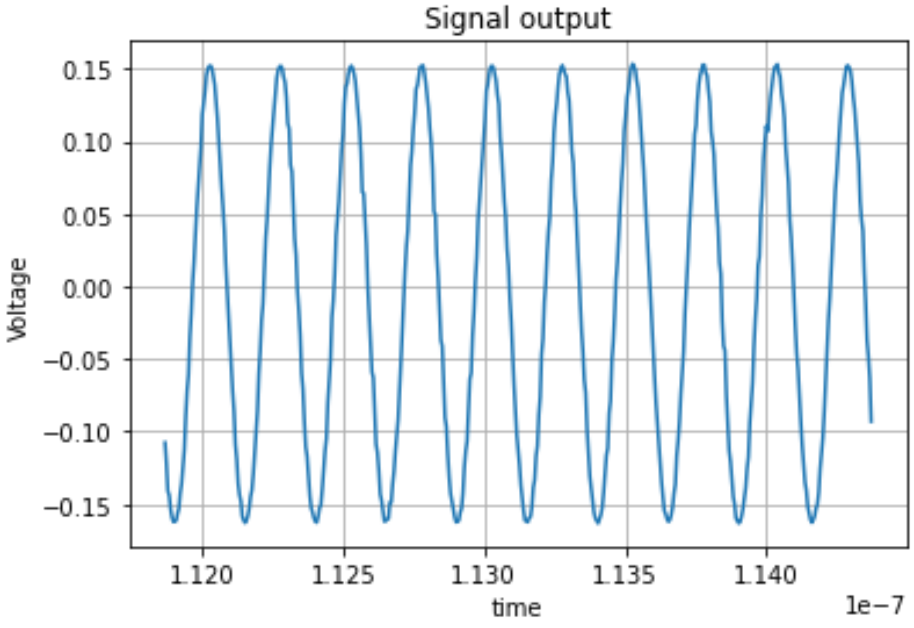

Figure 2.11 ***4 GHz*** *periodic signal*

understanding of constructing a bifurcation diagram, bifurcation points of periodic sinusoidal signal are shown here in this section. Figure 2.11 depicts the sinusoidal signal at 4 GHz. If the time period of the applied sinusoidal signal is exactly the same as the time period of the output signal, only one point appears which indicates the period one output as shown in Fig. 2.12. If the time

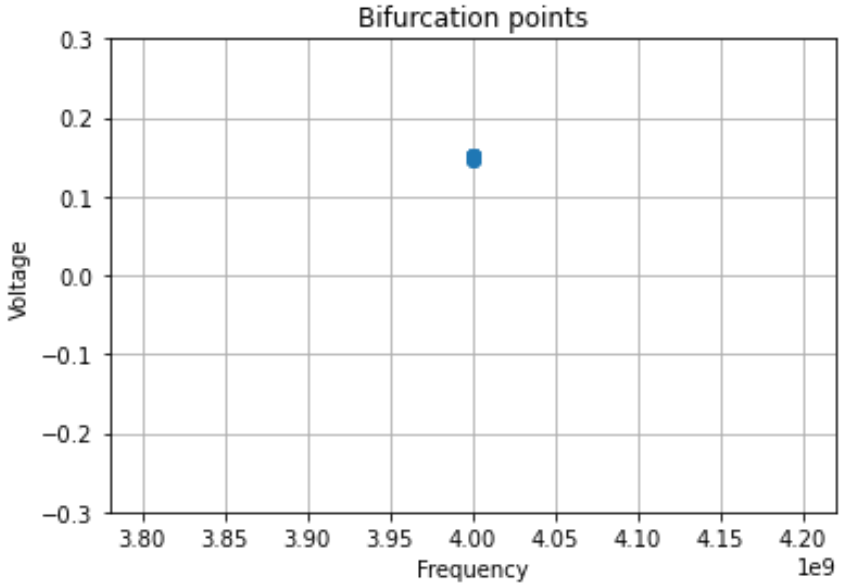

*Figure 2.12 Bifurcation point of 4 GHz signal (sampled at **1/4 GHz** rate)*

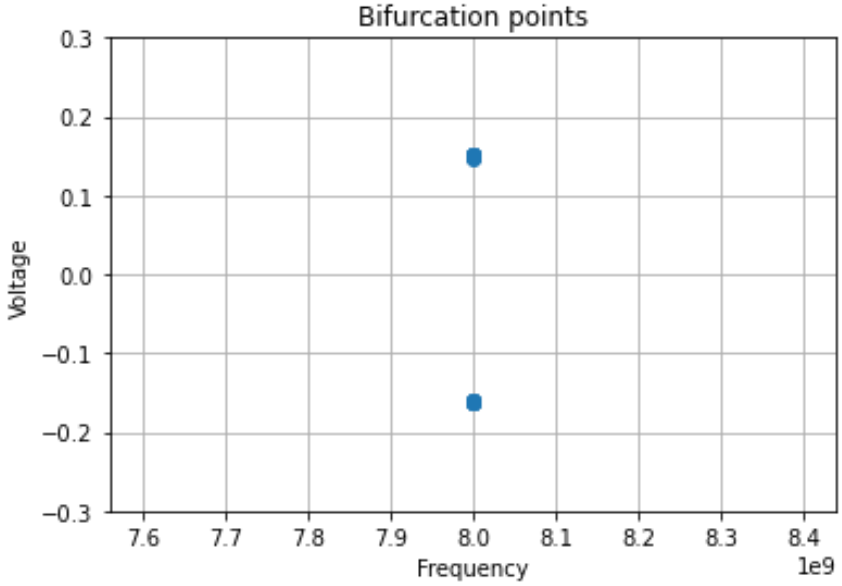

*Figure 2.13 Bifurcation point of 4 GHz signal (sampled at **1/8 GHz** rate)*

period of the output signal becomes double the time period of the input signal, we will get two points indicating period two output as shown in Fig. 2.13.

2.3.7.2 Experimental Bifurcation diagram

To investigate circuit dynamics on the sampling oscilloscope, an 80 MHz reset pulse signal is injected for direct observation. Input frequency as a bifurcation parameter was swept from 2.4 GHz to 9 GHz with steps of 10 MHz at 0 dBm power by fixing bias voltages at 810 mV. The input impedance, |Z|, is estimated to be approximately 160 Ω using circuit simulation. Therefore, the voltage amplitude for the 0-dBm input is estimated to be 0.96 V_{pp}. An experimental bifurcation diagram at high frequency is plotted to present a visual interpretation of circuit behavior where the output switches between periodic and chaotic by varying the input frequency. However, the conventional methods of plotting bifurcation diagrams failed at this frequency range. If one plots the bifurcation diagram by sampling the output signal at the fixed phase of the input signal, it turns out to be a highly oscillating and noisy figure as shown in Fig. 2.14. This is due to the time delay in the cables, and hence, the frequency-dependent phase difference between input and output signals. The difference in the cable length carrying the input and output signals yields this effect. To overcome these inevitable problems, a compensation method is used as shown below. Let the cable length difference of the input and output cables, and the effective velocity of the signal propagation in the cable be Δl and v_{eff}, respectively. Then the propagation time delay difference, ΔT, at the sampling oscilloscope head can be written as

$$\Delta T = \Delta l / v_{\mathrm{eff}},$$

Hence, the oscillation period in the experimental bifurcation diagram, Δf can be approximately shown as,

$$\Delta f = 1/\Delta T$$

Therefore, the time delay difference ΔT can be determined by the oscillation period in the bifurcation diagram. Consequently, the phase difference can be compensated if the output signal is sampled at $\phi = 2\pi f_{in}\Delta T$ in place of $\phi = 0$. Here, the f_{in} is input frequency. In the case of my experiment, 4.44 ns time delay is estimated in the output signal.

After fixing the phase difference error by following the above method, a meaningful bifurcation diagram was achieved as shown in Fig. 2.15, which is identical with the simulated bifurcation diagram in terms of periodic and nonperiodic states switching sequence. Nevertheless, it is relatively noisy due to unavoidable external noise, especially phase noises. There is the evolution of period one, period two, non-periodic, period three, and non-periodic regimes. Single periodic output appears between the 2.4 GHz to 4.7 GHz range representing a phase-locked regime. From 4.7 GHz to 5.3 GHz range, period doubling regime commences. There is an onset of non-periodic regime from 5.3 GHz to 6.5 GHz range right after the period doubling. Period doubling leading to the emergence of chaos has already been reported in the Duffing oscillator [177]. A densely filled area indicates the occurrence of non-periodic regime, that should correspond to chaos as discussed later. After the non-periodic region, the evolution of synchronized state appears which is the period-three region from 6.5 GHz to 7.9 GHz. From 7.9 GHz up to 9 GHz, non-periodic regime re-emerges.

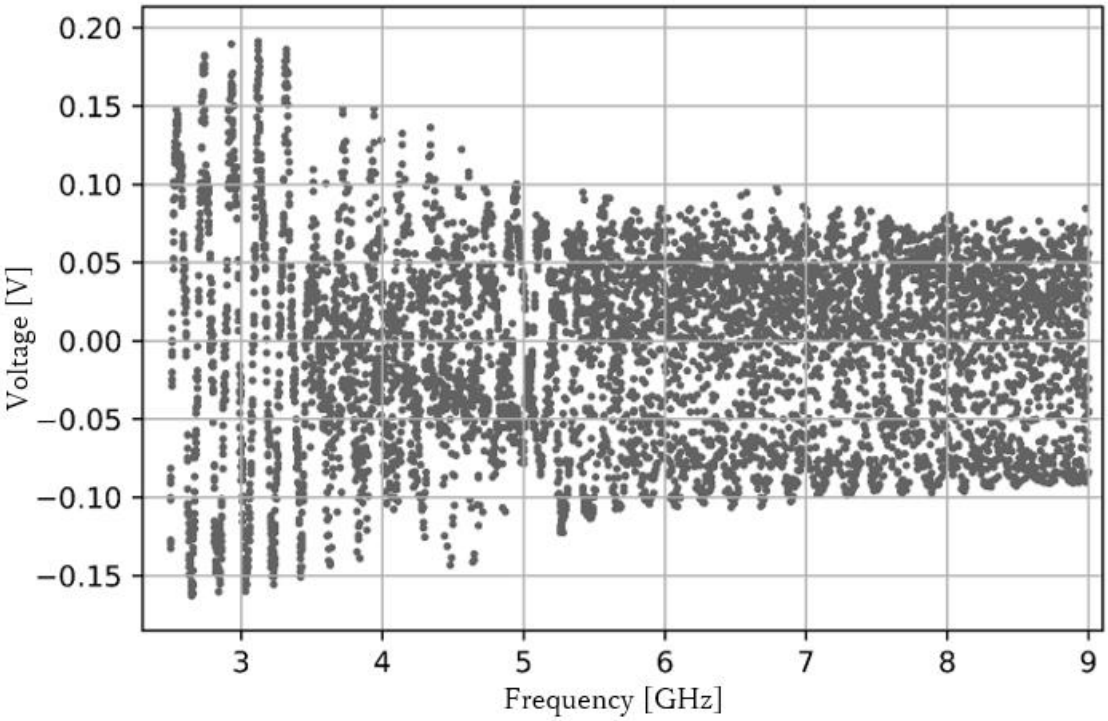

Figure 2.14 *Experimental bifurcation diagram without fixing phase difference error. Input signal frequency is taken on x axis and output voltages on y-axis.*

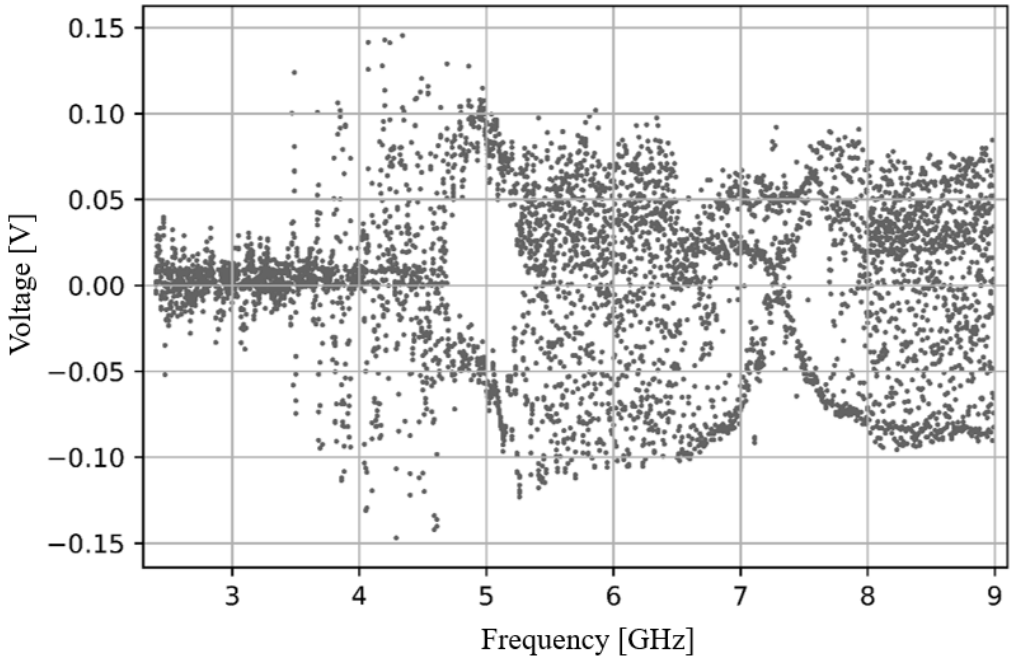

Figure 2.15 An experimental bifurcation diagram by sweeping input frequency from 2.4 GHz to 9 GHz after breaking through the phase difference obstacle

2.3.7.3 Detailed characterization of each regime

The purpose of this research is to demonstrate that the periodic resetting technique can be used for detailed characterization of the microwave/millimeter wave/THz wave chaos circuits. In the previous papers, the observation of such high frequency chaos signals in RTD circuits was demonstrated with a sampling oscilloscope, however, detailed characterization, in particular, calculation of Lyapunov exponents, was impossible because the observable waveform length was insufficient. In this chapter, the improvement of the circuit design allowed us to observe the output waveform up to 58 periods of the input signal, which is approximately 3 times longer than those in the previous reports. This improvement helped us acquire temporal waveforms data at a high frequency for further analysis.

Here, I present detailed characterization results with the experimentally acquired data. I obtained time domain signals at different input frequencies. Their corresponding power spectra, phase portraits, and return maps were obtained from these data. Also, Fourier analysis was done for these data, which is an effective experimental aid in recognizing the various types of attractors [178]. Reconstruction of phase space (Phase portrait) is a handy tool which is used to reveal the shape and structure of attractors that helps to identify the nature of signal. The conventional method of plotting phase portrait requires a system of differential equations to plot the trajectories in the phase space using multiple state variables. Typically, one state variable is plotted against another state variable or its derivative. In experiments, the most challenging point in plotting conventional phase portrait is the difficulty in getting derivative of the voltage waveforms by numerical derivation, because small noise can generate large errors. On the other hand, the time delay method is robust against the noise. So, the time delay method provides a solution by reconstructing a phase space from delayed versions of the one-dimensional time series data, allowing for the analysis of

system's dynamics. I followed the mutual information method [179] to estimate time delay τ. The mutual information method is a technique for estimating the optimal time delay parameter (τ) for embedding a time series in phase space. Once the optimal time delay τ is identified, it can be utilized for further analysis, such as the reconstruction of the phase space or even the determination of the Lyapunov exponent. Reconstruction of phase space (Phase portrait) of periodic signal is a limit cycle. On the other hand, phase portraits displaying strange attractors are attributed to chaotic systems [180]. Here, the phase portraits were reconstructed by plotting V (t) versus V ($t + \tau$) where V (t) is the output voltage. Subsequently, a return map is also a valuable analytical tool to distinguish the circuit's dynamics, which was plotted as x [n] on the x-axis and x [n + 1] on the y axis, where x [n] represents the phase point and x [n+1] is next phase point. These points were extracted by sampling output time series waveforms corresponding to the peaks of input signals.

Figure 2.16 shows the results at 2.5 GHz input. Here, the time-domain output signal is shown with a corresponding power spectrum having a single peak, a closed-loop phase portrait, and a single dot return map, indicating single period output. Similarly, Fig. 2.17 shows the results at 5 GHz. The power spectrum consists of two distinct peaks, a phase portrait with a twisted closed-loop, and two clear dots on the return map, and the output waveform reveals double period bifurcation acting as a 2:1 frequency divider.

After period doubling, the route to chaos was recognized at 5.46 GHz input signal frequency. Figure 2.18 illustrates the chaotic time series representation and its power spectrum. The power spectrum consists of rich spectral structure and broad-band peaks which are not rationally related to primary peak [178]. The phase portrait forms a strange attractor similar to Duffing oscillator (double scroll attractor), which is the signature of chaos [181]. The distributed points in return-map are making parabola-like shape exhibiting deterministic characteristics [182] and indicating

deterministic chaotic oscillations. In order to characterize the waveform quantitatively, the largest Lyapunov exponent (λ_{max}) was calculated employing the Wolf method [183]. The positive value of λ_{max} indicates chaotic time series. I got $\lambda_{max} = 0.0579$ which further authenticates chaotic output at 5.46 GHz. Here, I used 58 periods data for the calculation of Lyapunov exponents. It is a difficult problem how large number of periods are necessary for this calculation. The reference [183] has discussed it and shown that on the order of 10 to 100 is necessary for 1-D systems. Therefore, I think this value is, at least, approximately valid because our system is close to 1-D system.

Finally, Fig. 2.19 shows results at 7.5 GHz. The power spectrum with three peaks, a phase portrait containing doubly-twisted phase space orbit, and three distinct dots in the return map are giving confirmation of triple period output and 3:1 frequency divider operation. Beyond the triple period regime, there was the onset of a more complex non-periodic regime, which was strenuous to observe due to the superposition of various signals. Anyway, these results demonstrated that the periodical resetting scheme successfully characterizes microwave chaos signals, and it should be a good tool for characterizing millimeter/THz wave chaos signals.

For further validation of experimental results, I also performed a simulation of the more realistic circuit by incorporating parasitic elements of the chip devices and compared its results with experimental results. Figure 18 shows the simulated bifurcation diagram by taking frequency and voltage on x-axis and y-axis respectively. It represents a behavior identical to experimental bifurcation diagram in terms of switching sequence of periodic and non-periodic regime as shown in Fig. 2.20. Differences in their frequency ranges can be attributed to other parasitic elements, such as pattern layout, connectors etc., which are difficult to include. In order to characterize the output of each regime and compare them with experimental results, I plotted the phase portraits by time delay method to show the trajectories. Figure 2.21 shows the phase portraits of single period

(closed loop), double period (twisted closed-loop), chaos (double scroll attractor), and triple period (doubly-twisted) that are similar to the phase portraits of corresponding regime of experimental results. This similarity provides a good agreement between simulated and experimental results, and also validates our conclusion.

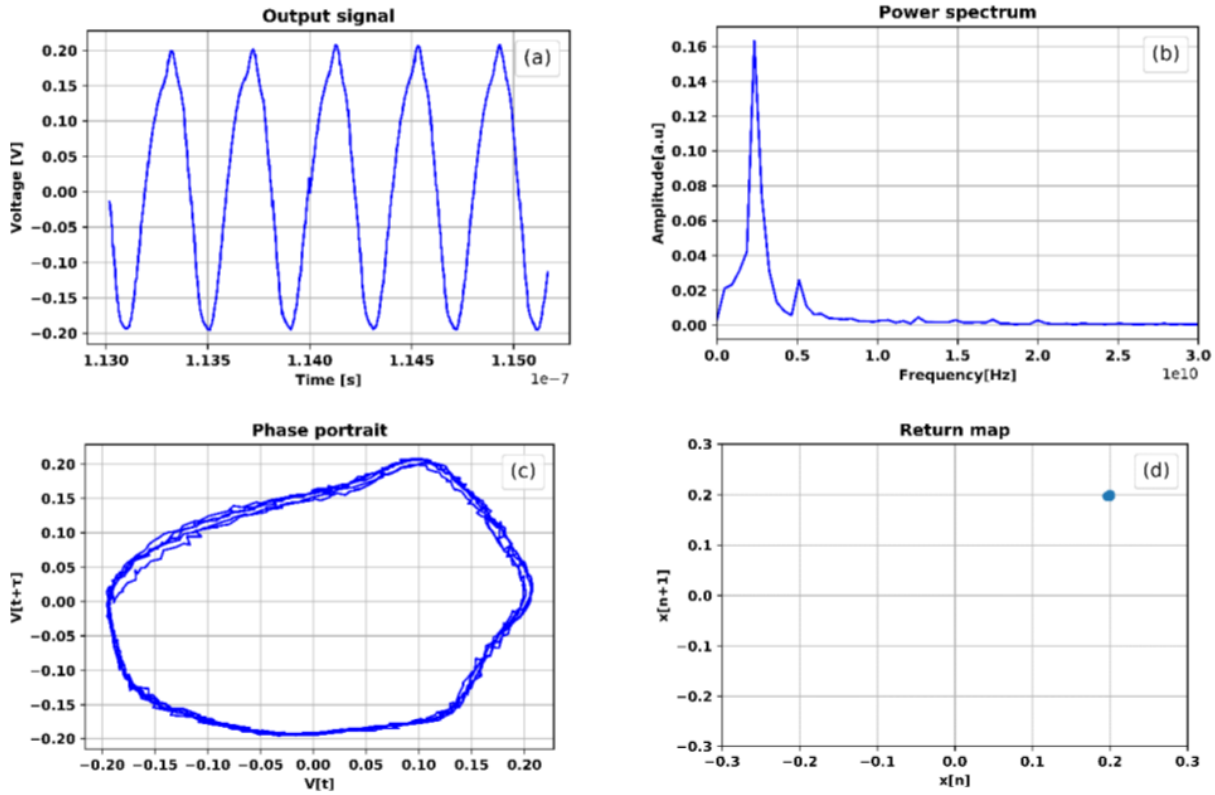

Figure 2.16 Single period output (a) Time series waveform at 2.5 GHz (b) Power spectrum (c) Phase portrait (d) Return map.

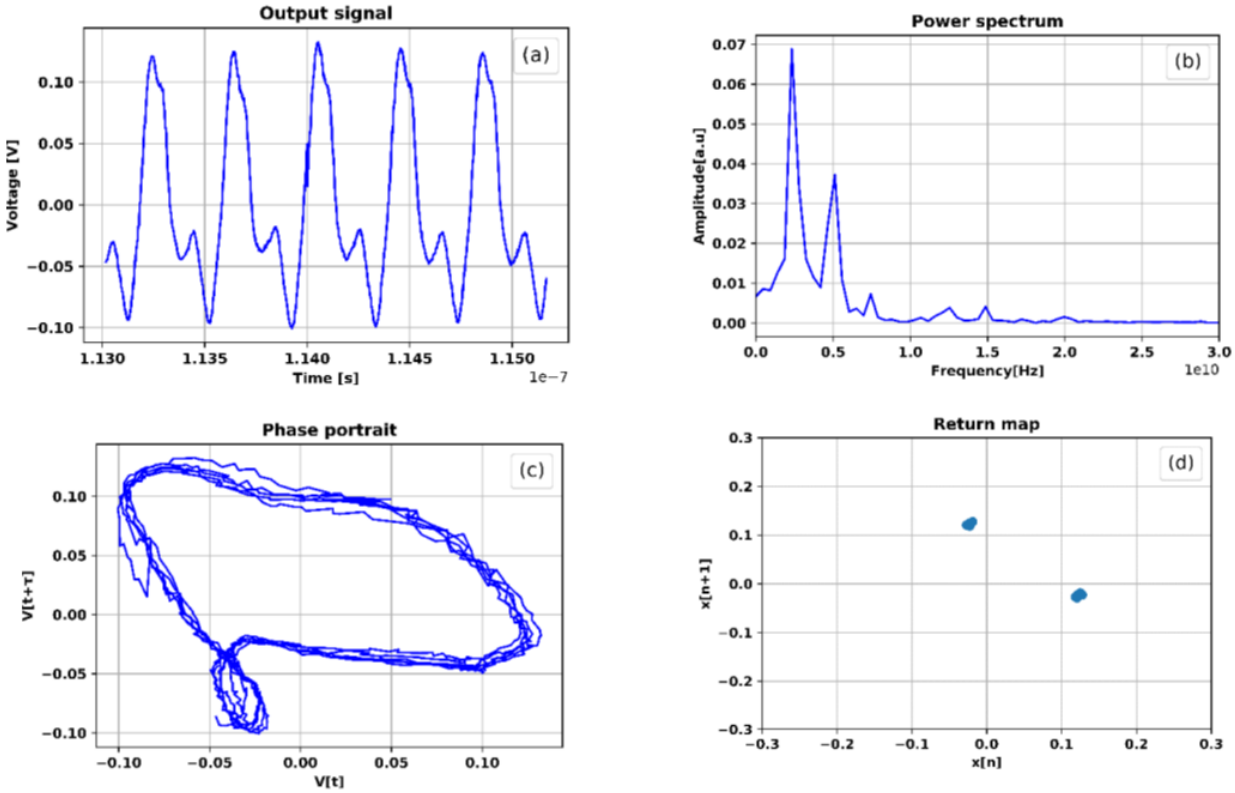

Figure 2.17 Double period output (a) Time series waveform 5 GHz (b) Power spectrum (c) Phase portrait (d) Return map.

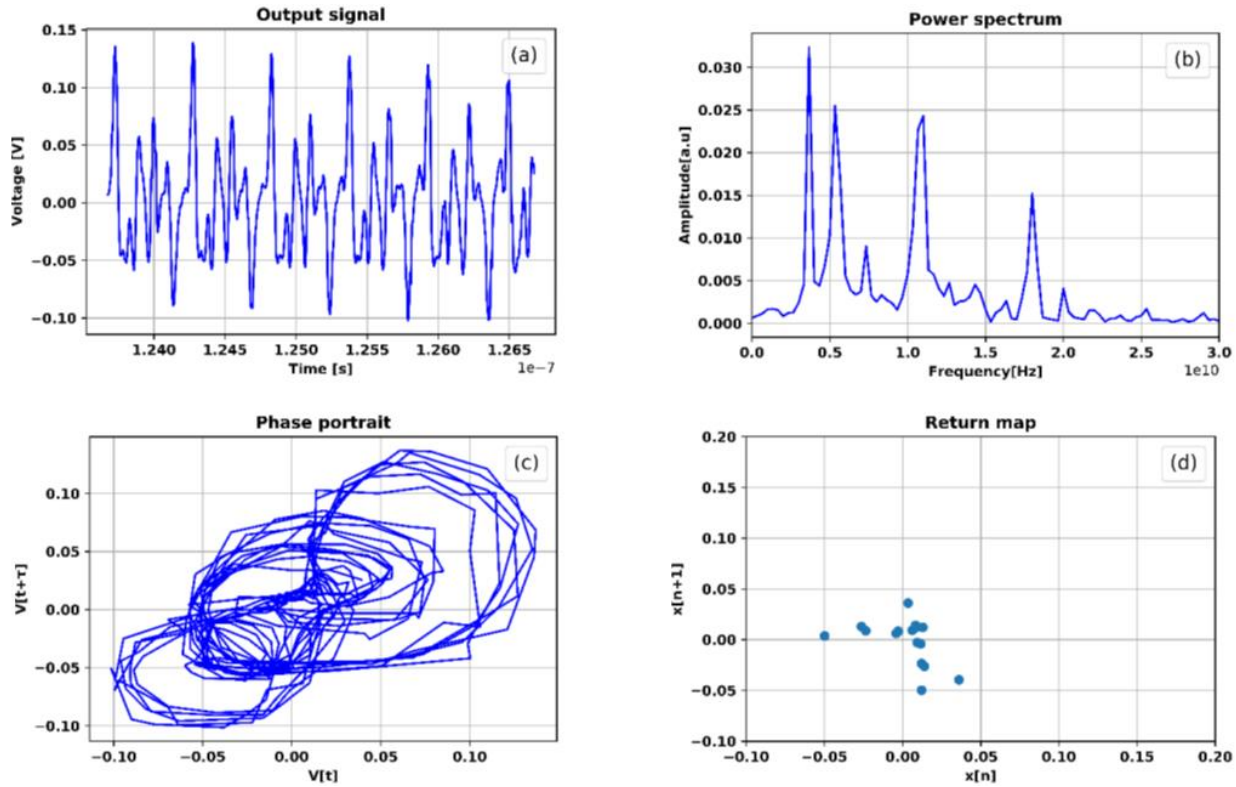

Figure 2.18 Chaotic output (a) Time series waveform at 5.46 GHz (b) Power spectrum (c) Phase portrait (d) Return map.

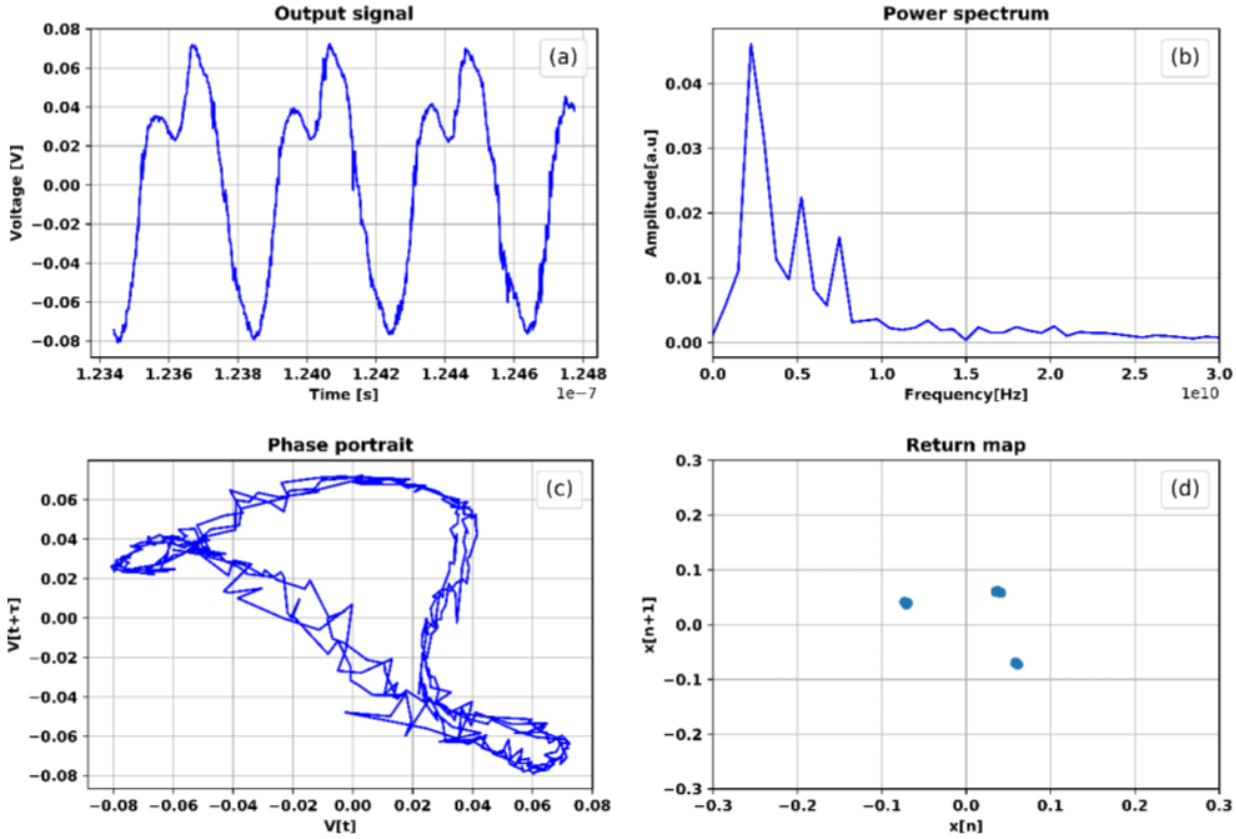

Figure 2.19 Triple period output (a) Time series waveform at 7.5 GHz (b) Power spectrum (c) Phase portrait (d) Return map

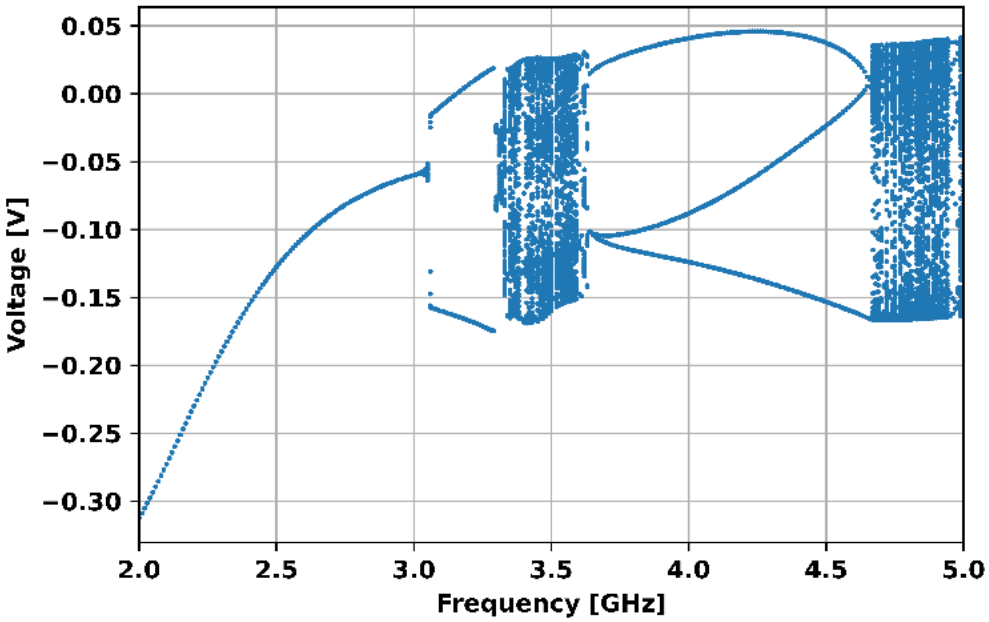

Figure 2.20 Simulated bifurcation diagram of the circuit including parasitic elements of the chip devices.

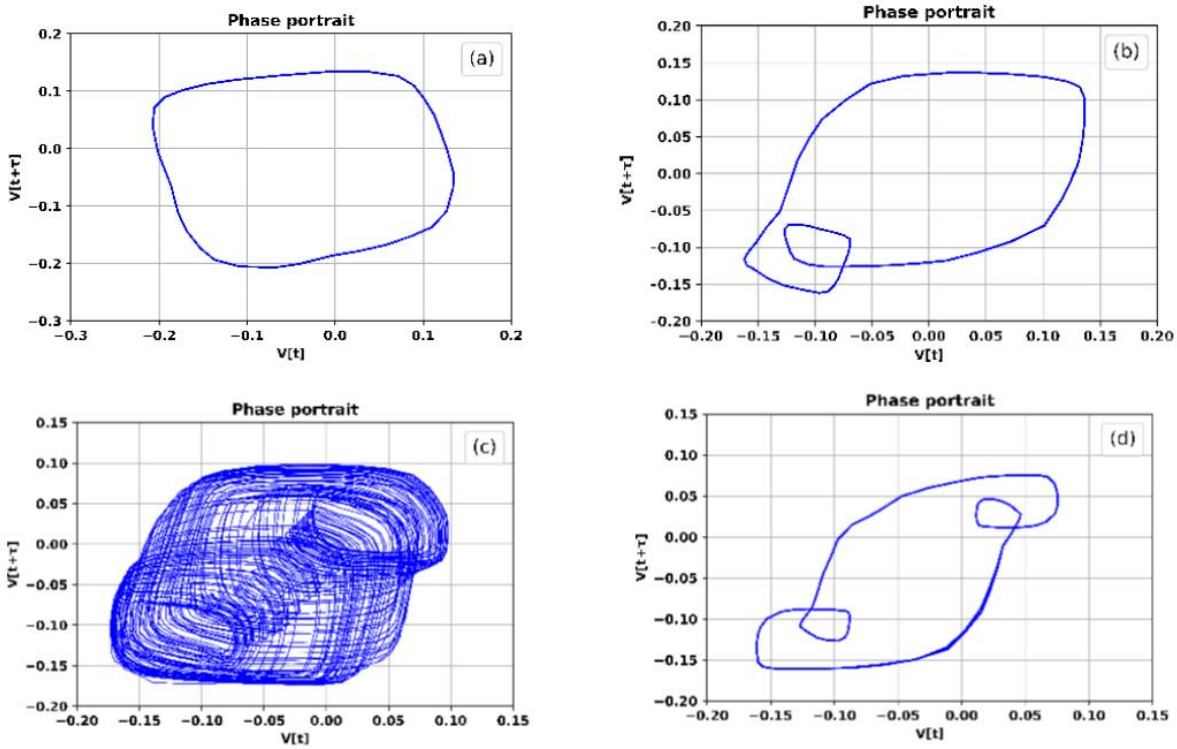

Figure 2.21 Phase portraits of each regime at various input frequency (a) single period output at 2.4GHz, (b) double period output at 3.1GHz (c) chaotic output at 3.55GHz (d) triple period output at 4GHz.

2.3.8 Summary

The resonant tunneling chaos generator circuit is demonstrated and characterized in depth at microwave frequency range. The circuit was fabricated on the PCB substrate employing the RTD chip and chip elements. This hybrid fabrication method proved to emulate the circuit as per circuit design without a long and complicated process while effectively reducing parasitic effects. Microwave chaos was controlled and visualized on the sampling oscilloscope using periodic reset technique in order to process data for detailed characterization. Longer period output up to 58 periods of input signal was achieved, which is approximately 3-times larger than those in the previous reports. This permits us to characterize output signals, in particular, calculation of Lyapunov exponents. I also found that the conventional methods of plotting bifurcation diagram from time series data failed due to frequency-dependent phase difference error. The proper bifurcation diagram was plotted using a compensation scheme based on the oscillation period in the conventional bifurcation diagram. A cascade of periodic and chaos regimes was exhibited on the experimental bifurcation diagram by sweeping input frequency from 2.4 GHz to 9 GHz. Single-period, double-period, chaos, and triple-period regimes were identified by plotting their time series waveforms, power spectrum, phase portraits, and return maps. The circuit's deterministic chaos was further proven by estimating the positive Lyapunov exponent from the time series waveform. These results indicate that the periodical resetting scheme should be a good tool for characterizing chaos in high-frequency regimes.

2.4 Nonlinear phenomena in RTD oscillators with a transmission line

2.4.1 Introduction

Transmission lines (TL) are an important component in the efficient transmission of electromagnetic waves from one place to another. They are critical in many applications, including telecommunications, power distribution, and signal transmission within electronic circuits [184], [185]. In high-frequency circuits and systems, the propagation delay introduced by TL is an important factor. This delay refers to the time it takes for the signal to travel from the input to the output of the TL and is affected by factors such as the physical length of the line, the dielectric material employed, and the conductor's geometry [186]. Chaos, caused by delayed feedback, shows up in a variety of physical systems like semiconductor lasers [187], microwave devices [188], and electronic circuits [189].

This study discusses the behavior of resonant tunneling diode (RTD) oscillators when a TL stub is added. It is important to note that the RTD is a two-terminal device, which has an inherent disadvantage. This can result in frequency fluctuations caused by changes in load impedance and spurious oscillations at the bias node [135–137]. In addition, the oscillator behavior is sensitive to the circuit patterns and wiring lines. In this section, the complex behavior is demonstrated, including chaos, that can occur in the RTD oscillators when a TL stub is introduced. The TL stub can be considered a delayed feedback unit that introduces a strong nonlinearity into the circuit, leading to chaos [190–193]. This mechanism is different from that discussed in section 2.3 and in previous papers [169], [170]. The circuit discussed in the previous studies is a forced van der Pol oscillator and produces complex signals due to the conflict between the external signal frequency

and the internal resonance frequency. On the other hand, the present circuit produces complex signals due to the conflict between the oscillation period and the delay time of the reflected signal in the TL stub. In addition to the mechanism, there is an important difference that affects the analysis of the circuit, namely, the present circuit is a self-oscillating circuit and it has no fixed reference frequency to sample the waveform signal. This difference makes the analysis of this circuit more difficult.

This type of simple and high-frequency chaos generator has the potential for various applications in the THz frequency range. On the other hand, understanding the effects of such a TL stub is also important for the design of THz circuits using RTDs. This is because even an extremely small stub can produce the nonlinear effects discussed in this paper. For example, a small anomaly in the circuit pattern, such as a stub-like protuberance, can produce such an effect. In addition, a short wiring line for an output or interconnect can produce similar effects due to reflection from an unavoidable impedance mismatch. In short, the importance of nonlinear phenomena increases at higher frequencies.

2.4.2 Basic behavior of the RTD oscillators with transmission line stub

The circuit being considered here is a free-running RTD oscillator with an open TL stub, as shown in Fig. 2.22. The oscillator circuit includes an RTD functioning as an NDR element, and a parallel connection of an inductor, L, and a capacitor, C, for the resonator. An open stub is connected to the resonator node. This simple stub produces complex behavior in the RTD oscillators via delayed feedback.

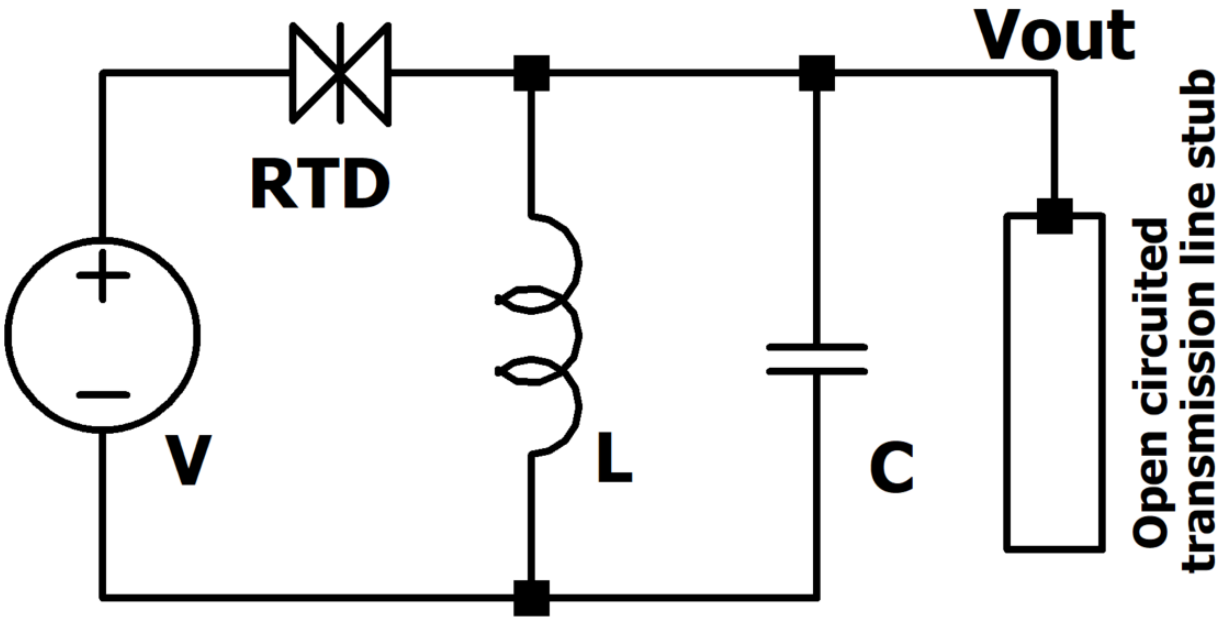

Figure 2.22 Basic circuit diagram of RTD-based oscillator along with an open TL stub

2.4.2.1 Circuit simulation

First, the effect of the TL stub on the RTD oscillators was investigated by performing the circuit simulation. A lossless TL model with 50 Ω characteristic impedance is used as an open stub, and

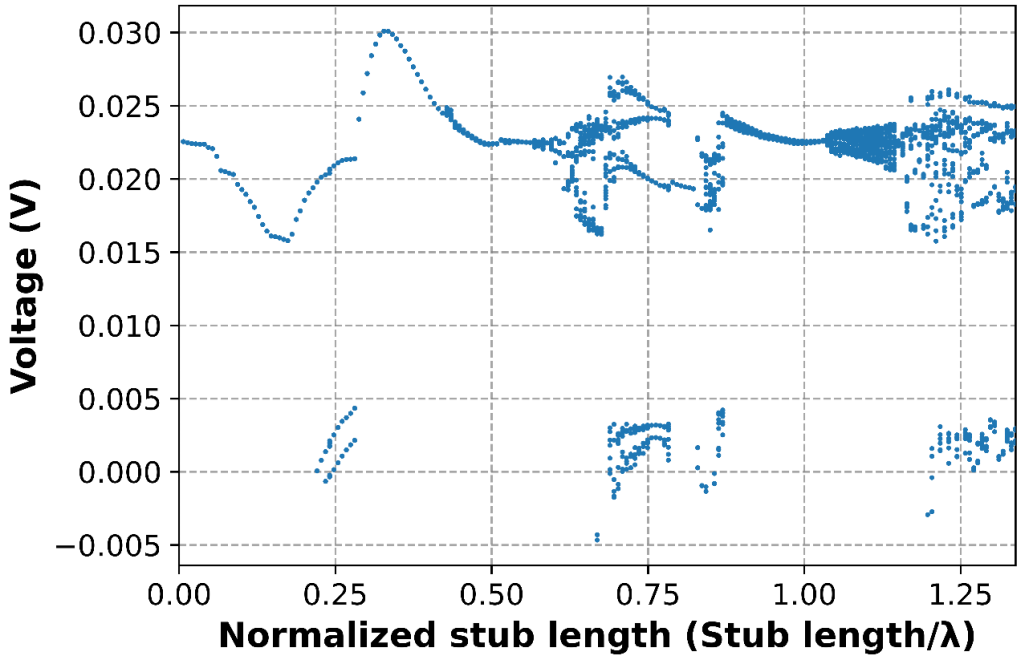

Figure 2.23 Simulation result of the bifurcation diagram of the RTD oscillator with an open-circuited stub. The inductance and capacitance used for the resonator were 4 nH and 0.3 pF, respectively.

a Schulman's I-V model [176] with similar characteristics to our RTD fabricated on an InP substrate. Characteristics of the RTD model are same as mentioned in section 2.2.2. This circuit was designed to oscillate at a low GHz frequency to match the experiment described in the next section, although a similar result is expected at much higher frequencies.

A DC bias voltage V_{bias} was applied to bias the RTD in its NDR region, resulting in the initiation of oscillations. The stub length was normalized to the wavelength of the fundamental frequency of the circuit without the stub (3.34 GHz). This bifurcation diagram plots the local maxima of the oscillation waveform at the given stub length. This sampling scheme is different from the conventional one elaborated in section 2.2.7.1, where the sampling is done with the period of the input frequency. This scheme is adopted because it is difficult to define the exact period because this circuit is a free-running oscillator, and the oscillation frequency changes as the TL length changes. In addition, to remove the effects of high-frequency noisy spikes caused by the sharp transition of the RTD current, the output signal was obtained through a low-pass filter (LPF) with the cutoff frequency set to a value slightly higher than the maximum oscillation frequencies. Despite this change, the characteristics of this bifurcation diagram are the same as the conventional

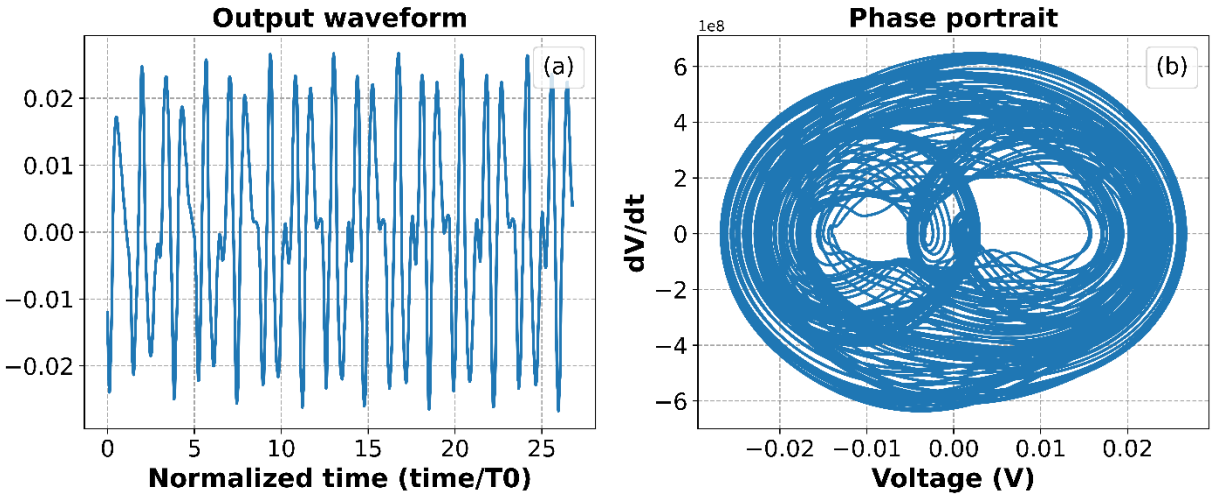

Figure 2.24 Chaotic output waveform and double scroll attractor. The normalized stub length is 0.681. L and C are the same as those for Fig. 2.23.

one, so that single oscillation gives one point, double period behavior gives two points, and so on. In particular, densely filled regions indicate complex signals, including chaos. This figure demonstrates that the RTD oscillator with an open TL stub shows various complex behaviors. Figure 2.24 (a) and (b) illustrate an example of the complex waveform and its phase portrait. The phase portrait displays a double scroll attractor, which is considered to be a signature of chaos [181].

It is worth noting that we have also confirmed by simulation that the short-circuited stub has the similar effects as the open stub. The difference is in the reflection phase, and roughly speaking, the short stub with twice the stub length has a similar effect as the open stub. We also note that the phenomena discussed in this paper can take place in the THz oscillators, since the same equivalent circuit well describes the operation of the oscillators in the THz frequency range [194].

2.4.3 Experiments

2.4.3.1 Experimental circuit design

The under-consideration circuit is a self-oscillating circuit that produces complex output signals including chaos. As stated earlier in section 2.2.3, it is difficult to observe complex, non-periodic

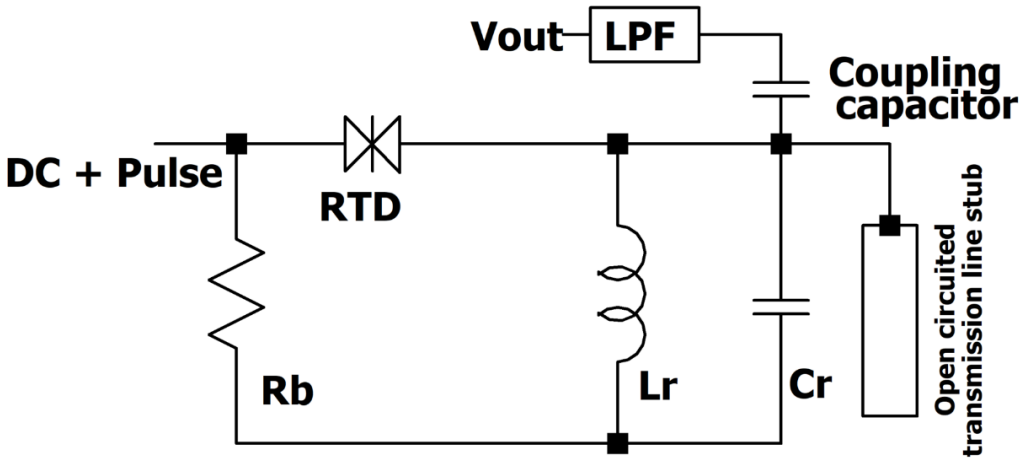

Figure 2.25 Circuit design for measuring the high frequency chaotic waveforms generated by the RTD based self-oscillators with open stub.

signals, such as chaos, using a sampling oscilloscope. So, the same experimental technique is adopted to visualize the output signals. This circuit produces chaos without introducing an external sinusoidal forcing signal. Consequently, the oscillation frequency is not synchronized, rendering the observation of output waveforms on the sampling oscilloscope more challenging. Furthermore, various parasitic effects also restrict the observation of the actual results. To overcome such impediments, an experimental circuit is designed as shown in Fig. 2.25. The operating principle of the circuit is again interpreted here.

The DC signal in conjunction with the pulse signal is injected which enables the bias voltage to enter and exit the NDR region of the RTD. The RTD oscillator then switches between oscillating and non-oscillating states, producing a train of high-frequency pulses (THFP). As a result, the waveforms of THFP can be easily observed on a sampling oscilloscope. A shunt resistor R_b is added to the bias side of the RTD oscillator circuit in order to suppress the spurious oscillations generated by the RTD. A coupling capacitor followed by a low pass filter (LPF) is connected at

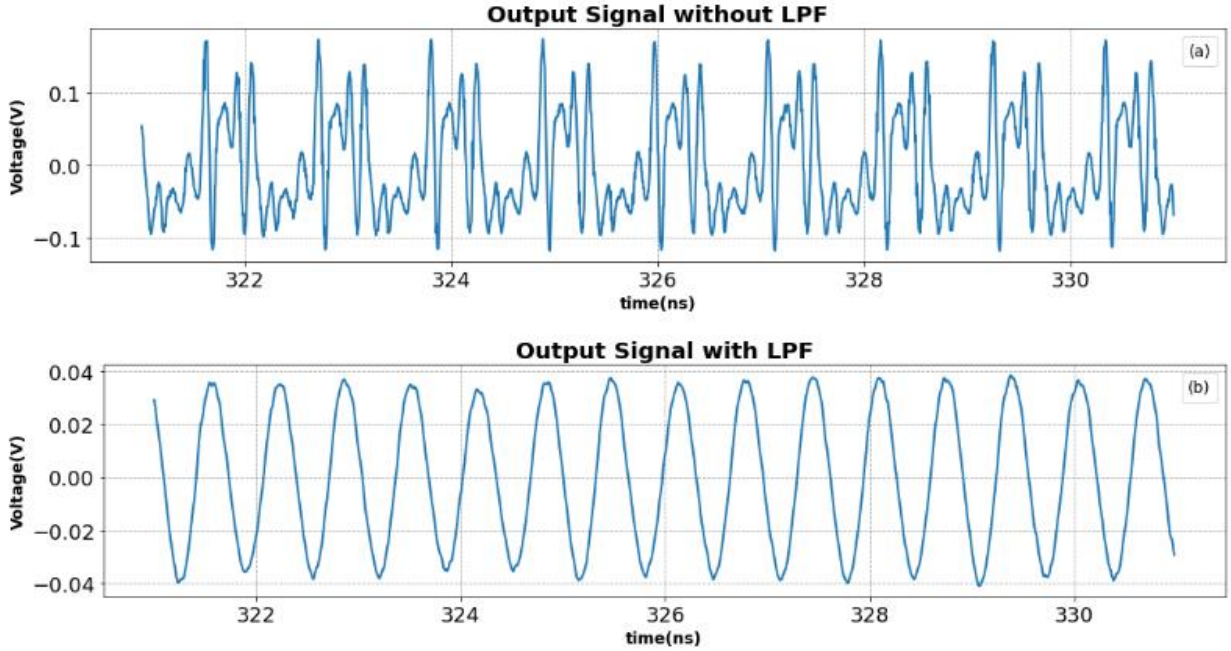

Figure 2.26 Output waveforms (a) without using LPF (b) Using LPF

the output node which facilitates the transfer of output signals to the measuring devices. The RTDs possess very strong non-linear I-V characteristics that generate very high-frequency components in the output signals. Due to these high-frequency components, output waveforms contain sharp spikes that impede the observation of fundamental signals. To eliminate such spikes, high-frequency components should be eliminated. For this reason, an LPF is used at the output port. The output waveform with and without LPF is shown in Fig. 2.26.

2.4.3.2 Oscillator fabrication

To confirm the results of the above simulation, we fabricated and tested the RTD oscillator with an open TL stub as shown in Fig. 2.27. For ease of measurements, the resonant frequency was designed in the low microwave frequency range. The circuit was fabricated using a hybrid integration approach on a 0.8 mm double-sided glass-epoxy FR-4 printed circuit board (PCB) by integrating commercially available 1.0 mm×0.5 mm chip elements and the in-house fabricated

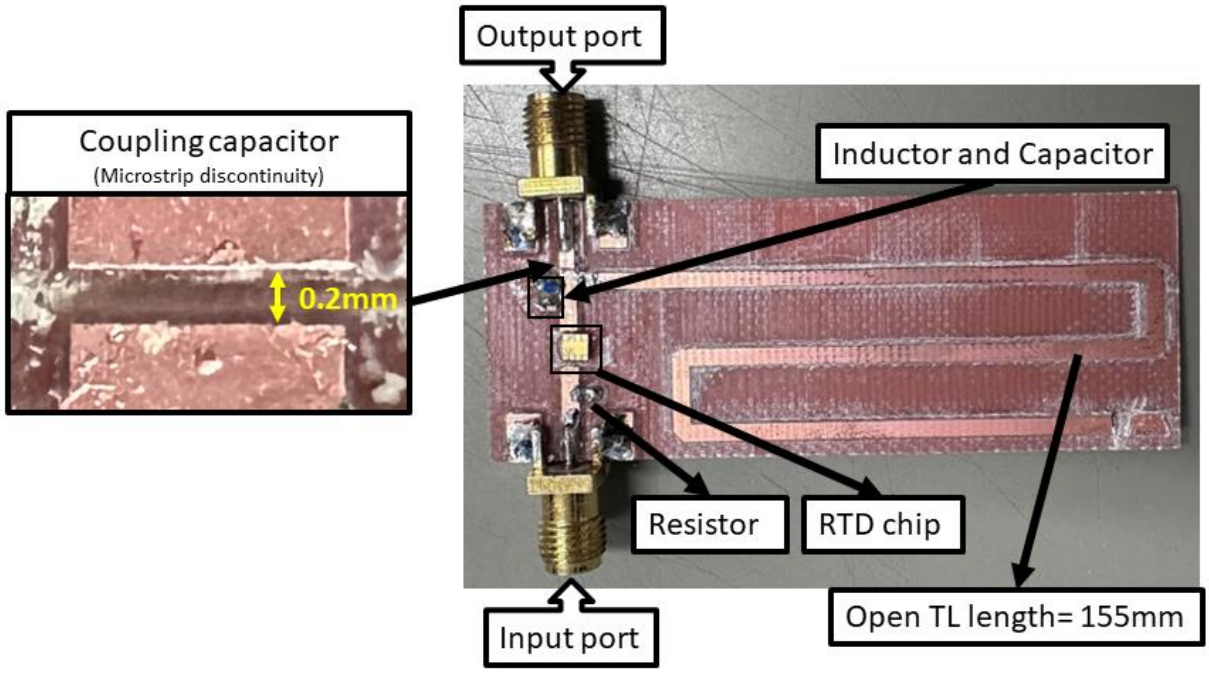

Figure 2.27 Prototype circuit to observe the effects of an open stub on the RTD oscillators. The inductance and capacitance used for the resonator were 4 nH and 0.3 pF, respectively. The output port was coupled to the oscillator node via a gap capacitor of approximately 41 fF, as shown in the left figure.

RTD chip. The connection of the RTD to the circuit was facilitated by the bonding wires. Multiple bonding wires were used to reduce their impedance. The oscillation waveforms were observed through the output port, which was coupled to the resonator node via a small capacitor. To avoid spurious oscillations, the bias stabilization resistor of 5 Ω was inserted between the bias node and the ground. The maximum length of the open stub is equal to approximately 1.3 times the wavelength of the fundamental oscillation without the stub.

2.4.3.3 Experimental setup

It is difficult to observe complex, non-periodic signals, such as chaos, using a sampling oscilloscope. Employing the proposed experimental technique for observing high frequency, the experimental setup is illustrated in Fig. 2.28. The circuit is powered by DC bias voltages in conjunction with the train of pulses generated by the pulse pattern generator (ANRITSU

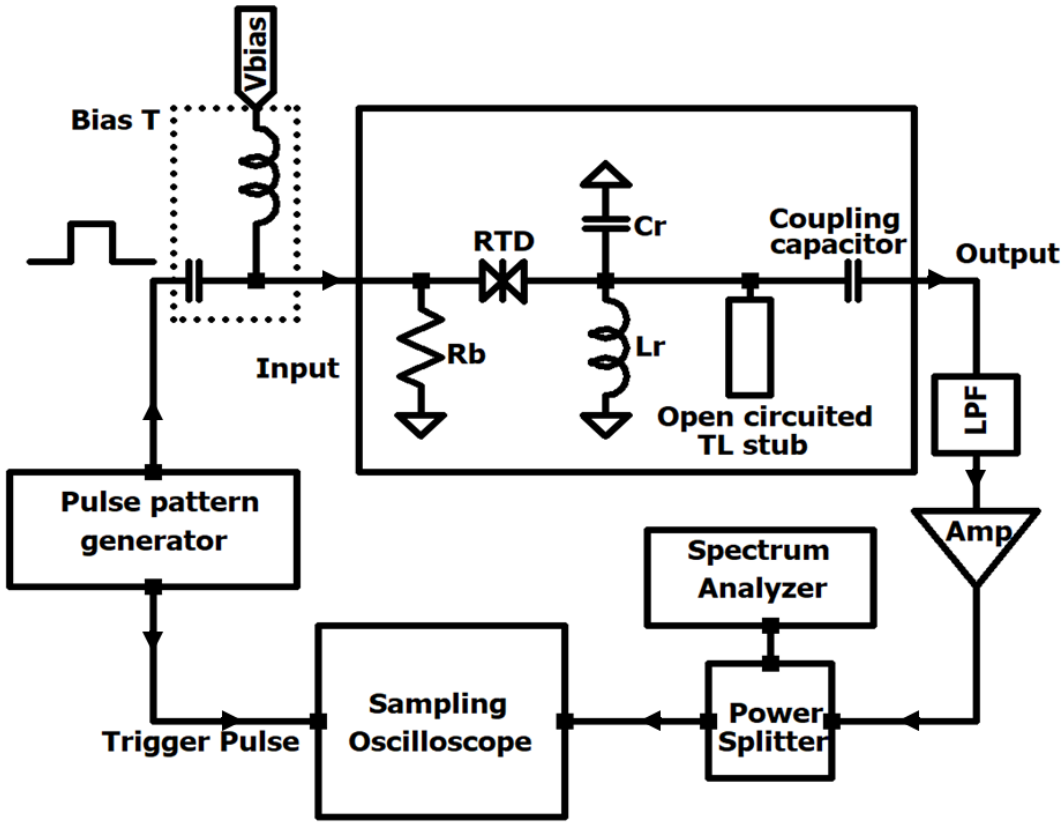

Figure 2.28 Experimental configuration for directly observing high frequency non-periodic output signal waveforms.

MP1761C) through Bias T. These pulses periodically reset the oscillator and allow the waveform to be observed with a sampling oscilloscope. The output signal was filtered by LPF. This is indispensable because the output signal contains many high-frequency components due to the strong nonlinearity of the RTD. These high-frequency components disturb observation of the essential behavior of the oscillator. The coupling of the output port is very weak to eliminate the effect of the measuring system on the circuit behavior. So, I use a microwave system amplifier (Agilent, 83017A) after LPF to amplify the output. A power splitter is inserted to simultaneously investigate the output waveforms on the sampling oscilloscope (Hewlett Packard 54750A) and frequency spectrum of signals on the spectrum analyzer (Agilent, 8565EC). The trigger pulse is facilitated by the pulse pattern generator to the sampling oscilloscope. For synchronizing the sampling process with output signals, a trigger pulse is necessary for reconstructing and displaying the waveforms accurately on the sampling oscilloscope. So, the trigger pulse is facilitated by a pulse pattern generator to the sampling oscilloscope. All instruments were connected to a computer for digital data acquisition.

2.4.3.4 Results and discussion

The fabricated circuit without the stub oscillated at about 1.41 GHz under DC bias of 1040 mV. To visualize the output waveforms, we injected an 80 MHz pulse accompanied by a DC bias voltages of 880 mV. To find the effects of the open stub on the RTD oscillators, the length of the open stub was changed 48 times by sequentially cutting 3 mm/5 mm length from the open end side employing a metal guide cutter. Detailed analysis of the output waveforms was then performed after each cut. By accumulating all the output waveforms acquired from the sampling oscilloscope, the bifurcation diagram was plotted by finding local maxima as shown in Fig. 2.29. A region of multiple dots indicates complex output, while distinct dots indicate periodic output, which can be single period, double period, and so on.

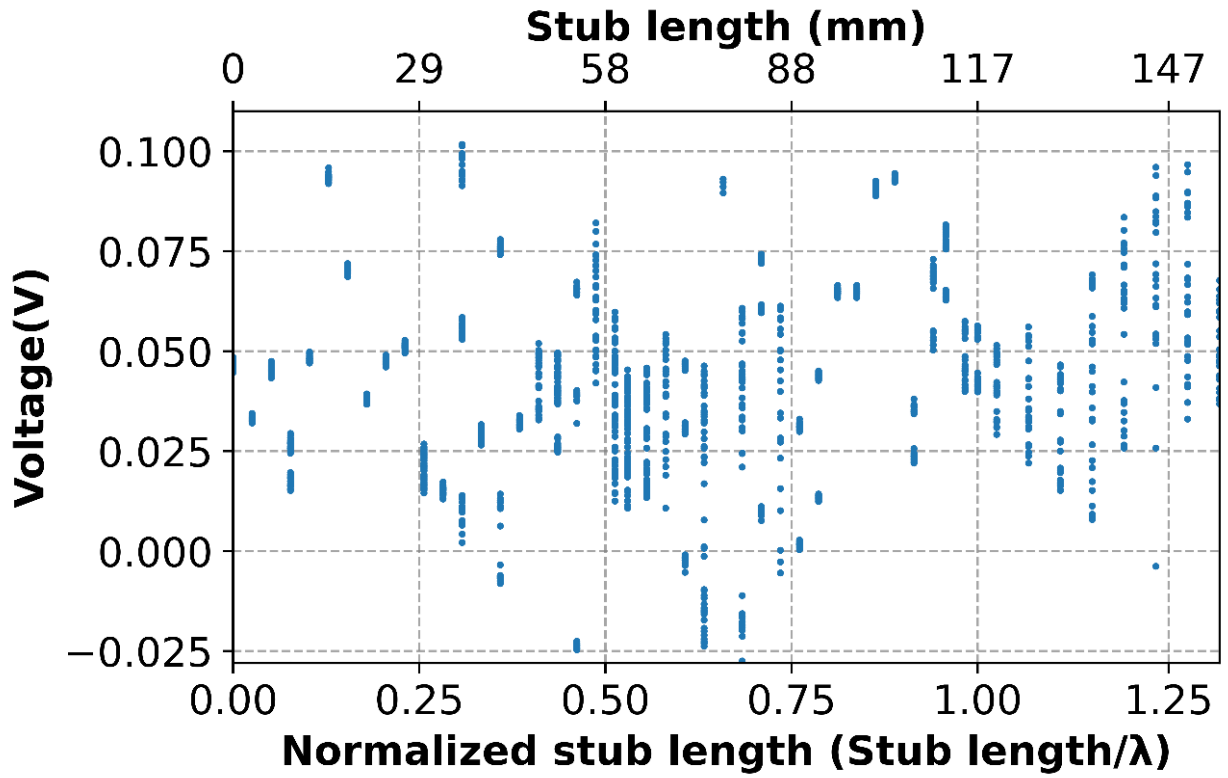

Figure 2.29 Experimental bifurcation diagram plotted by varying the open stub length. The stub length is normalized to the wavelength of the oscillation without the stub.

The experimental bifurcation diagram in Fig. 2.29 looks somewhat different from the simulated one in Fig. 2.23, however, they have important similarities. First, both bifurcation diagrams consist of complex behaviors unique to nonlinear systems. Next, for normalized stub lengths less than about 0.5, the output is rather simple, consisting of small-period behaviors. Then, for normalized stub lengths greater than 0.5, more complex and non-periodic behaviors appear. In addition, the dense region, which implies chaos or quasiperiodic behavior, seems to appear intermittently as the stub length increases. It should be emphasized that the experimental circuit is affected by many parasitic elements. Such elements should cause large differences in the bifurcation diagram.

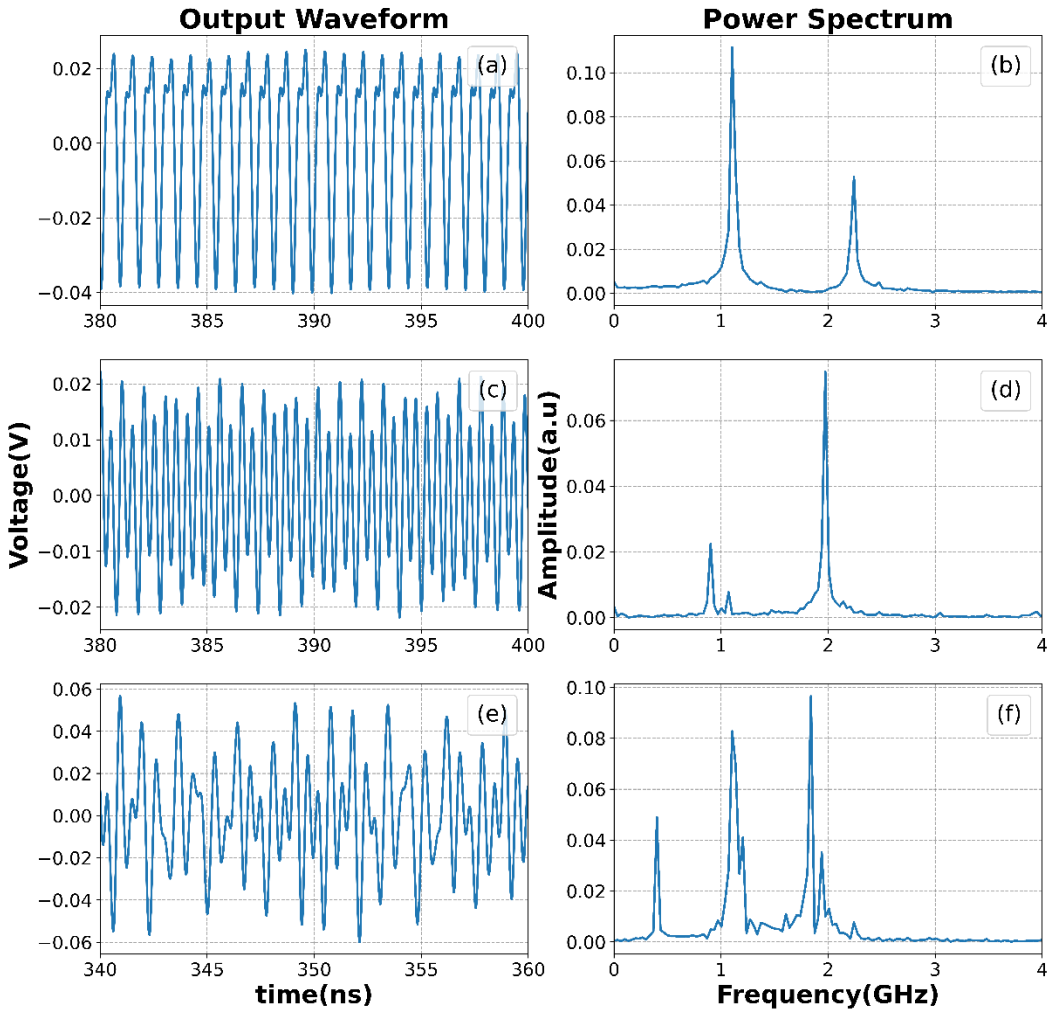

Figure 2.30 Examples of experimentally obtained waveforms with their spectrum for various TL lengths. The stub length and its normalized values are (a), (b) 9 mm, 0.0769, (c), (d) 30 mm, 0.256, and (e), (f) 86 mm, 0.735, respectively.

Figure 2.30 shows examples of the experimentally obtained waveforms with their spectrum. Various types of waveforms were observed in this circuit depending on the stub length. The double period behavior is shown in Fig. 2.30 (a), while the non-periodic signals are shown in Fig. 2.30 (c) and (e). It should be noted here that the small TL length of 9 mm, which is about 1/13 of the wavelength of the fundamental oscillation frequency, can cause signal modulation..

To further identify the nature of the output waveforms, we reconstructed the phase portrait using the time delay method [179] by taking $V\,(t)$ on the x-axis and $V\,(t+\tau)$ on the y-axis. Temporal data were interpolated to smooth the data for clear display of the waveforms and phase portraits. Figure 2.31 shows phase portraits obtained from the waveforms shown in Fig. 2.30 (c) and (e). Both signals are non-periodic and look random. However, the phase portraits are quite different for each other. The phase portrait for a stub length of 30 mm shows a quasi-periodic attractor, and that for 86 mm shows a very clear double scroll attractor which is considered to be the signature of deterministic chaos [181]. The Lyapunov exponents (λ_{max}) were also estimated using the Wolf method [183] for 86 mm, and the largest value obtained was 0.0142. The positive value of λ_{max} is the confirmation of chaos.

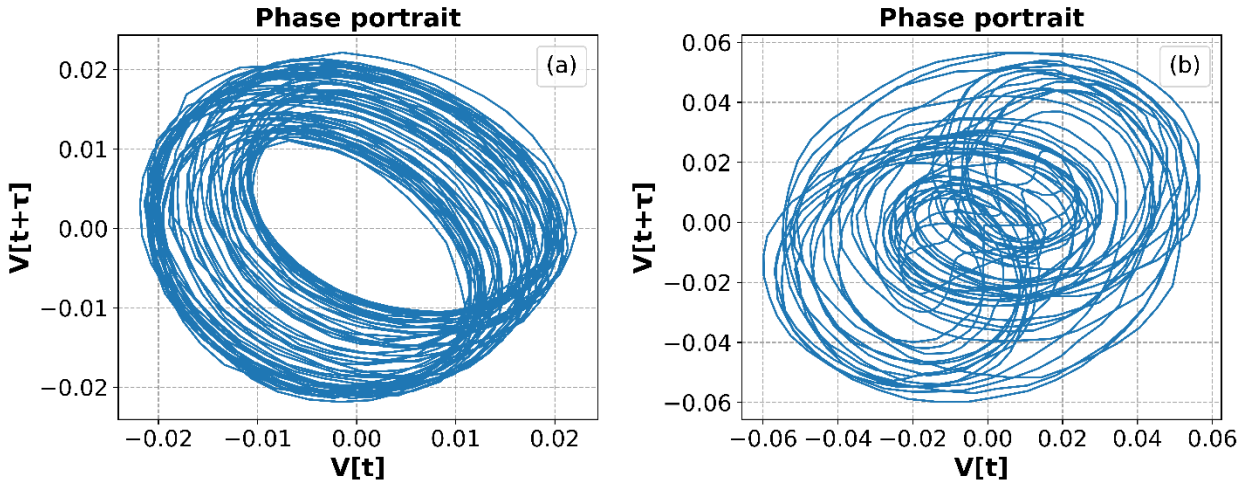

Figure 2.31 Phase portraits of the experimentally obtained waveforms. (a) stub length=30mm, (b) stub length=86mm.

Finally, we will briefly discuss the origin of the complex behaviors shown here. As described earlier, these phenomena can probably be explained by the ratio of the delay time to the period of the oscillation frequency, and their locking and unlocking. The intermittent appearance of the non-periodic region in Fig. 2.23 and 2.29 should be a result of this mechanism. However, it is more complicated because the oscillation frequency itself changes depending on the TL length. The detailed discussion is beyond the scope of this paper, and further studies are needed.

2.4.4 Summary

The behavior of RTD oscillators with an open TL stub was investigated as a function of the stub length. First, a circuit simulation was performed to clarify the basic phenomena caused by the stub. It was found that the open stub induces strong nonlinearities in the RTD oscillators, leading to the evolution of complex behavior, including chaos.

To confirm the simulation results, we fabricated and tested RTD oscillators with an open TL stub. The circuit was fabricated using a hybrid integration technique. The experimental results showed chaotic and periodic output waveforms by varying the open stub length. Consequently, this circuit has potential as a simple chaos generator in the THz frequency range. Moreover, understanding the effects of such a TL stub is also important for the design of THz circuits using RTDs, since even a small metal pattern or interconnection wires can cause such a feedback effect in the THz frequency range.

2.5 Eliminating nonlinearities in RTD oscillators caused by TL

The nonlinearities caused by the TL pose a barrier to using RTD oscillators in sensor applications. These nonlinearities can significantly affect the sensor's performance. To apply RTD oscillators to sensors effectively, it is crucial to eliminate these nonlinear effects. So, from simulation and experimental results, It has been found that the LC ratio of the resonator, characteristic impedance $Z = \sqrt{\frac{L}{C}}$, play a crucial role in generating/eliminating the nonlinearities upon changing the open stub length. Choosing a low characteristic impedance of the resonator circuit can significantly reduce the nonlinearities caused by TL.

2.5.1 Simulation results

I simulate the basic circuit shown in section 2.4.2 by keeping the operating conditions the same other than the LC value of the resonator. I chose a relatively low LC resonator characteristic impedance of 11.83 Ω, using a 1.4 nH inductor and a 10 pF capacitor. In addition, to remove the effects of high-frequency noisy spikes caused by the sharp transition of the RTD current, the output signal was obtained through a low-pass filter (LPF) with the cutoff frequency set to a value slightly

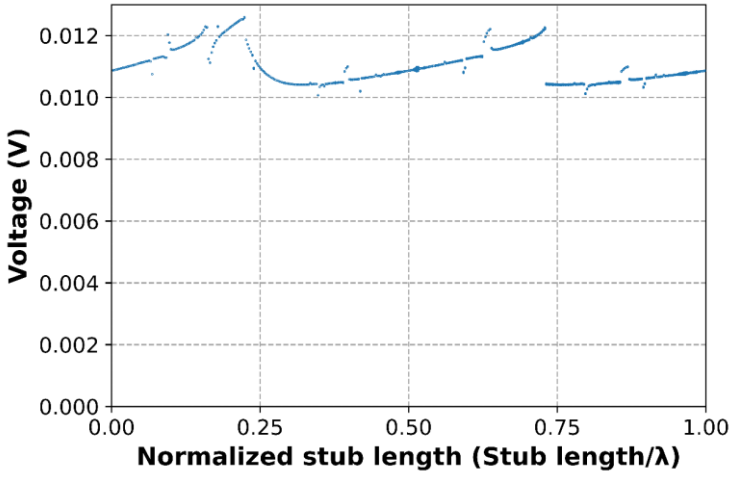

Figure 2.32 Simulation result of the bifurcation diagram of the RTD oscillator with an open-circuited stub. The inductance and capacitance used for the resonator were 1.4 nH and 10 pF, respectively. The characteristic impedance is 11.83 Ω which is comparatively low.

higher than the maximum oscillation frequencies. Figure 2.32 depicts the bifurcation diagram plotted by sweeping the stub length in terms of time delay. Here, the stub length is normalized with the wavelength (λ) and the λ is 758 ps which is equivalent to the time period of the fundamental frequency which is 1.32 GHz. There is a dominancy of solid distinct lines in the bifurcation diagram indicating periodic output. So, it depicts that keeping the characteristic impedance of the LC resonator circuit low significantly reduces the nonlinearities due to the TL stub and such circuits are not that sensitive to the length of the open TL stub. Conversely, circuits with high characteristic impedance of resonators tend to exhibit rather complex behavior which can be seen in section 2.4 where the characteristic impedance of resonator was 115.47 Ω.

2.5.2 Experimental results

Simulation results were further verified by fabricating a prototype circuit along with circuit parameters shown in Fig. 2.33. The circuit fabrication method is the same as I used previously in section 2.4.

A thorough investigation of a circuit characterized by the low characteristic impedance of the LC resonator was performed. It functions as a harmonic oscillator and exhibits stable oscillations at 0.833 GHz while maintaining the same operating conditions and experimental setup as the preceding circuit. The stub length of 180 mm was chosen with the assumption that the circuit would oscillate at a frequency of 1 GHz. At this frequency, a 180 mm length is estimated to be

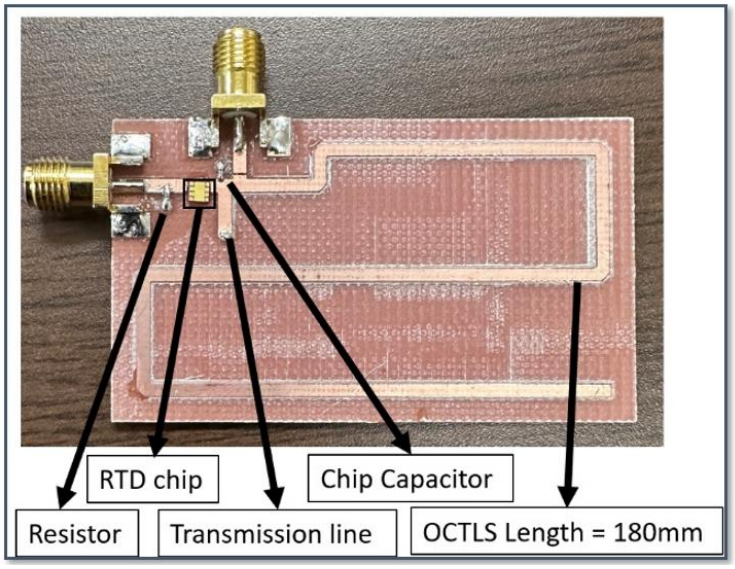

Circuit parameters	
Resistor (R_{sup})	5Ω
Chip capacitor (C_r)	10pF
Transmission line (L_r)	50Ω, 4.5mm, 1.4nH
Stub length	50Ω,180mm

Figure 2.33 Prototype circuit fabricated on the PCB substrate along with circuit parameters by choosing relative low resonator characteristic impedance, 11.83 Ω.

equivalent to one wavelength. However, due to parasitic effects, the circuit actually oscillates at 0.833 GHz. Therefore, the wavelength (λ) for normalization was estimated to be 200 mm.

The open stub with a length of 180 mm cuts 38 times by randomly reducing length aiming to govern the behavior with comparatively minor modifications. Then accumulating all the output waveforms, the bifurcation diagram is plotted which depicts almost periodic output with no complexity as shown in Fig. 2.34. It can be seen that the nonlinearities induced by open stubs are also affected by the characteristic impedance of the LC resonator. So, it is concluded that the nonlinearities due to TL can be significantly eliminated by choosing the low resonator characteristic impedance. However, variation of output power and change in fundamental

frequency was observed both in simulation and experiments. Variation of output power can be attributed to the reflection of signal with constructive and destructive interference.

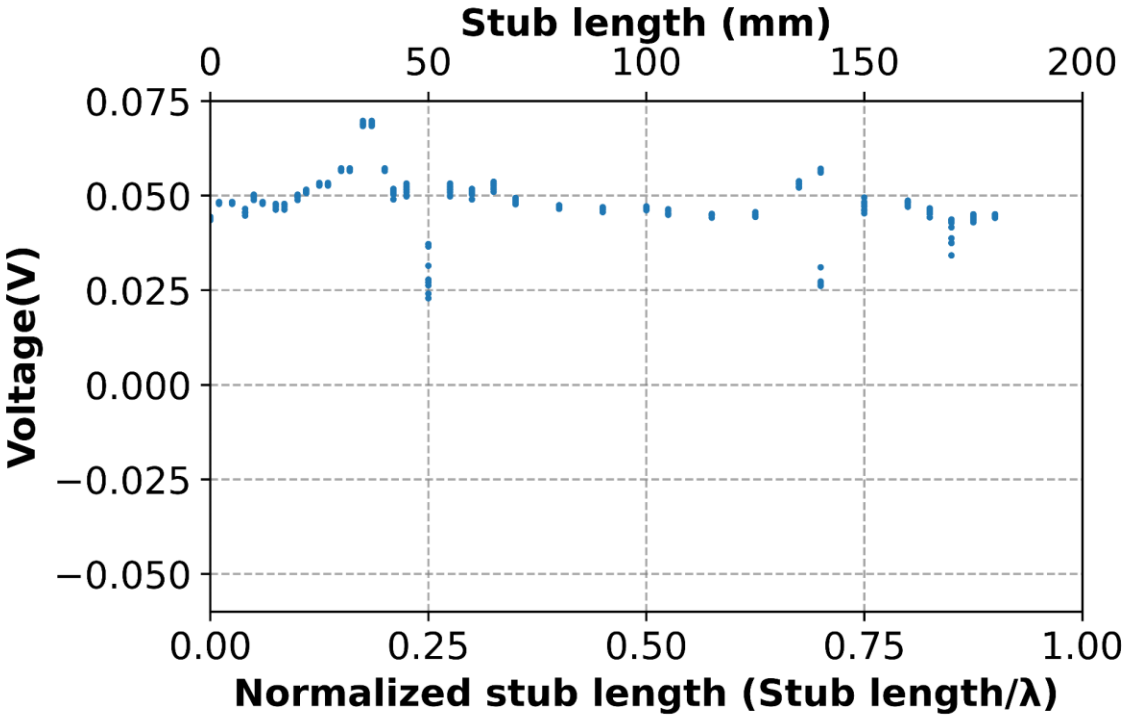

Figure 2.34 Experimental bifurcation diagram plotted by varying the open stub length. The stub length is normalized to the wavelength of the oscillation without the stub.

Chapter 3 Frequency Delta Sigma Modulation Sensors based on high-frequency oscillators

3.1 Introduction

Currently, many modern systems operate using digital signals. So, analog-to-digital (AD) conversion is vital for sensors to ensure compatibility with digital systems, improve accuracy, enable signal processing, facilitate communication with digital interfaces, and enhance the versatility of sensor data. For high-performance sensors, superior analog-to-digital converters (ADCs) are necessary. Among a variety of ADCs, a delta-sigma modulation analog-to-digital converter (DSADC) is prioritized for high-resolution applications. DSADC has the advantage that high-speed operation is directly linked to high-precision AD conversion and facilitates high dynamic range owing to oversampling and noise shaping. It does not require high-accuracy analog circuitry [195–198]. A conventional DSADC has an integrator, a 1-bit quantizer, and a feedback digital-to-analog converter. The integrator and feedback digital-to-analog converter (DAC), in particular, limit the sampling rate and hence bandwidth. A frequency delta-sigma modulator (FDSM) [26], [27] is an interesting substitute for the conventional delta-sigma modulator (DSM). The FDSM is based on a voltage-controlled oscillator (VCO), which converts the input analog signal into the frequency-modulated (FM) intermediate signal. The FM signal can be easily converted to the pulse density modulated (PDM) digital signal with a simple digital circuit consisting of a register and an XOR. The FDSM is suitable for high-frequency operation because it has no feedback loop and no DAC, which restricts the operation frequency. As a result, it is possible to execute AD conversion with an even broader bandwidth, larger dynamic range, higher SNR, and higher resolution [198–202]. Moreover, if the VCO is replaced by a variable frequency

oscillator whose oscillation frequency is dependent on the external physical quantity to be sensed, high-performance sensors become possible. As stated in the following sections, the performance of the FDSM is significantly reliant on the oscillation frequency of the VCO, employing the RTD oscillators for this technique is quite promising.

This chapter includes a brief description of the operating principle of AD converters, the characteristics of DSADC, and the significance of the FDSM technique for high-frequency and high-performance sensors. Furthermore, FDSM based stylus surface profiler is provided to highlight the high-frequency operation and wide dynamic range of this promising AD technique.

3.2 AD convertors

3.2.1 Principle of AD converters

An analog signal is a signal in which a certain physical quantity is replaced with another continuous quantity (for example, an electrical signal in an electrical circuit), whereas a digital signal is a signal in which a certain physical quantity is replaced with a discrete value [203]. An ADC converts

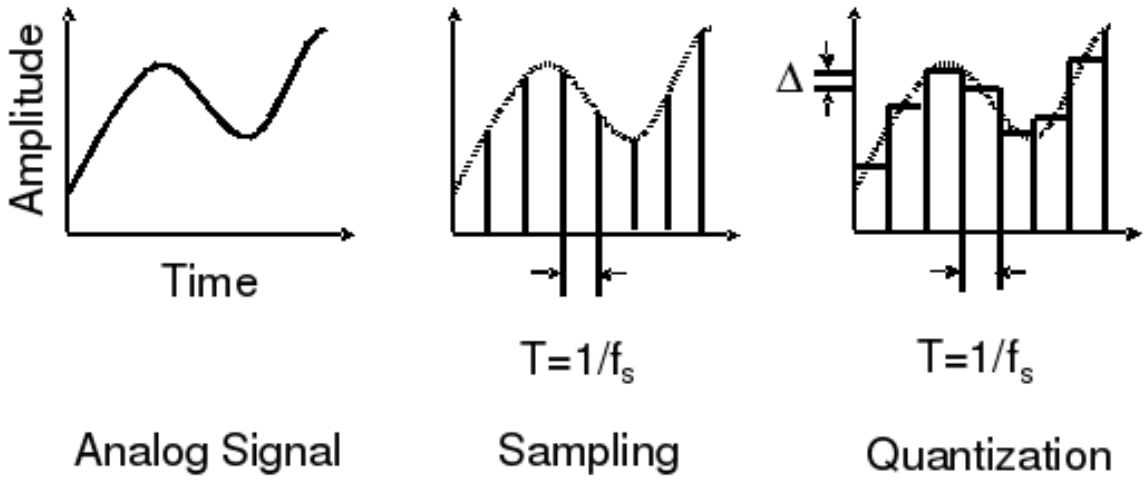

Figure 3.1 AD conversion flow of a digital signal

this analog signal into a digital signal [204]. AD conversion is performed through two steps: sampling, which discretizes the signal in the time domain, and quantization, which discretizes in the amplitude domain [205]. Figure 3.1 shows the flow of AD conversion in the time domain [195].

3.2.2 Sampling and aliasing

In AD conversion, first, a continuous analog signal is divided into fixed periods T, thereby discretizing it in the time domain. This is called sampling. Here, the reciprocal of the period 1/T is called the sampling frequency and is generally expressed as f_s. If a continuous-time signal whose frequency is limited to less than f_0 and sampled with $f_s > 2f_0$, the original signal can be completely reproduced from the resulting sampling sequence (The Nyquist-Shannon Sampling Theorem). The lower limit of this sampling frequency, $2f_0$, is called the Nyquist frequency f_N [206].

When sampling is performed at the sampling frequency f_s, a signal whose frequency is folded back at $f_s/2$ appears on the frequency axis. When sampling at $f_s<2f_0$ (down sampling), the original signal component and the folded signal component overlap, causing interference in the output signal. It

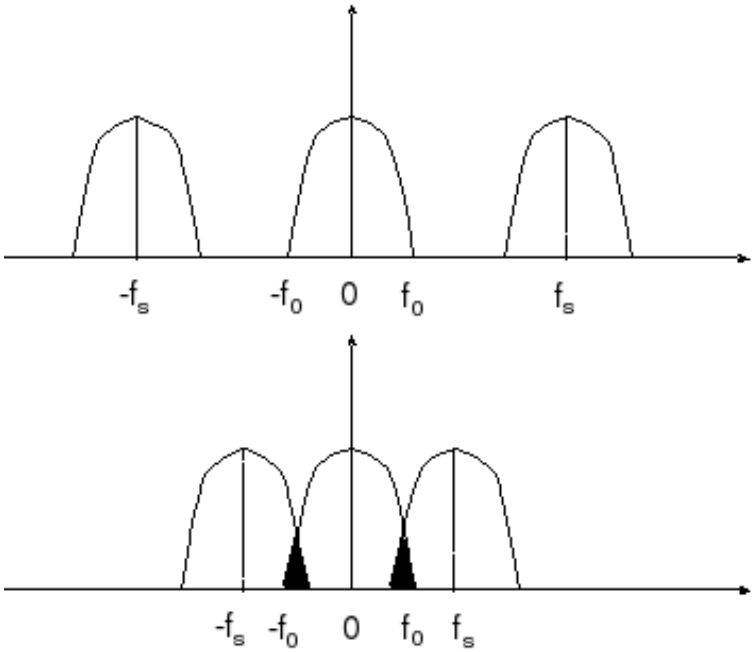

Figure 3.2 Aliasing: spectrum in case of sampled signal at $f_s<2f_0$

is impossible to recover the original signal from this sampled value. This is called folded distortion (aliasing) [207] and is illustrated in Fig. 3.2.

If there is high-frequency noise in the signal to be sampled, even if sampling is performed with $f_s > 2f_0$, aliasing will occur because frequency components (noise) above f_0 overlap when folded back. To prevent this aliasing, a low-pass filter must be used to remove frequency components above f_0 (= $f_s/2$). This filter is called an anti-aliasing filter [207–209]. And since this filter is required before the signal is sampled, it is always an analog filter. However, high-order analog filters cause phase distortion called group delay. Therefore, oversampling techniques are used. Oversampling means sampling at a frequency that is sufficiently higher than the Nyquist frequency $2f_0$ [206], and as a result, the aliased signal is largely separated, allowing a margin in the frequency band of the analog filter [207], [208]. Furthermore, by using oversampling, high resolution can be obtained. Details regarding this will be discussed in section 3.2.4.

3.2.3 Quantization

In AD conversion, after sampling, the amplitude value is discretized by quantization and a digital value is output [208]. Digital values are generally discrete values that are equally spaced, and the smallest unit is called resolution. Quantization creates an error between continuous analog amplitude values and discrete digital amplitude values. This is an intrinsic noise in AD conversion and is called quantization noise [209], [210]. For inputs that go back and forth between many quantization steps, the quantization noise becomes a white noise that is uncorrelated with the input. Furthermore, even if the quantization noise has a correlation with the input, it can be uncorrelated by adding an appropriate dither. A simple dithering method is to add a small amount of random noise in parallel to the input [211].

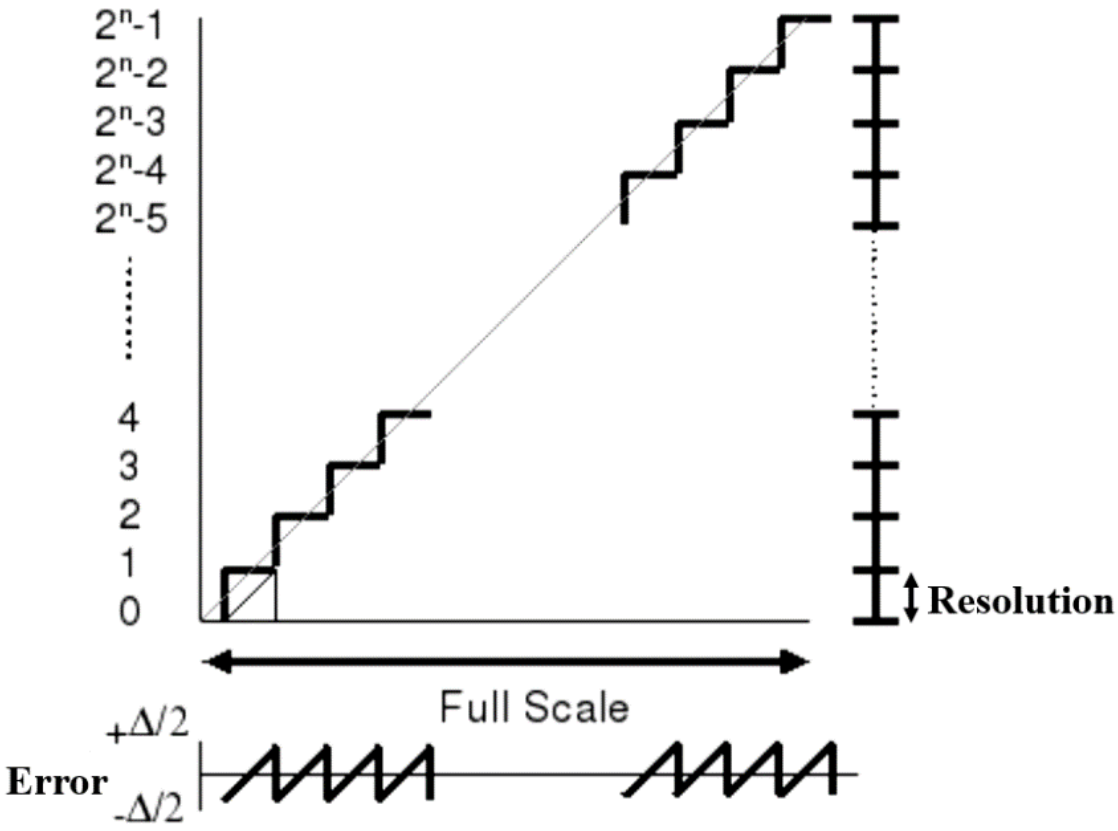

Figure 3.3 Illustration of quantization

Quantization is performed by dividing the full analog input range FSR (Full Scale Range) into 2^n equal parts and comparing them with equally spaced digital values, as shown in Fig. 3.3. AD conversion that quantizes in 2^n equal parts is called AD conversion with n-bit resolution. In ideal AD conversion, the only error is quantization noise. Additionally, the ratio of signal to noise ratio (SNR) is an indicator of the performance of an AD converter [208], [209], [211], [212]. The SNR is 0 dB when the amount of desired signal is equal to the amount of noise. A typical low SNR ADC will have an SNR greater than 0 dB.

3.2.4 Oversampling

In ideal AD conversion, errors and quantization noise are uniformly distributed up to half the sampling frequency $f_s/2$ [213]. If oversampling is performed by setting the sampling frequency to M times the Nyquist frequency $2f_0$, the quantization noise power spectral density will be widely dispersed as shown in Fig. 3.4. Therefore, if the band above f_0 is removed by a filter, the total amount of quantization noise can be reduced. In other words, the SNR is improved. The M in this case is called the oversampling ratio (OSR) [195], [214].

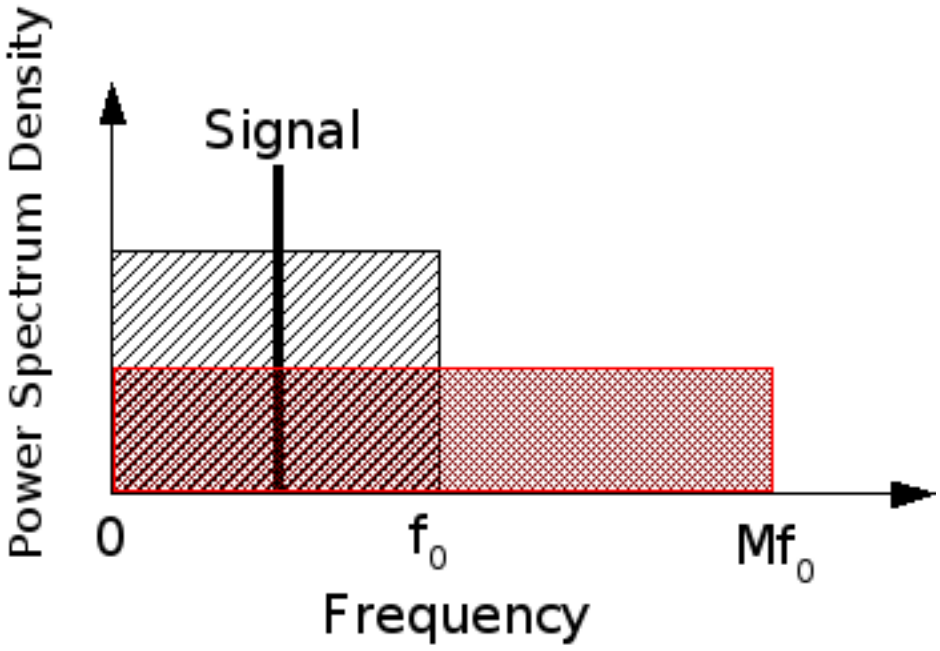

Figure 3.4 Oversampling and quantization noise

Oversampling AD converters require a digital filter at the subsequent stage. The digital filter consists of a low-pass filter and a decimation filter. A low-pass filter removes quantization noise outside the signal band. Next, a decimation filter decimates the data whose sampling frequency $f_s=Mf_N$ due to oversampling to 1/M and down-converts it to the original Nyquist frequency f_N [215–217].

3.3 Delta Sigma Analog-to-digital convertors (DSADC)

3.3.1 Principle of DSADC

The DSADC utilizes two techniques for analog to digital conversion, oversampling, and noise shaping, to achieve a high SNR [216]. A DSADC consists of a delta-sigma modulator (DSM) and a digital filter, as shown in Fig. 3.5. The DSM modulates the input analog signal into a pulse density at a sampling frequency f_s (oversampling) that is sufficiently higher than the Nyquist frequency f_N. At this time, the quantization noise in the low-frequency region is shifted to the high-frequency region (noise shaping). The pulse density sequence obtained by DSM is down-converted to the original Nyquist frequency f_N by a digital filter. This cuts the quantization noise shifted to the high-frequency region and obtains a high SNR.

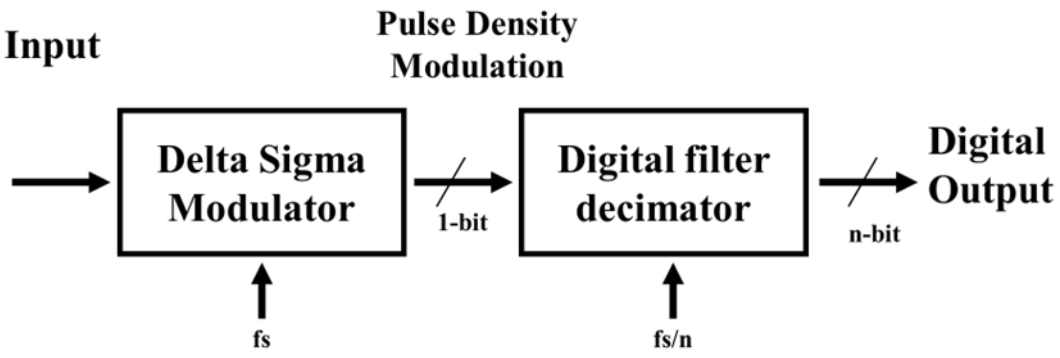

Figure 3.5 Basic configuration of DSADC

Therefore, in a DSADC, the resolution is determined by the sampling frequency and does not require high-precision analog elements. Note that in this configuration, the filter is a normal digital circuit, and the most important part that influences the characteristics is the DSM which is responsible for converting analog signals to digital signals [195], [197], [216].

3.3.2 The basic configuration of DSADC

The DSM, which is the main part of the DSADC[1], consists of an integrator, a 1-bit quantizer, and a 1-bit DAC, as shown in Fig. 3.6 [218]. Here, I concentrate on the first-order DSM.

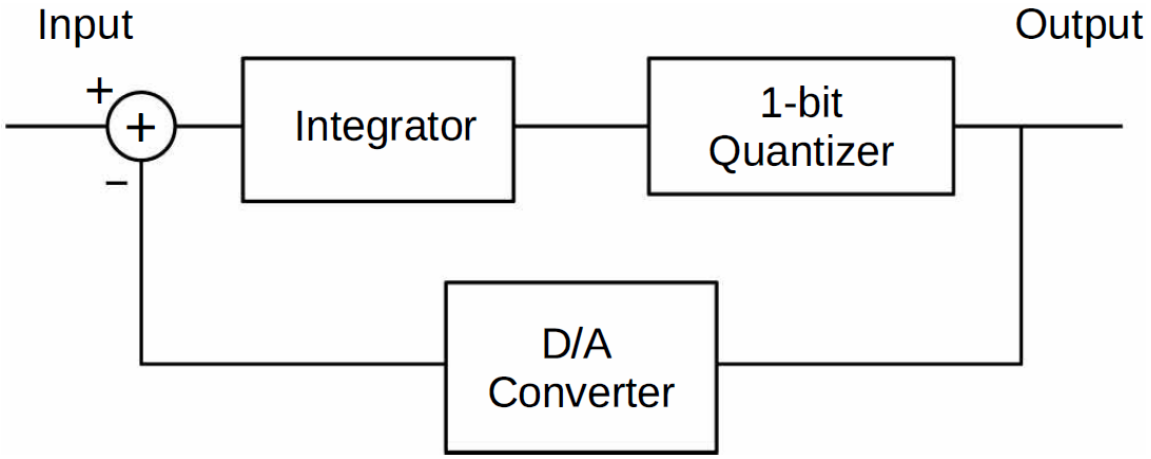

Figure 3.6 Block diagram of the DSM

The input signal is integrated by an integrator, and a pulse is output when the value exceeds a certain threshold. A 1-bit quantizer determines whether the threshold has been exceeded. At the same time, it is fed back through the DAC to prevent the integrator from saturating. This negative feedback is the basic configuration of the DSM, and it performs pulse density conversion of the signal. When the input voltage is large, the integrated output reaches the threshold quickly, so the

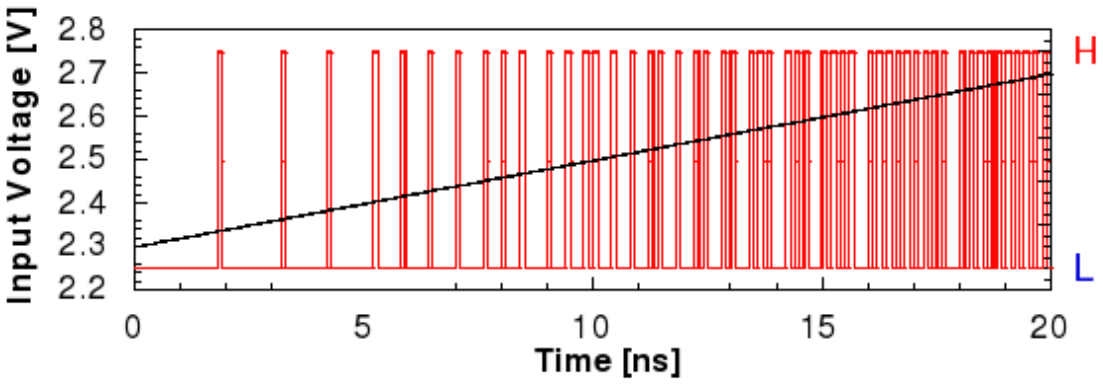

Figure 3.7 Pulse density conversion by DSM

[1] This is a 1st order DSM, although higher-order DSMs are often used.

pulse density becomes dense, and conversely, when the input voltage is small, it becomes sparse as illustrated in Fig. 3.7.

3.4 FDSM and its operating principle

Frequency modulation (FM) is a method of transmitting information by changing the frequency of a carrier wave. In FM, the frequency of the carrier wave is varied up or down depending on the amplitude of the input signal representing information; when the input signal is large, the frequency is high, and when the input signal is small, the frequency is low as shown in Fig. 3.8. This FM signal wave is obtained by adding an input signal to the control voltage of an oscillator whose oscillation frequency can be controlled by a voltage, that is, a voltage-controlled oscillator (VCO: Voltage Controlled Oscillator). If we look at the relationship between the input voltage and the number of edges of the FM signal wave (points where the rise and fall of the wave are steep), we can see that when the input voltage is high, the number of edges is high, and when it is low, the number of edges is low. Therefore, it can be seen that by simply applying FM modulation to the input signal and detecting the zero-crossing point of the FM wave, pulse density conversion of the

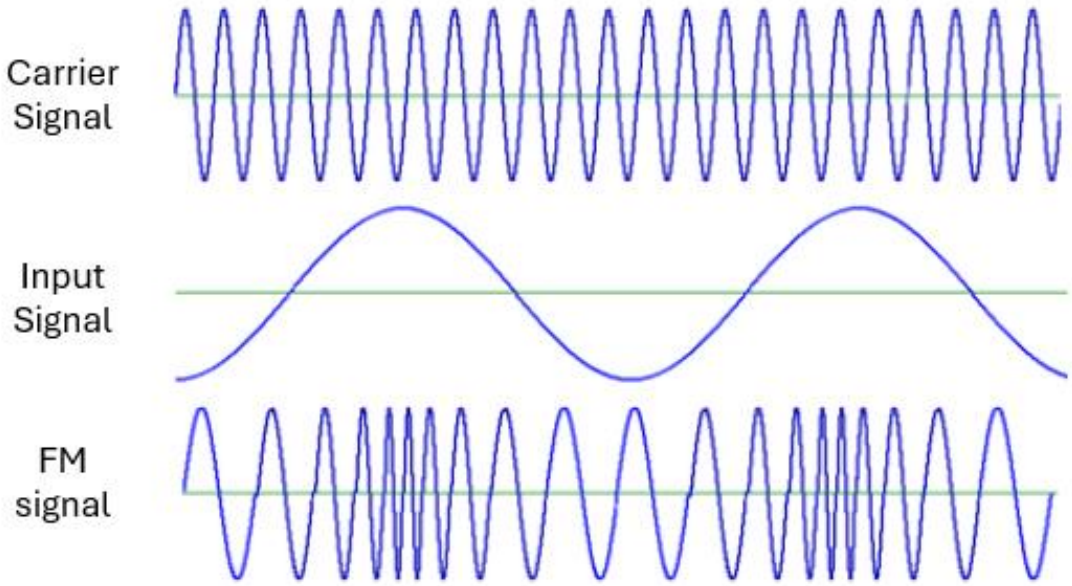

Figure 3.8 Frquency modulation

input signal can be performed in the same way as DSM. This is called FDSM which is a promising AD conversion technique [27], [219], [220].

An FDSM can be composed of a VCO, a 1-bit quantizer, and XOR (exclusive OR) as shown in Fig. 3.9. The FDSM modulator skillfully utilizes the characteristics of the FM signal which is the output signal of the VCO. The phase of the FM signal can be expressed with the following equation:

$$\boldsymbol{\theta(t) = \int_{\tau=0}^{t} 2\pi\left(f_c + kx(\tau)\right) d\tau} \qquad \textbf{(3.1)}$$

Here, $x(\tau)$, f_c, and k represent the input signal, oscillation center frequency (FM signal carrier frequency), and frequency modulation degree, respectively. In this way, the phase of the FM signal can be considered to be the integral of the input signal, and the integrator in the conventional DSM becomes unnecessary. Furthermore, the fact that it returns to 0 when the phase reaches 2π can be considered as virtual feedback. Therefore, by outputting a pulse every time the phase rotates once, it is possible to configure a DSM without a feedback DAC that limits the speed.

The pulse output is obtained by quantizing the FM signal using a 1-bit quantizer and extracting the part that changes from 0 to 1. The circuit in Fig. 3.9 uses a register and XOR to extract not only 0 → 1 but also 1 → 0 changes, which means that a pulse is output every time the phase goes around

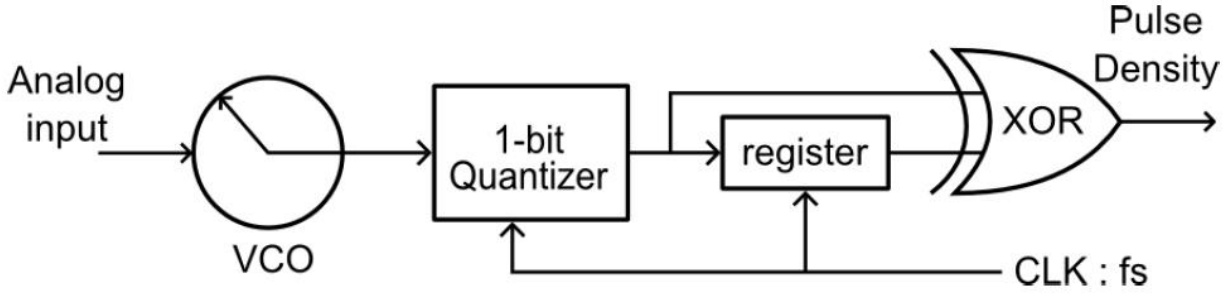

Figure 3.9 Circuit configuration of FDSM

π, effectively doubling the sampling frequency as shown in Fig. 3.10. Therefore, the signal to quantization noise ratio (SQNR) is given by the following equation [221].

$$\boldsymbol{SNQR = 20\log\left(\sqrt{2}\frac{\Delta f}{f_s}\right) - 10\log\left(\frac{\pi^2}{36}\left(\frac{2f_{max}}{f_s}\right)^3\right)} \qquad \textbf{(3.2)}$$

Δf is the maximum frequency deviation given by the maximum input signal range, and f_{max} is the maximum frequency of the input signal.

Thus, this method is suitable for high-speed operation because there is no feedback loop. Furthermore, the feedback is mathematically built-in and does not introduce errors at this stage, making it easy to achieve high accuracy allowing high-frequency operation.

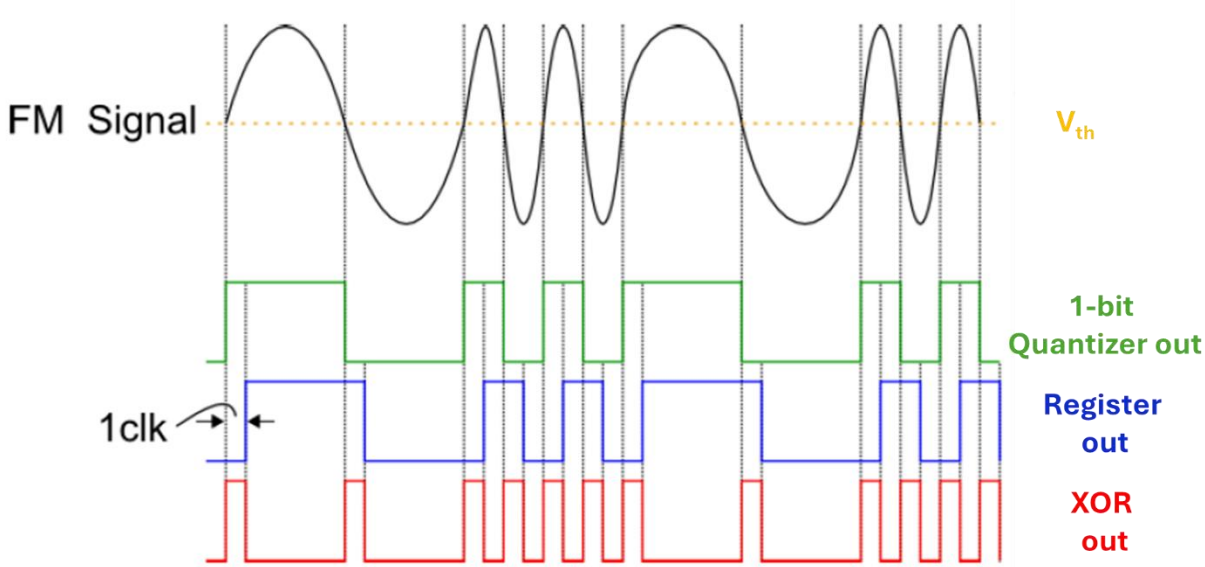

Figure 3.10 FM signal zero cross detection

3.5 FDSM based stylus surface profiler

3.5.1 Introduction

The FDSM can be applied to sensors when the VCO is replaced by an oscillator whose oscillation frequency depends on an external physical parameter to sense. Previously, we proposed some sensors based on the FDSM concept [133], [218], [222–224]. Among these sensors, the

microphone sensor based on a microwave oscillator using a cavity resonator demonstrated a very low noise power of -143 dBFS (decibel fullscale) for 96 kHz band width [218], [223]. This sensor uses a cylindrical cavity resonator for the oscillator, where one end of the resonator is replaced by a thin metal diaphragm that moves in response to sound pressure. In other words, this sensor can be regarded as a displacement sensor of the diaphragm, having a very high dynamic range. Here, we discuss the possibilities of such displacement sensors, and also demonstrate the application of this sensor to a stylus surface profiler. This sensor is very simple, and outputs digital signal directly. Moreover, it is robust against external noises, and eliminates noises added during signal amplification owing to the superior AD conversion technique.

The performance of FDSM sensors is strongly dependent on the frequency modulation width as shown in equation 3.2. This indicates that a higher oscillation frequency is preferable because the modulation ratio remains constant in most cases. The high performance of the stylus surface profiler is discussed in subsequent sections which uses 10 GHz oscillation frequency. However, the performance should be greatly improved by using RTD-based THz oscillators.

3.5.2 The FDSM microphone as a displacement sensor

Figure 3.11 illustrates the FDSM microphone demonstrated in the previous paper [218]. The variable frequency oscillator consists of a cylindrical cavity resonator and a gain block. The one end of the cavity resonator is replaced by a thin metal diaphragm, which moves in response to the sound pressure. The other end is covered by the double-sided FR-4 print circuit board (PCB), where the slots are opened on the copper GND plane to couple the microstrip lines to the cavity resonator. The size of the resonator was 25 mm diameter and 20 mm length. The resonant mode used was TE111, whose resonant frequency is approximately 10 GHz. The resonant frequency of this mode depends on the cavity length, and hence, the diaphragm position. This implementation

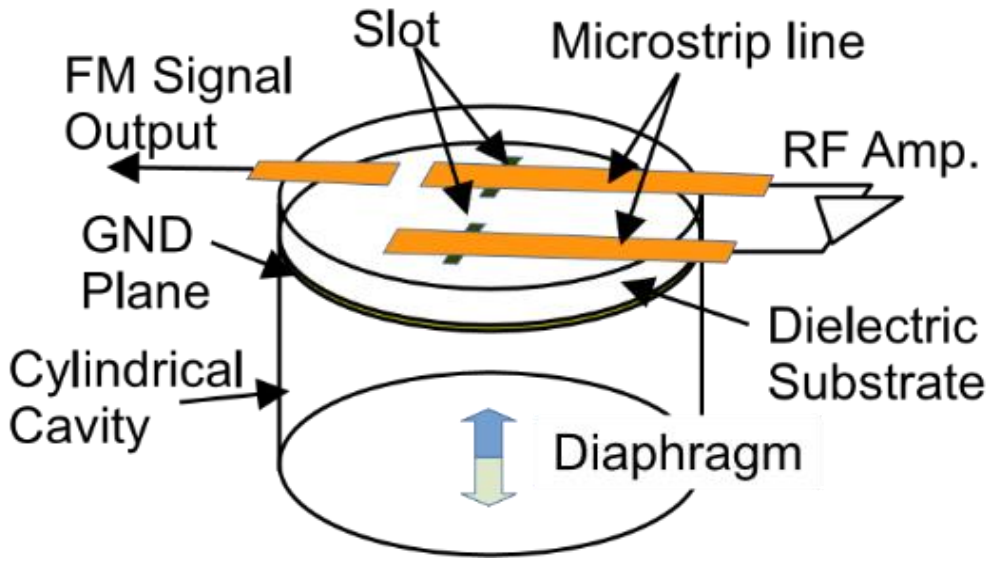

Figure 3.11 Structure of the FDSM microphone sensor employing variable frequency oscillator [218]

is promising because the Q-factor of the resonator is much larger than the LC oscillator using a condenser microphone and an inductor [222]. This large Q-factor results in low phase noise oscillation, which is essential to obtain wide dynamic range [225].

This microphone can be regarded as a displacement sensor for the diaphragm. Here, we will discuss the advantages of the application of the FDSM microphone to displacement sensors, especially to a surface profiler and an atomic force microscopy (AFM).

First, we will discuss the relation of the diaphragm motion to the frequency shift of the cavity resonator oscillator. For the sake of concreteness, the size of the resonator is assumed to be the same as written above in the following explanation. Figure 3.12 shows the resonant frequency shift as a function of the diaphragm displacement calculated by electromagnetic (EM) simulation. The diaphragm is assumed to be paraboloidal under sound pressure [226]. The figure shows that the

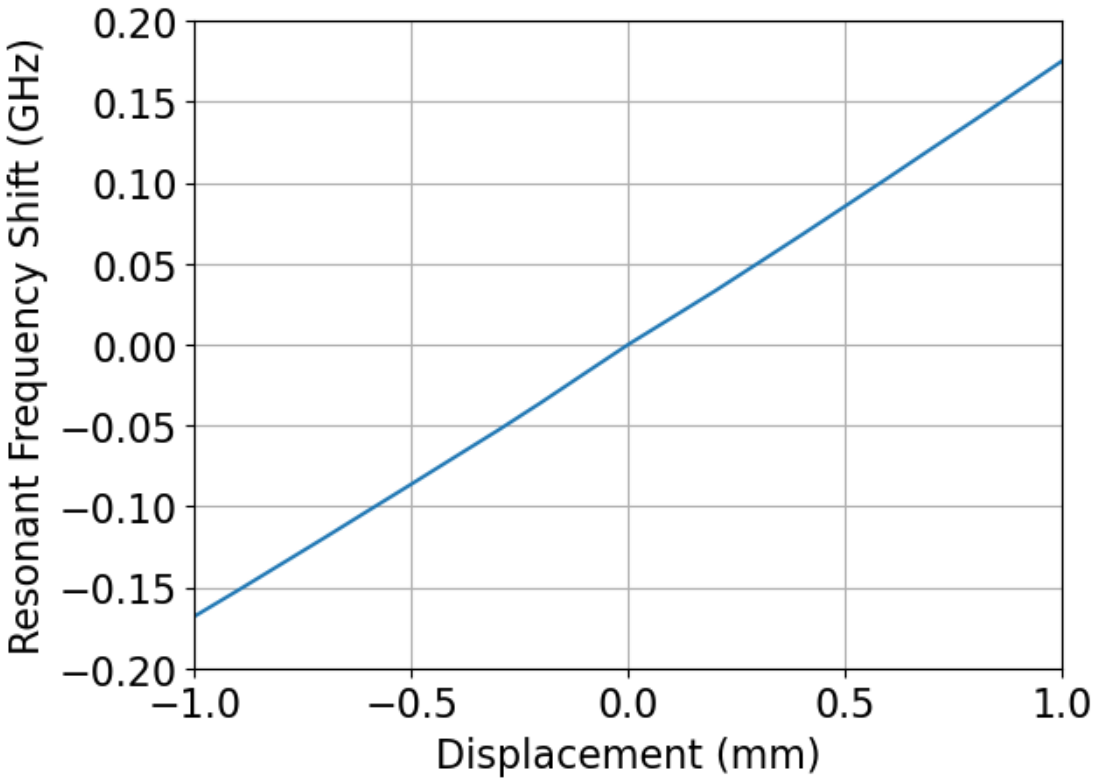

Figure 3.12 Resonant frequency of the cylindrical cavity resonator calculated by EM simulation as a function of the diaphragm displacement. The diaphragm is assumed to be paraboloidal, and the displacement is measured at the center of the diaphragm.

resonant frequency shift is approximately proportional to the displacement, and the linearity is good for within ±1 mm displacement.

A significant implication in this figure is that this sensor can measure the displacement with a very wide dynamic range. An extremely low total noise power of -143 dBFS was demonstrated with a sampling rate of approximately 12.6 GHz [218]. This indicates that this sensor can measure the frequency shift as small as 22 Hz. The corresponding minimum observable displacement is approximately 0.1 nm. If we assume the maximum observable displacement to be 1 mm to assure linearity, the corresponding frequency shift, 190 MHz, is still much less than maximum observable frequency shift of 3.15 GHz, which is a quarter of the sampling rate. In conclusion, ultra-wide dynamic range of 0.1 nm to more than 1 mm can be obtained with this displacement sensor.

3.5.3 Application of the FDSM microphone sensor to a Stylus Surface profiler and an AFM

Here, we propose and discuss application of the FDSM microphone sensor to a stylus surface profiler, and even to an atomic force microscope (AFM). Figure 3.13 shows the schematic of the FDSM stylus surface profiler. A stylus probe is set on the center of the diaphragm, and it is contacted to the sample, which moves with a piezoelectric stage. The most important advantage of this stylus profiler is its wide dynamic range as discussed in the previous section. It can measure the surface profile in the range from 0.1 nm to more than 1 mm without changing the amplifier gain. This permits us to observe 0.1 nm class structure on a surface having 1-mm class large roughness. This technique can also be applied to AFMs when the stylus probe is replaced by an AFM tip with sophisticated diaphragm and tip design having superior mechanical properties. Important features of this type of stylus surface profilers/AFMs are follows.

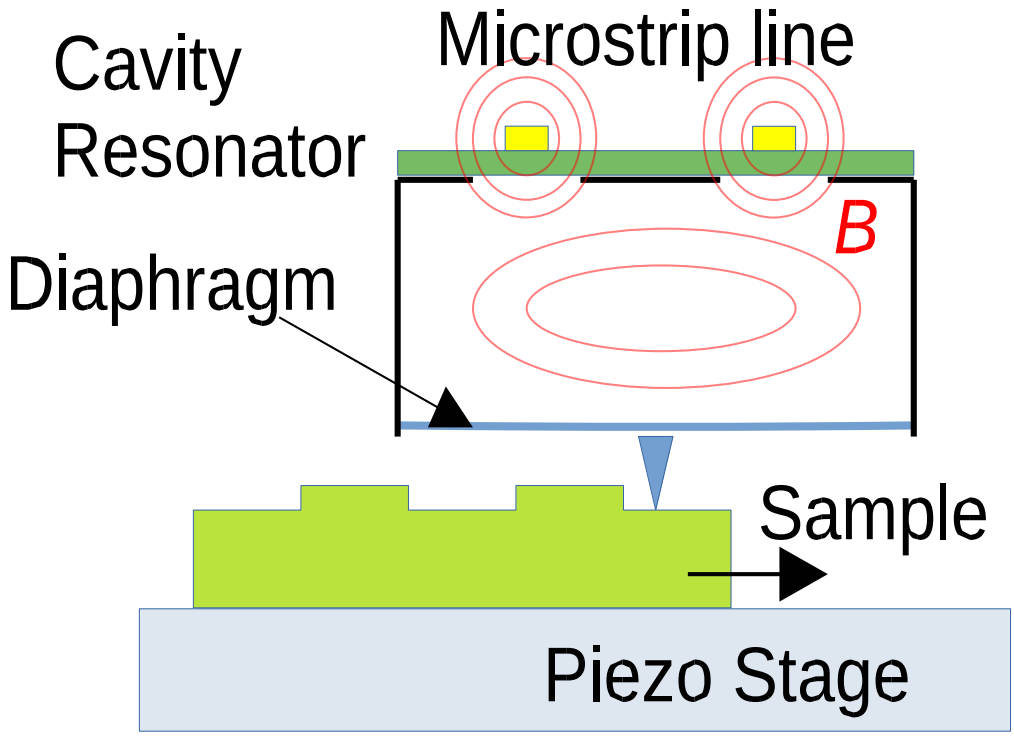

Figure 3.13 A basic structure of the FDSM stylus surface profiler.

First, it has a wide dynamic range with a wide bandwidth. This permits us high speed scanning as well as ultra small structure measurement on a rough surface. Second, oscillating-mode, and tapping-mode measurements are also possible when applying sound waves to the diaphragm. A most important advantage of this is that the whole oscillating waveform can be precisely measured, which should include details of the atomic force. This is in contrast to the conventional AFMs, which measure the oscillating frequency shift of the cantilever. It should be noted that the oscillating frequency can be freely changed by changing the applying sound frequency, which is advantageous for measuring mechanical properties, such as elasticity, viscosity, and friction. This is difficult for the conventional AFMs that use the resonant frequency of the cantilever.

3.5.4 Prototype Device of the FDSM Stylus Surface Profiler

We have fabricated a simple prototype device of the stylus surface profiler to demonstrate the basic function. Figure 3.14 shows the photograph of the fabricated device. It consists of microstages, a piezoelectric stage, and a cavity resonator oscillator in a stainless frame.

Figure 3.15 shows the photographs of the fabricated cavity resonator oscillator. It was fabricated from oxygen-free, high conductivity copper to achieve a high Q-factor, which is essential for noise floor reduction. The copper block size was $45 \times 45 \times 20$ mm^3, and the cavity diameter and length were 25 mm and 20 mm, respectively. The cavity surface was polished and cleaned with a chemical cleaner to achieve a high Q-factor. The oscillator circuit on the FR-4 board is shown in Fig. 3.15 (b), where the transmission-type oscillator topology was used to improve the phase-noise property.

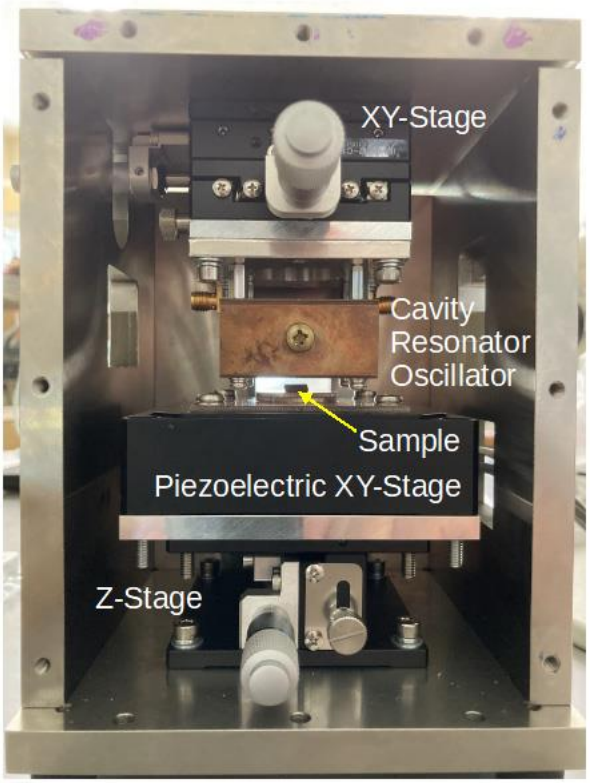

Figure 3.14 Fabricated FDSM stylus surface profiler.

We used a GaAs pHEMT MMIC medium power amplifier, HMC441LP3E (Analog Devices), as the gain block of the oscillator.

For ease of fabrication, we used a microprobe pin for the stylus probe tip. The pin was cut to a length of about 2 mm and glued to a support stand that was placed on the thin plastic plate with a diameter of 1 cm. This plastic plate was bonded to the center of the diaphragm as shown in Fig. 3.15 (c). The diaphragm was made of commercially available 12-μm thick Al foil, the outside of which was covered with adhesive tape to suppress oscillation due to noise. The tip apex was about 10 μm in diameter.

In this experiment, no tension was intentionally applied to the diaphragm. Therefore, the force exerted by the tip on the sample can be approximately estimated from the mass of the tip support stand. The support stand was made of copper plate with a thickness of 0.1 mm. It is therefore

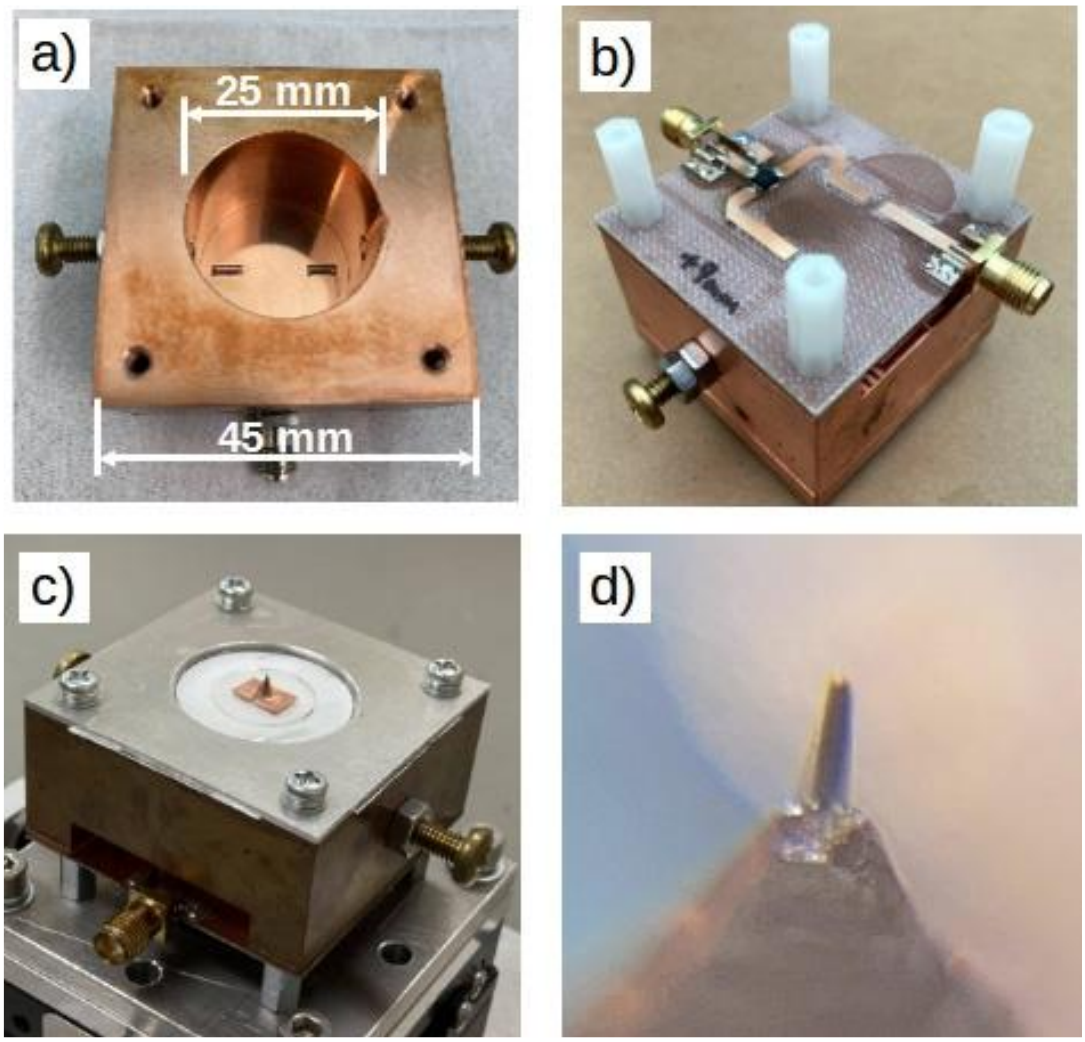

Figure 3.15 Photographs of the fabricated cavity resonator oscillator. (a) Inside of the cavity resonator. The slots were shown on the bottom. (b) PCB-side of the resonator oscillator. (c) Diaphragm with a tip and support stand. (d) Apex of the tip. The apex size was approximately 10 μm.

estimated to be about 0.3 mN. This is comparable to the conventional stylus profiler. No scratch was seen on the sample surface after the measurement.

The cavity resonator was attached on the xy-microstage for rough positioning of the measuring point, and it was set to the ceiling board downward. The piezoelectric stage was set on top of the z-microstage to adjust the sample height. The piezoelectric stage used was THK PRECISION, PS2L90-400U-S, which can control the sample's xy-position in the range of ±200 μm with a 20 nm resolution.

3.5.5 Experimental Results

We tested the basic operation of the prototype device with a GaAs sample having various depth trenches. The sample has 60-μm width trenches separated by 40-μm spaces in a line-and-space pattern. The trenches were fabricated by photolithography and wet chemical etching using sulfuric acid-based etchant. The nominal depth of the trenches are 10 nm, 100 nm, 1 μm, and 10 μm, respectively. Due to the side-etching effect, the 10-μm depth trench has much wider width than that of the mask pattern. The sample was set on the PCB-based sample holder using electron wax. The sampling and digital process was done using a circuit programmed on a field programmable gate array (FPGA) board described in the reference [218].

Figure 3.16 shows an example of the surface profile of the sample measured by the prototype device. The depth was measured at each 4-μm step controlled by the external bias voltage applied to the piezoelectric stage. This step was smaller than the tip apex and the total number of measurement points was 100. Figure 3.16 was obtained from a single scan. A linear leveling procedure to compensate the sample tilting was carried out for specified two points after the scan. The displacement-to-frequency conversion factor was calibrated with values measured using a commercial surface profiler, and determined to be 150 kHz/μm. This factor reasonably agreed with the value determined from Fig. 3.12, 180 kHz/μm. The difference should be resulted from the difference in the diaphragm form due to the thin plastic plate. In Fig. 3.16 (a), a 1 μm depth trench is clearly seen with a large 10 μm depth trench. Moreover, a 100 nm depth trench is also visible at the left of the 10 μm trench. Fig. 3.16 (b) shows the magnified view of Fig. 3.16 (a), where the x-axis is the same as that of Fig. 6 (a). Here, the 10 nm trench is also seen at the right of the 10 μm

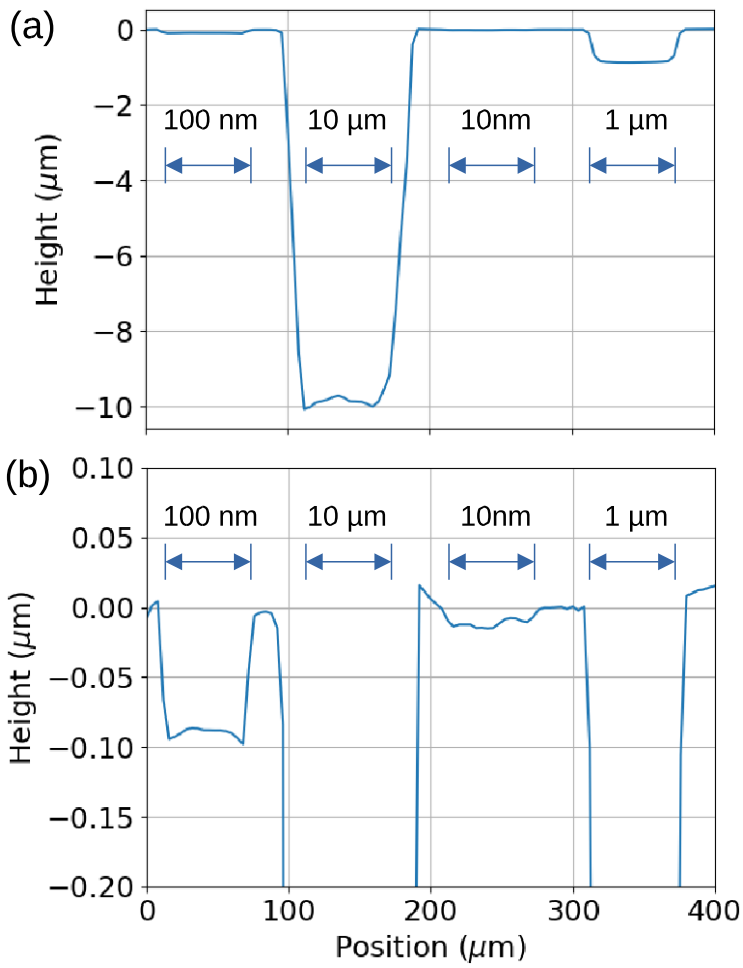

Figure 3.16 An example of the measured surface profile of the GaAs line-and-space sample. The lower Fig. 3.16 (b) is a magnified view of the upper Fig. 3.16 (a). The areas designated with an arrow are trenches with a nominal depth shown near the arrow.

trench. It should be noted that this large dynamic range profile can be obtained in a single scan with no gain change.

Finally, we obtained a surface morphology map by scanning the sample with x and y axis. An example of the results is shown in Fig. 3.17. Figure 3.17 (a) shows the original map measured. Here, only 10-μm and 1-μm trenches are visible. Figure 3.17 (b) is a magnified view of Fig. 3.17 (a), where the z-axis was enlarged to observe shallower structures. In this figure, the linear leveling

procedure was carried out based on a plane designated by 3 points. The 100 nm trench is clearly seen at the left side of the 10 µm trench. Moreover, the 10 nm trench is also seen at the right side of the 10 µm trench. The width of the 10 µm trench is wider in Fig. 3.17 (b), this is probably

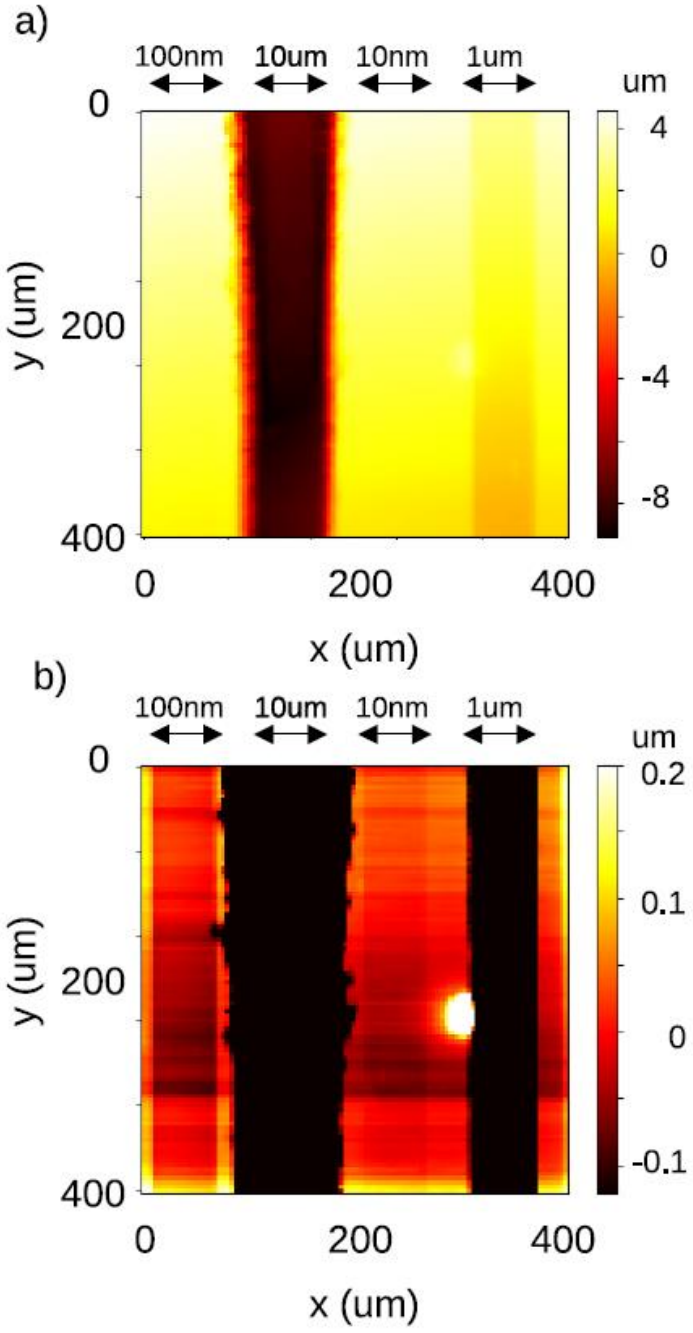

Figure 3.17 An example of the 2-dimensional surface height map of the line-and- space sample. Figure 3.17 (a) shows an overall view, while Fig. 3.17 (b) shows the magnified view. The areas designated with an arrow are trenches with a nominal depth shown near the arrow.

resulted from the effect of the tip apex radius. In summary, this scanned data contains information of the morphology in the range from less than 10 nm to 10 μm, which can be obtained with no gain control.

Table 3.1 summarizes the results in comparison to conventional stylus surface profilers. It should be noted that the device fabricated in this experiment is a simple, prototype device to demonstrate basic operation. Nevertheless, the performance of the device is already comparable to conventional ones. Much higher performance is expected with more sophisticated diaphragm and circuit design.

Table 3.1 Comparison to the conventinoal stylus profilers

	Conventional Stylus profiler	Our proposal	
		Expected	This work
Sensor type	LVDT*1	FDSM	
Resolution	~ 1 nm	$\lesssim$ 0.1 nm	~ 1 nm
Max depth	~ 1 mm	$\gtrsim$ 1 mm	10 μm
Dynamic range	$\lesssim$ 90 dB*2	$\gtrsim$ 120 dB	~ 80 dB

*1Linear Variable Differential Transformer
*2Nominal value calculated from the range/resolution

3.5.6 Conclusion

A novel type of displacement sensor was proposed based on the FDSM. A cylindrical cavity resonator with a diaphragm at one end of the cavity was used for the variable frequency oscillator, which is a core of the FDSM. This can be applied to a stylus surface profiler and an AFM, when a probe tip is set at the diaphragm. To demonstrate basic operation, we fabricated a stylus surface profiler. A good surface profile was successfully obtained with this device. A 10 nm depth trench was measured together with a 10 μm trench in a single scan without gain control. This result clearly demonstrates the extremely wide dynamic range of the FDSM displacement sensor. Additionally,

it depicted that the performance of FDSM sensors strongly depends on the frequency modulation width. It implies that the higher oscillation frequency is preferable since the modulation ratio remains constant in most cases. So, the high-performance unprecedented sensors can be realized by using RTD based THz oscillators by simply replacing VCO in FDSM.

Chapter 4 Application of RTD oscillators to FDSM

4.1 Introduction

As discussed in Chapter 1, most of the research on RTD oscillators is primarily focused on radio communication applications [227–230]. Since the THz band has a distinctive absorption spectrum and non-invasive effects, sensor applications in the fields of medicine, chemistry, biology, physics, and material science are also promising [51], [231–233]. Sensors that use RTD oscillators to detect frequency changes due to external parameters have already been proposed and demonstrated [133], [224]. These sensors use the FDSM technique for AD conversion by replacing the VCO with RTD oscillators. The results of the FDSM-based stylus profiler discussed in Section 3.5 clearly demonstrate the extremely wide dynamic range as well as the performance of FDSM sensors, which depends on the frequency modulation width. In general, the ratio of changes of frequency modulation and sensing parameters is constant, increasing the oscillation frequency is beneficial. In addition, using higher frequency oscillators has several advantages, including wide frequency bandwidth and small area [224]. Therefore, the application of RTD oscillators to these sensors will be the basis for unprecedented sensors in the THz region featuring high dynamic range and high-speed operation.

In this chapter, by taking advantage of the FDSM superior AD conversion technique and RTD high-frequency operation, scanning near field terahertz microscope (SNFTM) is proposed. The proposed method includes two ways for down-converting the THz signals aiming to make them suitable for sampling. The down-conversion method can be achieved with either symmetric type monostable bistable logic element (SMOBILE) or RTD mixer. Then the nonlinear effects of the transmission line are investigated that pose a hinderance in the correct operation of the sensor.

Finally, owing to the ease of measurements, the operation of the proposed SNFTM is verified in the microwave frequency range that can be said scanning near field microwave microscope (SNMM).

4.2 Proposal of the SNFTM based on an RTD oscillator

The THz absorption characteristics and noninvasive properties have become the basis for exploring the field of THz imaging [5]. Especially, THz near-field imaging has been reported with various scanning techniques aiming to provide high-resolution imaging beyond the diffraction limits. The Near field THz imaging allows material characterization, biological imaging, and studying nanoscale structures [234–236].

The motivation of the current proposed SNFTM is based on the concept of a self-oscillating evanescent microwave probe (SO-EMP) which is designed for very high spatial resolution imaging of material nonuniformities [237]. It consists of a microstrip line resonator along with an amplifier connected to the feedback loop as illustrated in Fig. 4.1. This microwave oscillator probe is equipped with a wire tip at one end of the resonator. When the probe moves closer to the sample,

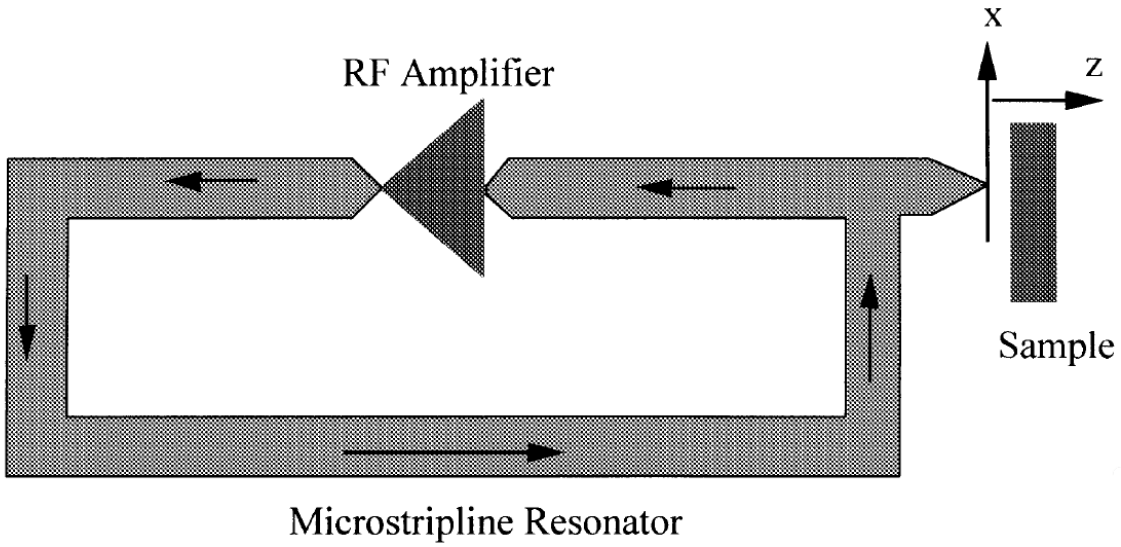

Figure 4.1 Schematic diagram of a self-oscillating evanescent microwave probe with a built-in RF amplifier. (Adopted from [237] *)*

capacitance is formed between the sample and the probe tip (serves as an electric dipole) resulting in the change of frequency and quality factor of oscillator. It permits frequency tracking as well as quality factor mapping, providing insight into the electronic properties of the materials, such as dielectric constants, carrier concentrations, and doping.

Based on above mentioned concept, the SNFTM is proposed aiming to characterize the electronic properties of the materials employing THz waves. Employing THz oscillators can provide subwavelength resolution allowing us to explore the nanoworld precisely. The SNFTM circuit is composed of an RTD and LC resonator equipped with a probe tip connected to the resonator side. The basic circuit configuration is illustrated in Fig. 4.2. When the probe tip moves closer to the sample, it forms a capacitance C_{tip} due to the interaction between the evanescent field near the tip and the free electrons that come to the surface of the sample. This capacitance is subject to change

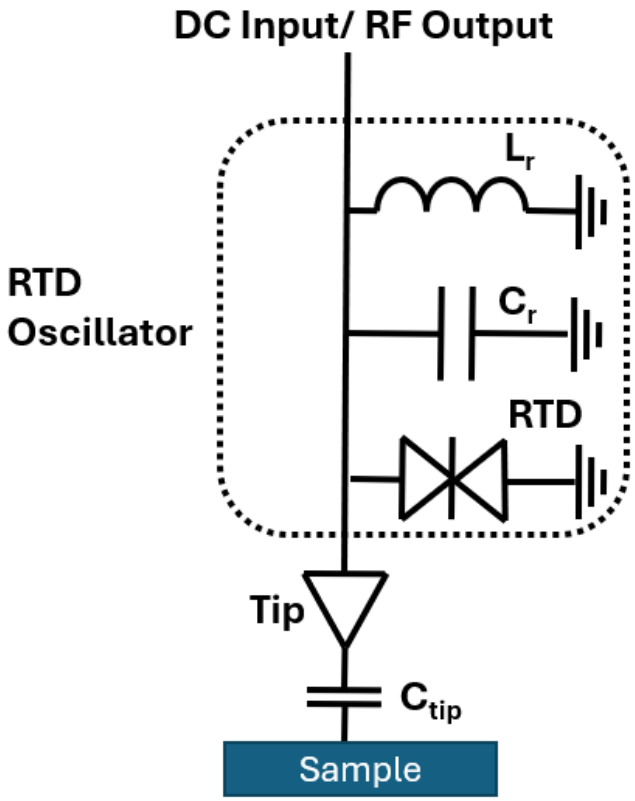

Figure 4.2 Basic circuit configuration of SNFTM

with the dielectric properties, doping, carrier concentration, and material composition of the sample. If the sample, permittivity of dielectric, and tip geometry remain the same, the capacitance is determined by the tip-sample distance which can be expressed using the following formula:

$$C = \frac{\epsilon_0 A}{d} \qquad 4.1$$

Where ϵ_0 is the permittivity of dielectric which is air in our case. A is the overlap area between the tip and sample in square meters, and d is the distance between the tip and sample. When the tip-sample distance decreases, the capacitance increases and vice versa. This capacitance affects the LC resonator capacitance value. Hence, a rough approximation of the frequency of the RTD oscillator can be achieved from the LC resonator value by ignoring the impedance of the tip and wires from the below equation:

$$f = \frac{1}{2\pi\sqrt{LC}} \qquad 4.2$$

From the above equation, the resonant frequency decreases as the capacitance C increases. Subsequently, it is concluded that reducing the tip-sample distance results in increasing the capacitance which in turn decreases the oscillation frequency. Thus, the RTD oscillator becomes a variable frequency oscillator which is an ideal substitute for the VCO in the FDSM technique for high-resolution AD conversion. The mapping of frequency tracking becomes the basis for imaging.

Here, it is important to note that the RTD oscillator works in the THz frequency region and the direct AD conversion of high-frequency signals is challenging. Considering this problem, two methods are proposed in order to make the SNFTM suitable for AD conversion employing the FDSM technique. One is to use the symmetric-type monostable-bistable transition logic element (SMOBILE) for direct under-sampling of THz signals. The second is to use the RTD mixer for

down-conversion of the THz signals and then applying to FDSM. Both methods are elaborated in subsequent sections.

4.3 SNFTM employing SMOBILE

The complete setup of SNFTM is depicted in Fig. 4.3. It consists of the SNFTM circuit, SMOBILE, and FDSM. The working flow of SNFTM setup is that first the high frequency modulated signal is transferred to the SMOBILE which undersampled the signal. Then this signal passes to the FDSM for AD conversion. Ultimately, the change in frequency is mapped to form the image of the sample. Here the purpose of SMOBILE is discussed.

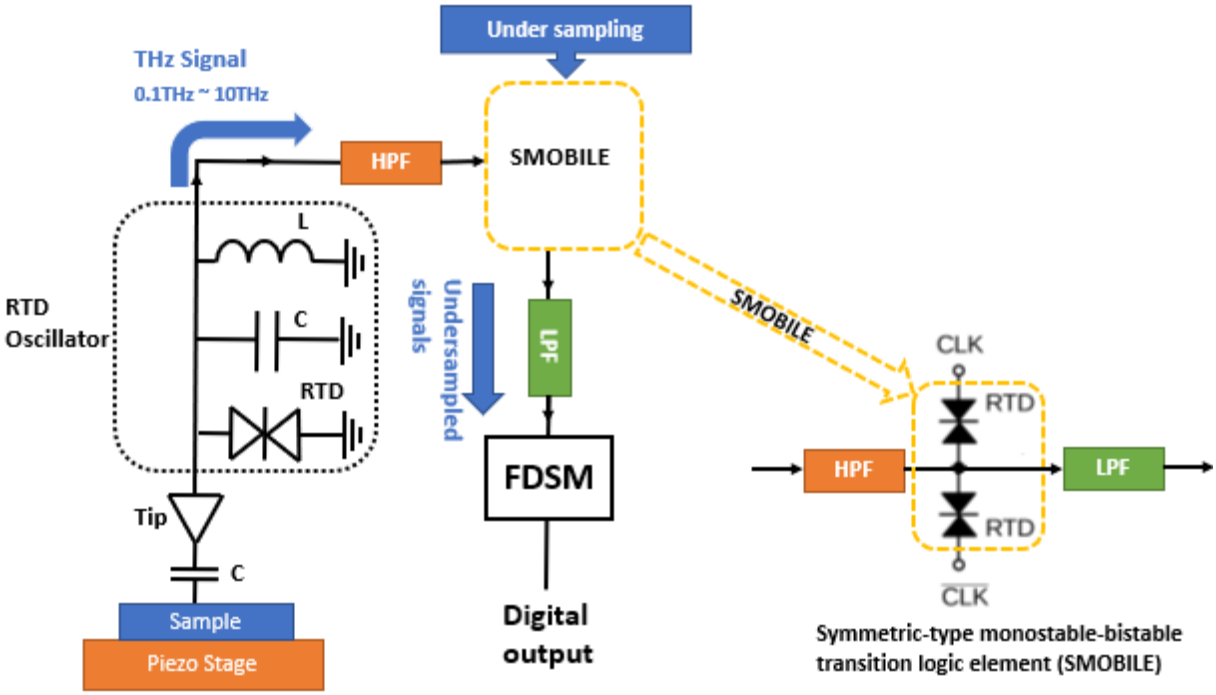

Figure 4.3 Proposed complete setup of the SNFTM

SMOBILE is proposed by incorporating the RTDs for direct under-sampling of THz signals. So far, the working of RTD has been discussed for oscillator circuits. Besides oscillators, RTDs can be used for various applications such as mixers, logic elements, etc [238], [239]. Here, the applications of RTDs are studied to a 1-bit quantizer for THz-signal under-sampling. This circuit

is advantageous for direct sampling of the THz frequency range due to its high sensitivity and is highly suitable for THz-range FDSM sensors [240], [241].

Here, a symmetric-type monostable-bistable transition logic element (MOBILE) [242] is employed for a high-speed 1-bit quantizer. The MOBILE works as a DFF or 1-bit quantizer owing to the monostable bistable transition of the series-connected RTD circuit caused by the bias voltage change. The important difference between the SMOBILE from the conventional MOBILE [243] is that the complementary clock signals are fed to the RTDs, as shown in Fig. 4.4. This clocking scheme solves the problem of the conventional MOBILE that the output current interferes with the proper operation, especially, when the effect of the load capacitance cannot be ignored [244]. Moreover, this circuit does not use an input HEMT which restricts the maximum input frequency. In addition, a new input/output isolation technique is used based on the frequency difference. A band pass filter (BPF) and an LPF are added at the input and output ports, respectively. These filters can isolate input/output signals when the circuit is used for under-sampling.

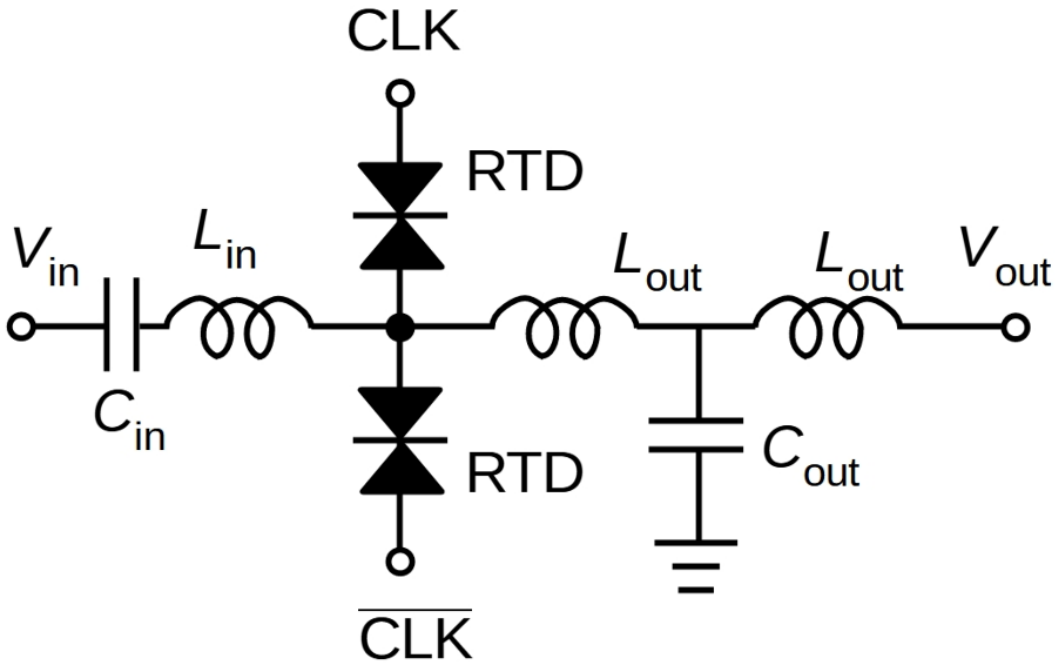

Figure 4.4 Circuit diagram of the SMOBILE with HPF/BPF and LPF I/O isolation.

4.3.1 SMOBILE simulation

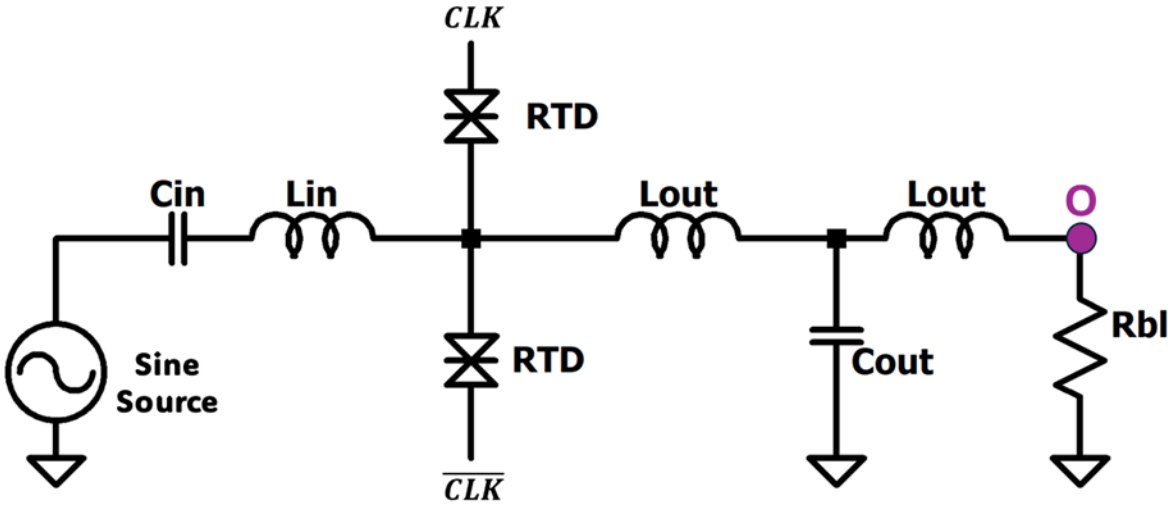

Figure 4.5 SMOBILE circuit used for simulation

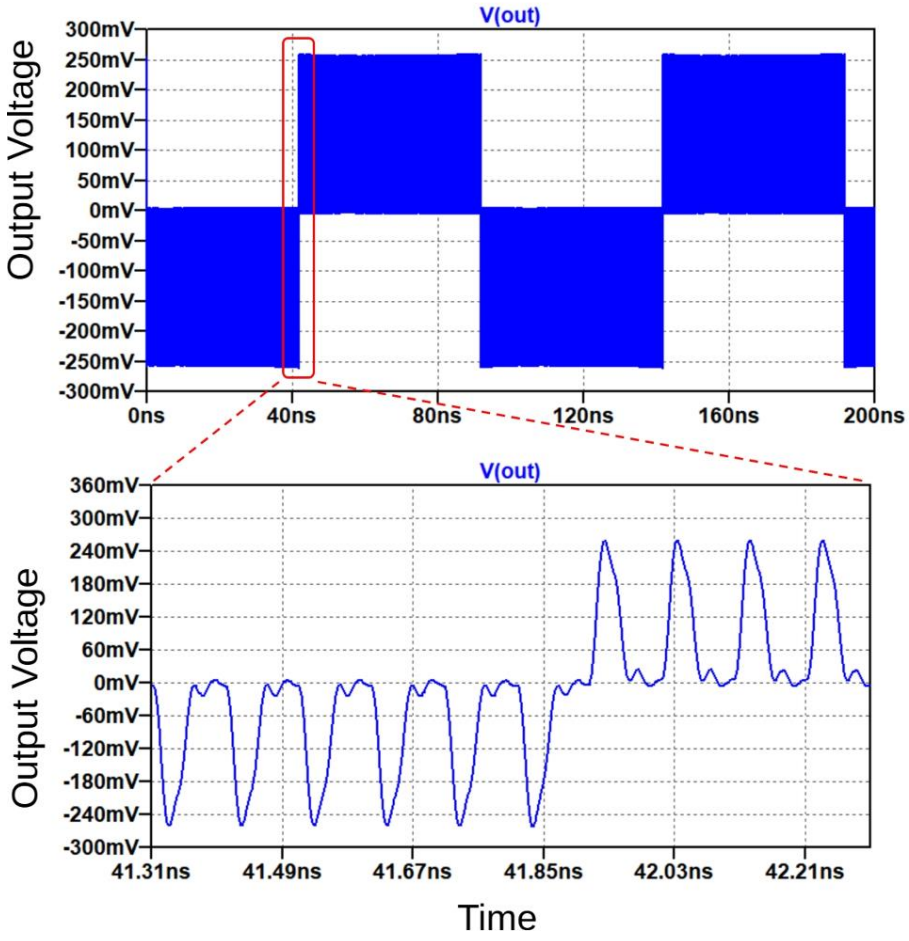

Figure 4.6 An example of the simulation results. The input signal frequency is 500.1 GHz, and the clock frequency is 10 GHz. Lower figure shows the magnified view near the Low to High transition.

First, I carried out a circuit simulation with the same RTD model that is discussed in section 2.3.2. Figure 4.5 shows the SMOBILE circuit that was designed for simulation. Here, the 500.1 GHz input signal is supplied from a sinusoidal source (Sine source) and 10 GHz complementary clock (CLK and $\overline{CLK}$). On the input side, C_{in} followed by L_{in} works as a BPF to provide isolation from the output low-frequency signal. On the output side, L_{out} and C_{out} constitute the LPF aiming to get under-sampled signal at the output. Here, R_{bl} works as a broadband load (50 Ω) equivalent to the impedance value of measurement devices used for the experiment. The circuit parameters are shown in Table 4.1. Figure 4.6 shows an example of the simulation results measured at the O node. The upper figure shows the output waveform at the 50-Ω load. As the input frequency is slightly different from the integer multiple of the clock frequency, the input signal phase at the rising edge

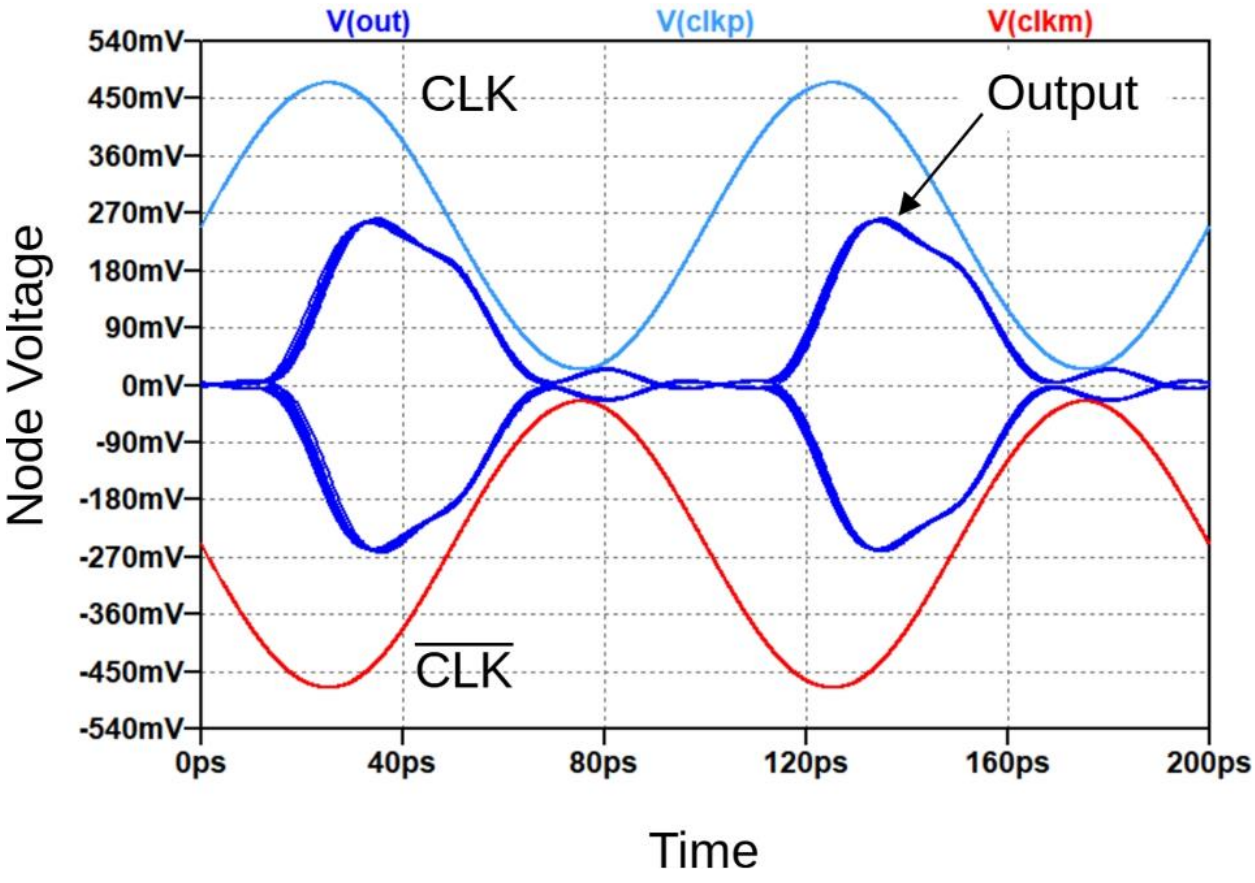

Figure 4.7 The simulated eye-pattern diagram of the SMOBILE. The input and clock frequencies are the same as those in Fig. 4.4

of the clock changes slowly (0.2 % per clock period). As a result, the output signal repeats 1 and 0 with a period of 100 ns. The lower figure shows the magnified view of the output voltage near the transition. The eye-diagram of the output is shown in Fig. 4.7 together with the clock voltages. Like the conventional MOBILE, the output shows the return-to-zero (RZ) signal pattern. Good eye opening can be obtained indicating a large phase margin. This is owing to the monostable-bistable transition as well as the high-speed nature of the RTD.

Parameters	Values
C_{in}	20 fF
L_{in}	20 pH
L_{out}	0.4 pH
C_{out}	0.1 pF
R_{bl}	50 Ω
RTD peak current	10 mA
RTD capacitance	20 fF

Table 4.1 Element values of the fabricated circuit

4.3.2 SMOBILE circuit fabrication

In order to verify the simulation results, simple circuits were fabricated using InGaAs-based RTDs on a 0.8 mm thick printed circuit board (PCB) to demonstrate the basic operation as shown in Fig. 4.8. The RTD pairs and pads were fabricated on the wafer and cut into 2.5x2.5 mm^2 chip, and they were connected using wire bonding. To eliminate the effects of bonding wires and for ease of measurement, relatively low input and clock frequencies, approximately 1/100 of those in the above simulation, were chosen to design. A microstrip line discontinuity is introduced which works as a high pass filter. For LPF 1005-type chip elements were used for the capacitors and inductors. The value of inductors was chosen 4 nH and a 1 pF capacitor was used.

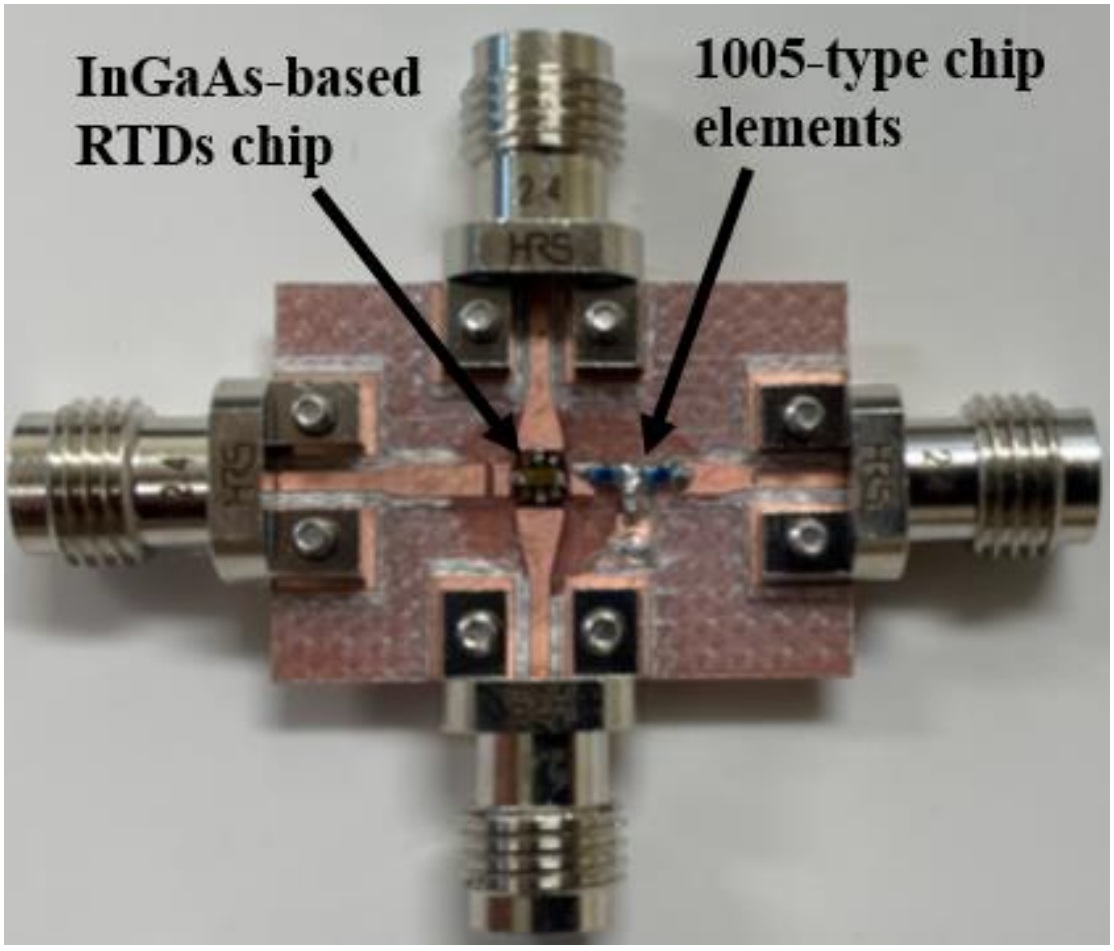

Figure 4.8 SMOBILE circuit fabricated on PCB substrate.

4.3.3 Experimental setup and results

Figure 4.9 illustrates the experimental measurement setup for verification of the basic operation of the fabricated circuit. The pulse pattern generator (PPG) is used to supply the clock signal. The

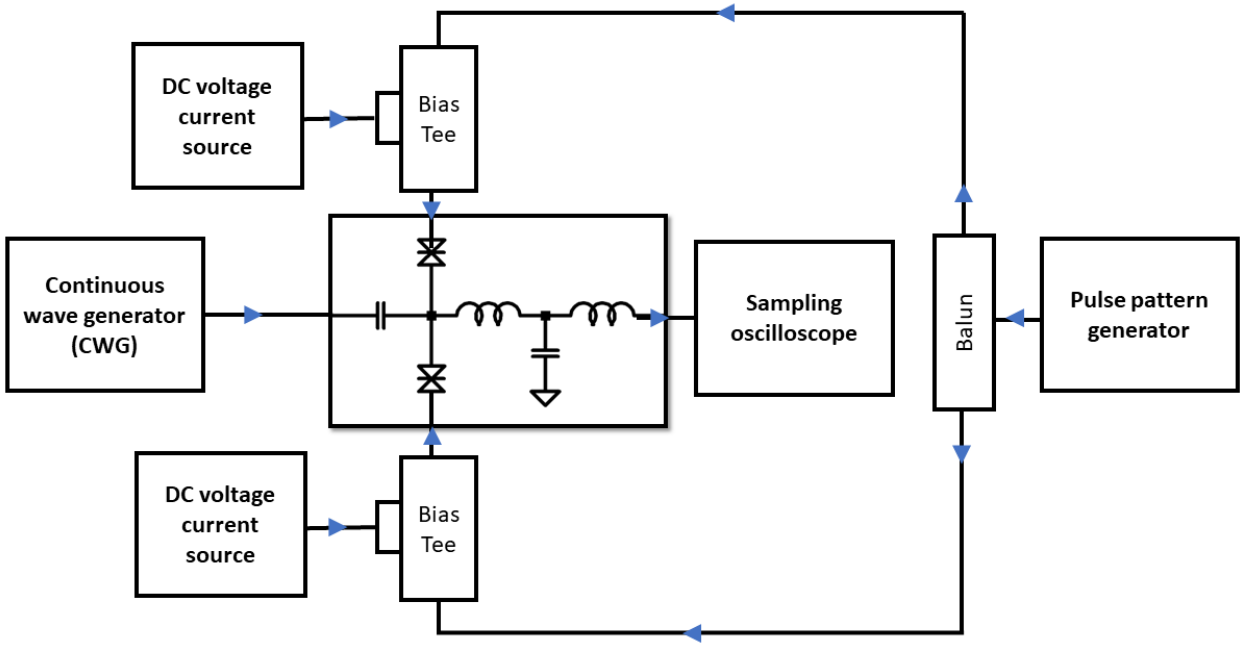

Figure 4.9 Experimental measurement setup for SMOBILE circuit

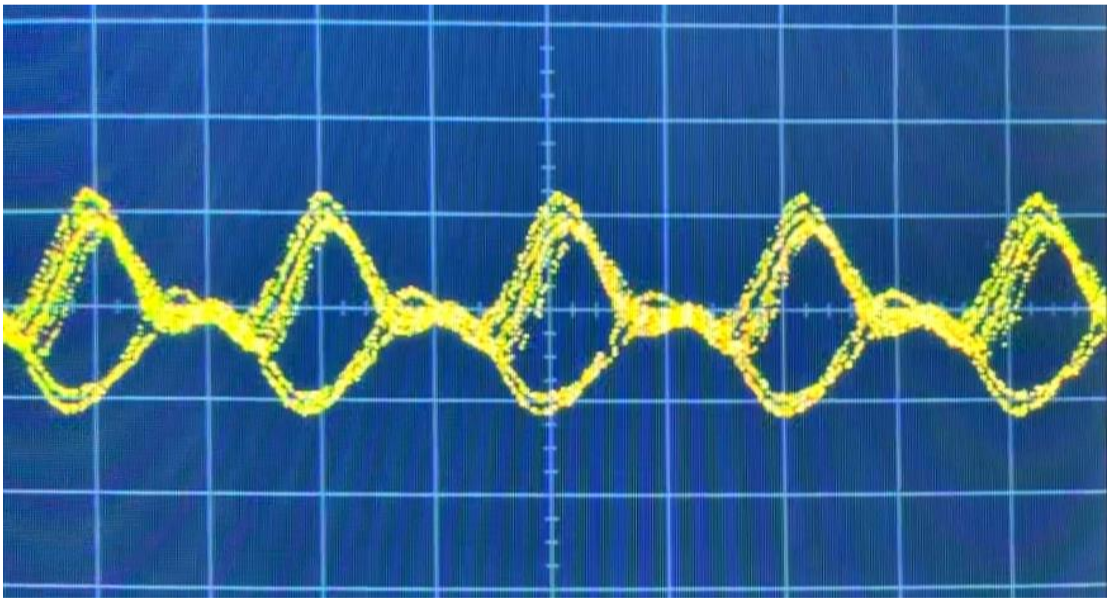

Figure 4.10 An example of the output wave form from the prototype circuit fabricated on a PCB substrate with an InGaAs-based RTDs. (Horizontal axis 300 ps/div, Vertical axis 50 mV/div.) The input and clock frequencies are 4.35 and 1.6 GHz, respectively.

complementary clock pulses were generated using a balun. The signal generated by PPG does not have enough driving current for RTDs. So, the complementary clock is fed to the circuit in conjunction with DC voltages. In order to avoid any instability in the circuit, both DC voltage current sources are grounded, ensuring that their potential is at the same point. The input RF signal is provided using the continuous wave generator. Figure 4.10 shows an example of the output waveform with an input frequency of 4.35 GHz and a clock frequency of 1.6 GHz. A clear eye-pattern was observed. It should be noted that the circuit includes no buffer amplifier, and the SMOBIE directly drives the 50-Ω load. This was impossible for conventional MOBILE, because the load current interferes with the switching to "High" voltage.

This method is proved to be a very precise and novel way of under-sampling the high-frequency signals. However, one difficulty of using SMOBILE is that both RTDs should have the same value of peak current for the proper operation which is strenuous to achieve in experiments.

4.4 SNFTM employing the RTD self-oscillating mixer (SOM)

The setup of SNFTM incorporating the RTD SOM is also proposed as shown in Fig. 4.11. It includes the same SNFTM circuit constituted of an RTD oscillator equipped with a probe tip, RTD SOM, and FDSM. In this scheme, when the probe tip moves closer to the sample placed on the piezo stage, the frequency variation occurs in the SNFTM circuit. This frequency-modulated signal is transferred to the RTD SOM circuit for down conversion and then ultimately to the FDSM. A brief discussion about mixers and the working of RTD SOM is discussed below.

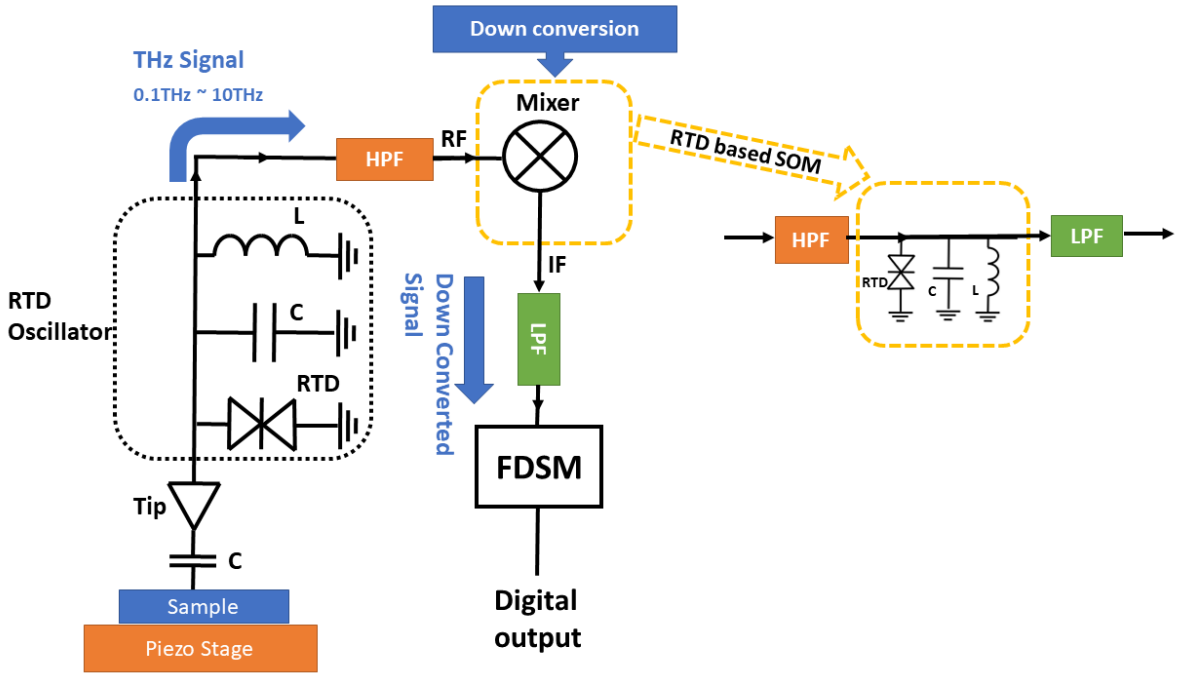

Figure 4.11 SNFTM employing RTD SOM

The main purpose of the mixer is to change the frequency of the signal. During down-conversion, the frequency of the input RF signal is reduced to a lower intermediate frequency (IF). This process permits further signal processing at a more manageable common frequency. Mixers for downconversion include three key ports such as radio frequency (RF) input port, local oscillator (LO) input port, and intermediate frequency (IF) output port. It receives data signal as an RF signal which in turn mixes with stable high frequency signal applied via LO oscillator port. As a result,

the IF port outputs a down-converted IF signal whose frequency is the difference of the RF and LO signals frequencies.

In conventional mixers, the high-frequency LO signal is difficult to deliver due to several factors such as Transmission line effects, parasitic effects of devices, etc. The SOM is also a type of mixer that integrates frequency conversion (IF signal) and oscillation generation function (LO signals) in a single device, making circuits simpler and minimizing components. So, an external LO is unnecessary in SOM. RTDs are also compatible for SOM due to depicting NDR region in IV characteristics and working as oscillator circuits. These RTD SOM are suitable for wireless communication, sensing, and imaging applications[245]. The purpose of using RTD SOM is its suitability for working in the THz region. In our proposed SNFTM employing RTD SOM, it is used for downconversion. A simple RTD-based oscillator circuit is used as a SOM which can be seen in Fig. 4.11. Like the SMOBILE-based SNFTM, here I also used BPF/HPF and LPF at the input and output ports, respectively, in order to provide isolation due to frequency differences.

4.4.1 Simulation of SNFTM employing RTD SOM

First, the simulation circuit is designed in order to achieve the desired circuit operation as shown in Fig. 4.12. This simulation circuit consists of an SNFTM oscillator circuit, probe tip circuit, BPF, RTD SOM, and LPF. All parameters' values used in Fig. 4.12 are mentioned in Table 4.2. In the SNFTM oscillator circuit, L_{in} is used to insert the inductance offered by connecting wires, R_{sup} is used to suppress the spurious oscillations and L_r is the parasitic inductance of R_{sup}. Here, the RTD model is the same as I discussed in section 2.3.2. C_{res} and L_{res} are working as LC resonator. The oscillator circuit with chosen parameters oscillates at 41.56 GHz. The probe tip circuit is composed

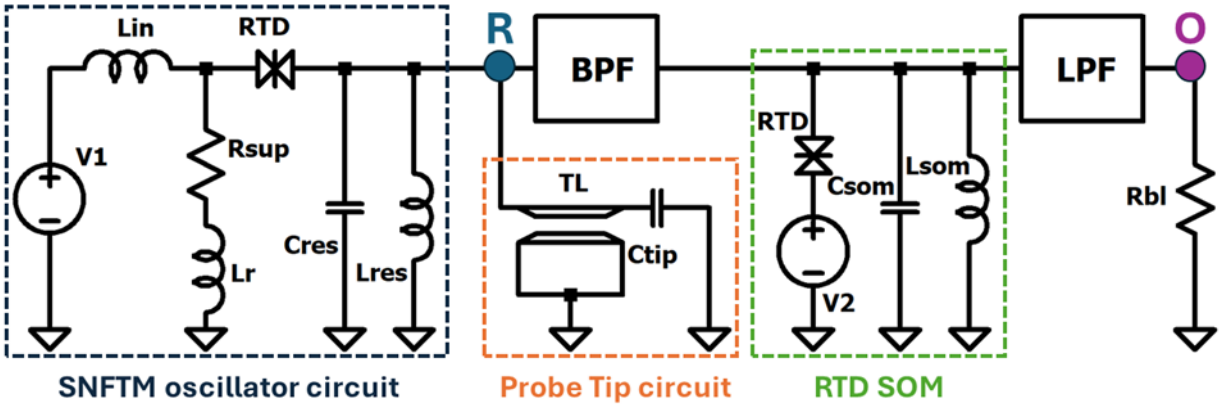

Figure 4.12 Simulation circuit designed for the SNFTM employing RTD SOM

of TL which is indispensable to connect the probe tip and capacitor (Ctip) which is formed between tip and sample upon moving closer. The Ctip value varies from 10 fF to 50 fF with steps of 10 fF resulting in change of fundamental frequency of the oscillator circuit. Then, a BPF with a cutoff frequency of 36 GHz-46.6 GHz is used to isolate the RTD SOM oscillations. RTD SOM circuit consists of a very simple RTD oscillator configuration where C_{som} and L_{som} constitute the LC resonator with a fundamental frequency of 30.73 GHz. Then LPF is used with a cutoff frequency of 14.6 GHz to receive the IF signal. The R_{bl} (50Ω) is broadband load resistance in place of the measurement device's input impedance. Simulation is performed by sweeping the C_{tip} value and resulting FFT of output collected at O port is shown in Fig. 4.13. In this figure,

Table 4.2 Parameters of the circuit shown in Fig. 4.12

SNFTM circuit		**RTD SOM**	
Parameters	Values	Parameters	Values
L_{in}	10 nH	C_{som}	0.1 pF
R_{sup}	5 Ω	L_{som}	0.2 nH
L_r	0.1 nH		
L_{res}	0.1 nH		
C_{res}	0.1 pF		
TL delay	22.3 ps		

the zoomed part is the region where distinct peaks of downconverted IF signals were supposed to appear but that was not the case. There are broad spectra near the expected IF peaks that attracted attention to verify if there exists a chaotic phenomenon. Because it is well known that power spectra of chaotic signals are broadband peaks. Here, it is important to note that the SNFTM circuit

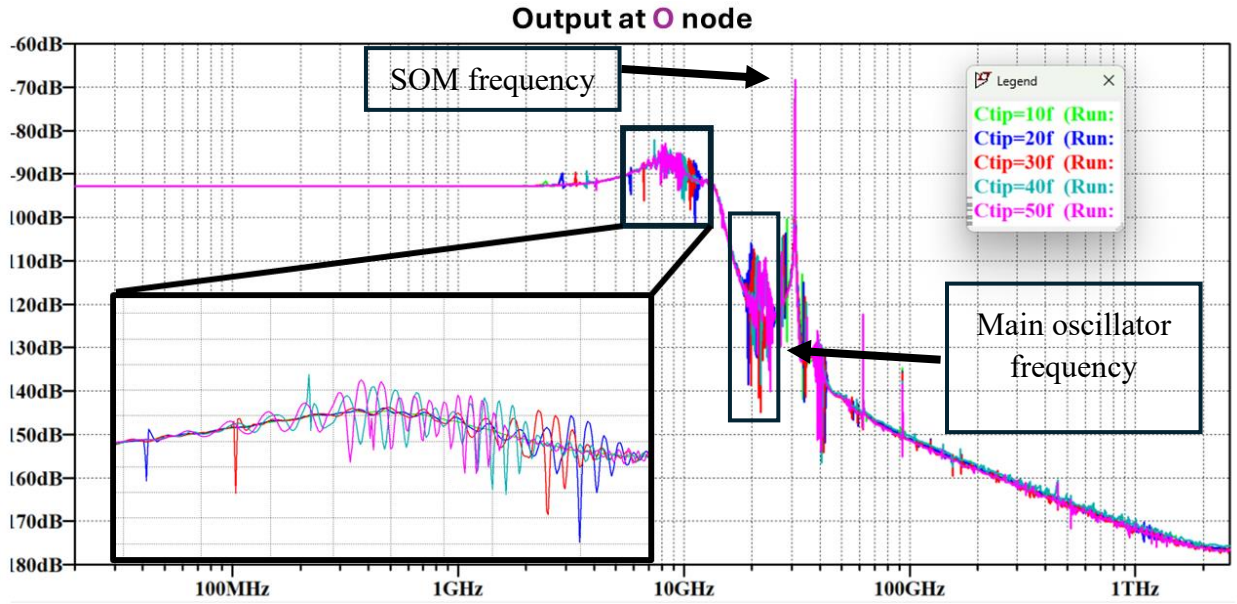

Figure 4.13 Simulated FFT of IF output signals at O node with different values of Ctip. When TL is inserted in Probe tip circuit

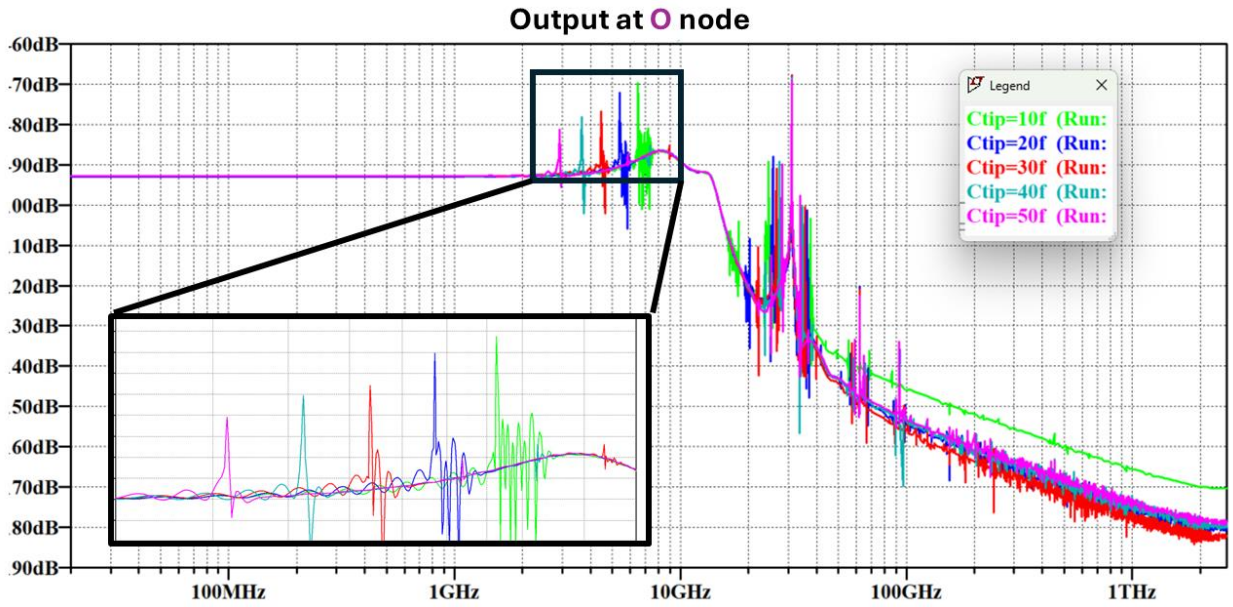

Figure 4.14 Simulated FFT of IF output signals at O node with different values of Ctip. When TL is eliminated from probe tip circuit

contains TL which can show strong nonlinearities as I demonstrated in section 2.3. So, in order to verify whether the nonlinearities arise due to TL or not, simulation is also performed by eliminating the TL from that circuit which is shown in Fig. 4.12. Figure 4.14 shows the output of the circuit by eliminating the TL from the circuit. The output is as expected depicting distinct peaks of IF signals upon varying the capacitance. For deep insight into this matter, the oscillation waveforms and their corresponding phase portraits are discussed.

4.4.2 Effects of transmission line

In order to investigate the transmission line effects in the SNFTM circuit, the simulation is performed with the circuit shown in Fig. 4.15. This circuit is basically the SNFTM circuit, but it is almost similar to the circuit I demonstrated as an RTD oscillator with a TL stub in Section 2.4. It is worth noting that the SNFTM circuit is integrated with the tip-sample capacitance but in the absence of a sample (eliminating C_{tip}) the circuit will become the same which I demonstrated in section 2.4. So, it is confirmed that this SNFTM circuit will show nonlinear behavior as the TL is working as a delayed feedback unit.

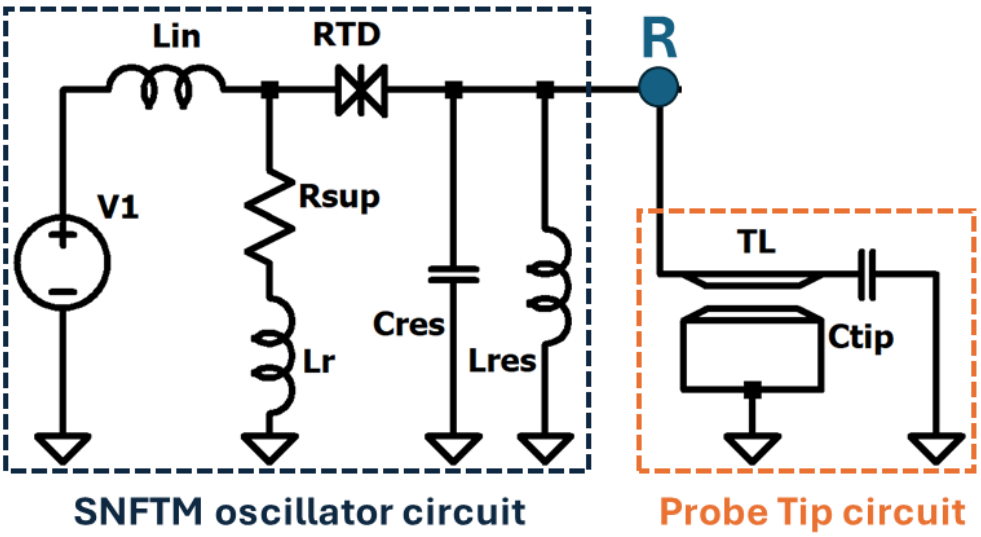

Figure 4.15 SNFTM circuit for simulation

The simulation output waveform and its corresponding phase portrait at Ctip 50 fF value are shown in Fig. 4. 16. It was expected to get periodic output waveforms and closed loop phase portraits, but this was not the case. The output waveform looks non-periodic and complex which is generated due to the TL nonlinearities as discussed above. To further verify the cause of nonlinearities, simulation is performed by eliminating the TL form the circuit shown in Fig. 4.15 while keeping the operating conditions the same. Figure 4.17 depicts the pure sinusoidal waveform and closed loop phase portrait which is the indication of perfect periodic output. So, it is verified that the origin of nonlinearities is the TL in the SNFTM circuit, which can pose a barrier to the correct operation of FDSM sensors that use RTD oscillators. The FDSM sensors detect frequency changes,

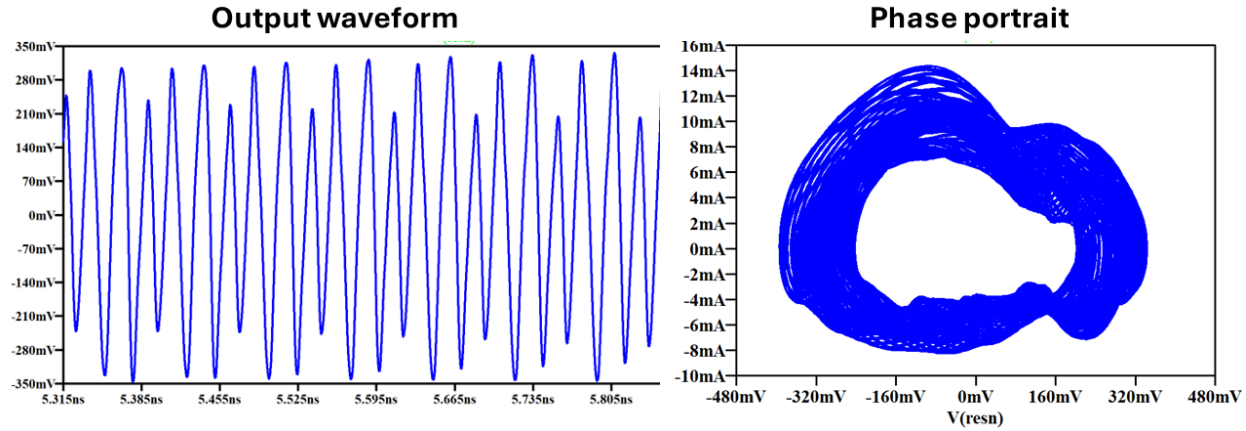

Figure 4.16 Output waveform and phase portrait incorporating TL in probe circuit tip

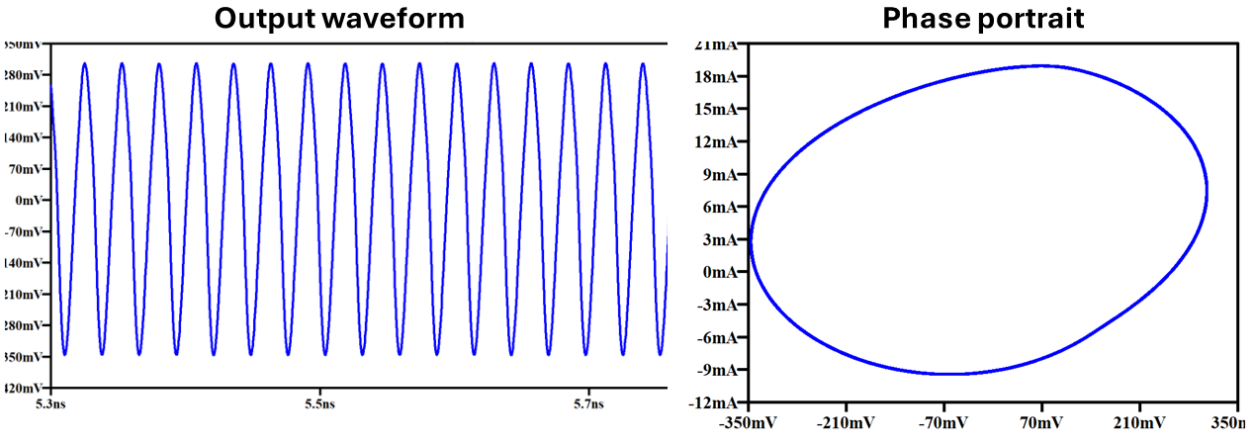

Figure 4.17 Output waveform and phase portrait incorporating TL in probe circuit tip

and the nonlinearities induced by the TL have a direct impact on the frequency of the output signal. To avoid these nonlinear effects, choosing a low characteristic impedance for the LC resonator is key to the proper and correct operation of FDSM sensors, as discussed in Section 2.5.

4.5 Scanning near field microwave microscope (SNMM)

To verify the basic working principle of the SNFTM experimentally, a scanning near-field microwave microscope (SNMM) is designed in the microwave frequency region for ease of measurement. The SNMM circuit is also fabricated using the same hybrid integration technique employed in previous experiments, providing a very easy, short, and compact method for circuit fabrication.

4.5.1 SNMM circuit fabrication

The experimental circuit for SNMM is shown in Fig. 4.18. The circuit consists of an RTD which serves as an NDR element, and a resistor R_{sup} is connected to suppress the spurious oscillations. L_r and C_r are used for the resonator. A tip is used for scanning the sample.

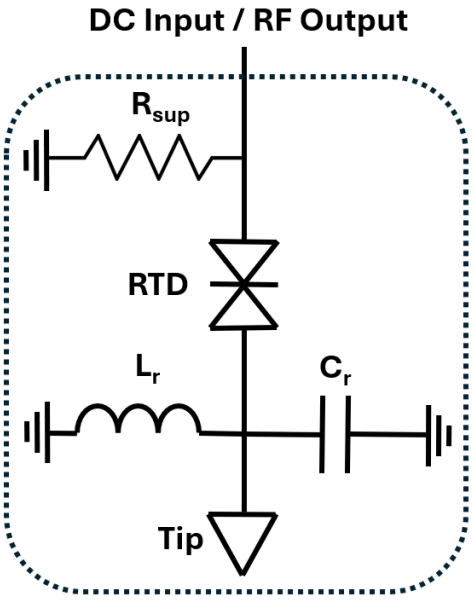

Figure 4.18 Experimental circuit design for SNMM

A 35 mm × 17 mm prototype circuit was fabricated with the hybrid integration technique on the 0.8 mm thick FR-4 PCB substrate by using an in-house InGaAs-based RTD chip, 1005-type chip elements, and a metal probe tip, as shown in Fig. 4.18. The chip elements and metal probe tip were integrated by soldering. The parameters of the elements used for fabricating the SNMM circuit were chosen to operate the circuit in the microwave frequency range and their values are depicted in Fig. 4.19. The resonator circuit's characteristic impedance was set to 10 Ω, a relatively low value, to minimize the nonlinearities introduced by the TL used for the probe tip. The conn ection of the RTD chip was facilitated by bonding wires. The measurement setup for SNMM illustrated in Fig. 4.19 consists of a piezo motor stage for scanning the sample in the XY direction and a microstage

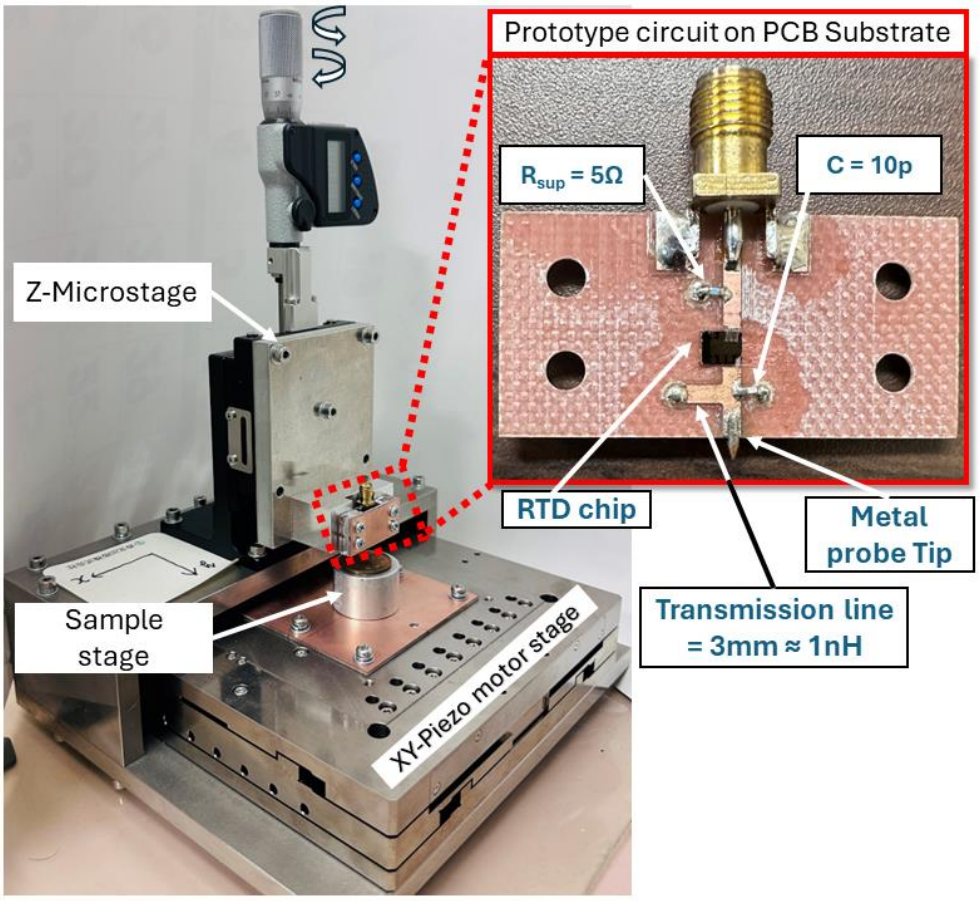

Figure 4.19 Fabricated scanning near-field microscope with a prototype SNMM circuit on the PCB substrate.

for height adjustment in the Z direction. The resolution in the XY direction is 10 nm, the maximum movement range is ±8 mm, and the resolution in the Z direction is 1 μm.

4.5.2 Experimental setup and results

Fig. 4.20 illustrates the experimental setup. A bias T was used to power the circuit with a DC signal and get an RF output. The output RF signal (fundamental frequency of circuit chosen to be around 1 GHz) was passed through LPF (2 GHz) to eliminate the high-frequency components, and amplified by the microwave amplifier (Keysight 83017A). Then the signal was divided into two branches, and fed to the spectrum analyzer and the sampling/digital filter circuit fabricated on a field programmable gate array (FPGA) [224]. Finally, the digital signal was transferred from the FPGA to the PC via TCP/IP to map the frequency change.

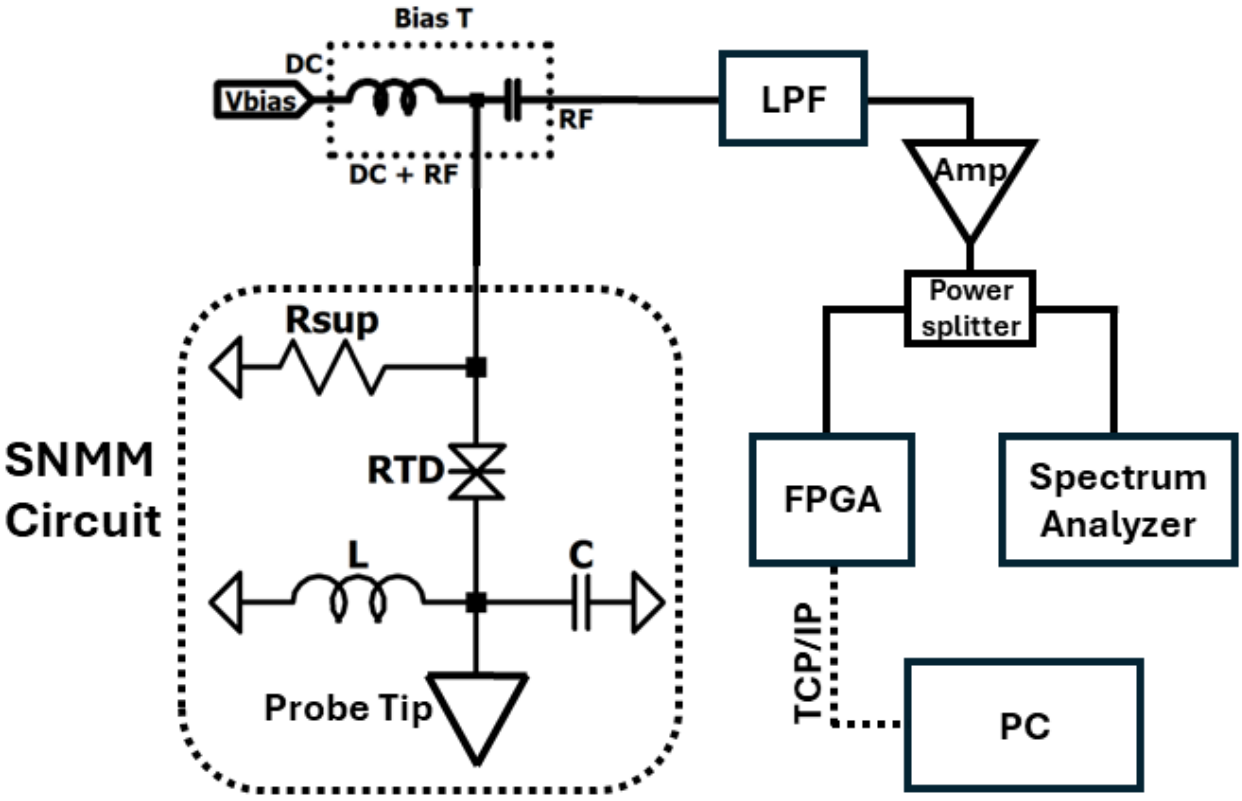

Figure 4.20 Experimental setup of SNMM for mapping the frequency change.

In the absence of a sample, the circuit oscillated at 1.027 GHz with a bias voltage of 930 mV. Figure 4.21 shows the change in frequency when the copper metal plate was used as a sample. It was clearly demonstrated that the oscillation frequency decreases when the tip-sample distance decreases. The magnitude of the frequency change was large enough for the FDSM.

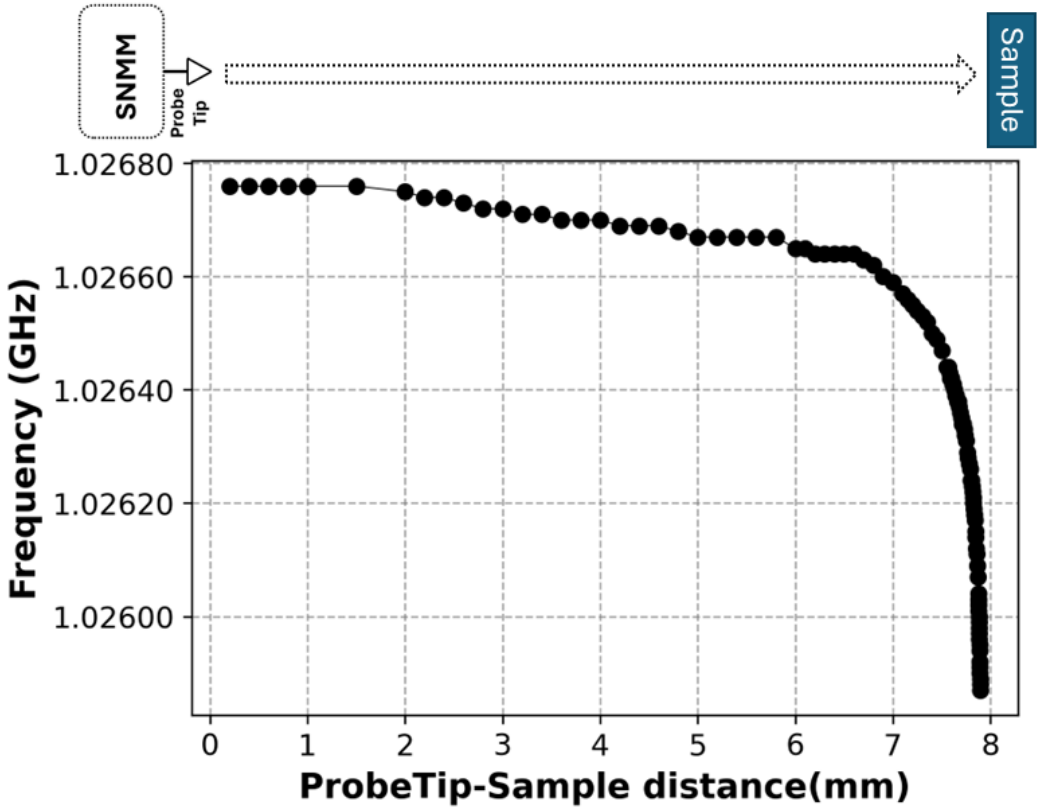

Figure 4.21 Frequency change with respect to the gap between Tip and sample.

Next, I scanned the surface of a 10-yen coin. Figure 4.22 shows the scanned image mapped by frequency tracking of the 10×10 mm^2 area with a step of 100 μm and height of approximately 33 μm. A clear image of Phoenix-Hall was obtained. This measurement represents the height of the sample. Since variations in the gap (height) lead to changes in frequency, the observed frequency shift corresponds directly to changes in height. This relationship is captured and analyzed using a frequency tracking map. The resolution of the image was limited by the step size, tip-sample

distance, and the radius of the tip apex. The sample-tip distance and the dielectric constant of the sample both affect the oscillation frequency, and the separation of each information can be solved by integrating the displacement sensor as discussed in the previous section 3.5. Nevertheless, it was demonstrated that a high-resolution image beyond the diffraction limit can be obtained with this prototype device.

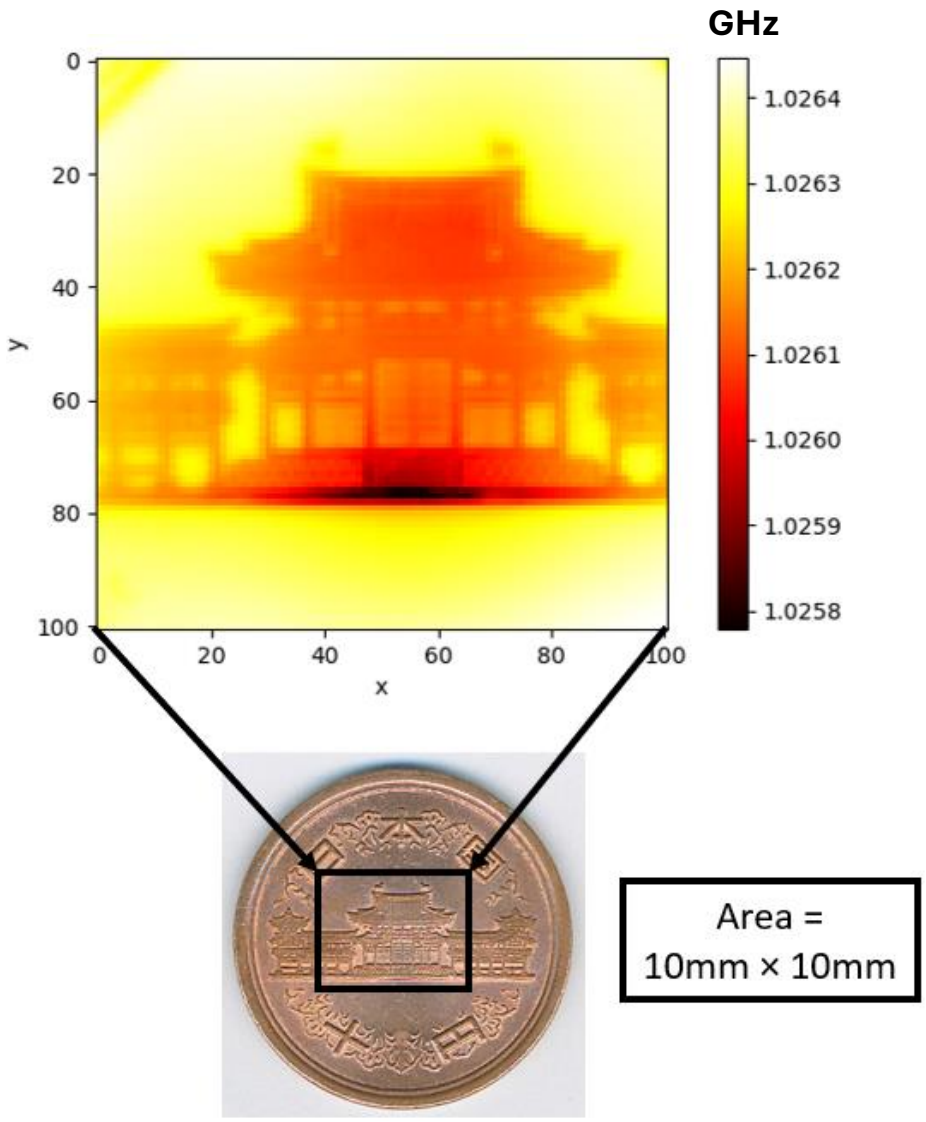

Figure 4.22 Scanned height measurement image of Phoenix Hall designed on 10-yen coin.

4.6 Summary

The concept of the FDSM-based SNFTM circuit employing the RTD oscillators equipped with probe tip for imaging was proposed. This concept is presented to operate the SNFTM circuit in the THz range. Direct sampling of high-frequency signals is challenging. To overcome this difficulty, two ways of transforming THz signals to low-frequency signals are proposed. First, the SMOBILE using a pair of RTDs with frequency-based input/output isolation for undersampling is proposed. The circuit simulation demonstrated proper operation at 500 GHz input with a 10 GHz complementary clock signal for sampling. Moreover, the basic operation was experimentally demonstrated showing good eye opening which indicates a large phase margin. Second, the SNFTM employing RTD SOM is proposed where the downconversion is achieved with the simple RTD oscillator circuit working as a SOM. The Simulation results showed that this method works well for observing frequency change by down-converting the signal. However, the nonlinearities put the hindrance in observing the frequency change which was induced by the transmission line used to facilitate the connection to the probe tip in the SNFTM circuit. This was confirmed by simulating the circuit with and without a transmission line. By eliminating the TL from the circuit, a clear frequency change was observed by plotting the FFT of output signals. Choosing a low characteristic impedance of the resonator circuit is one of the solutions to avoid the TL nonlinearities. Finally, to verify the basic working principle of the SNFTM experimentally, a prototype device was fabricated in the microwave frequency region for ease of measurement. A very clear image of Phoenix-Hall was obtained by scanning the surface of a 10-yen coin. It was demonstrated that a high-resolution image beyond the diffraction limit can be obtained with this prototype device.

Chapter 5 Conclusion

In this thesis, the nonlinearities exhibited by RTD oscillators due to their nonlinear unique IV characteristics were investigated with the aim of finding their impact on the FDSM sensors. A detailed experimental characterization of the nonlinear behavior of the RTD oscillators was achieved by applying the sinusoidal signal to the RTD oscillator while powering it in the NDR region. Next it was found that the RTD oscillators show nonlinear behavior if the transmission line as an open stub is connected to it. Here, nonlinear behavior refers to the generation of complex output signals including chaos. These findings allowed us to design the proposed SNFTM circuits employing the RTD oscillators suitable for the FDSM technique while avoiding the nonlinear effects that can impede the proper operation of sensors. The simulation results showed that these effects can interfere with the proper operation of sensors. Additionally, the potential of RTD oscillators for sensor applications was also demonstrated. Overall, these findings carry great importance in applying the RTD oscillators for THz range sensors in conjunction with a superior FDSM AD conversion technique.

In Chapter 1, the broad range of applications of THz waves was discussed, especially noninvasive sensing applications for imaging in the fields of physics, chemistry, biomedical, pharmaceutical, and material science. The comparison of various THz sources was presented, and it was concluded that the RTD is the best candidate for the THz source, possessing prominent features such as unique IV characteristics and room-temperature THz range operation in oscillator circuits.

In Chapter 2, the nonlinear phenomena that exist in the RTD oscillators were demonstrated in detail. First, I validated and characterized the resonant tunneling chaos generator circuit in depth at the microwave frequency range. The circuit was fabricated on the PCB substrate employing the

RTD chip and chip elements. This hybrid fabrication method proved to emulate the circuit as per circuit design without a long and complicated process. Microwave chaos was controlled and visualized on the sampling oscilloscope using a periodic reset technique in order to process data for detailed characterization. Longer period output up to 58 periods of input signal was achieved, which is approximately 3 times larger than those in the previous reports. This permitted us to characterize output signals, in particular, the calculation of Lyapunov exponents. I also found that the conventional methods of plotting bifurcation diagrams from time series data failed due to frequency-dependent phase difference errors. The proper bifurcation diagram was plotted using a compensation scheme based on the oscillation period in the conventional bifurcation diagram. A cascade of periodic and chaos regimes was exhibited on the experimental bifurcation diagram by sweeping input frequency from 2.4 GHz to 9 GHz. Single-period, double-period, chaos, and triple-period regimes were identified by plotting their time series waveforms, power spectrum, phase portraits, and return maps. The circuit's deterministic chaos was further proven by estimating the positive Lyapunov exponent from the time series waveform. These results indicate that the periodical resetting scheme should be a good tool for characterizing chaos in high-frequency regimes.

Secondly, the behavior of RTD oscillators with an open TL stub was investigated as a function of the stub length. First, a circuit simulation was performed to clarify the basic phenomena caused by the stub. It was found that the open stub induces strong nonlinearities in the RTD oscillators, leading to the evolution of complex behavior, including chaos. To confirm the simulation results, I fabricated and tested RTD oscillators with an open TL stub. The circuit was fabricated using a hybrid integration technique. The experimental results showed chaotic and periodic output waveforms by varying the open stub length. Consequently, this circuit has potential as a simple

chaos generator in the THz frequency range. Moreover, understanding the effects of such a TL stub is also important for the design of THz circuits using RTDs, since even a small metal pattern or interconnection wires can cause such a feedback effect in the THz frequency range. Nevertheless, To apply RTD oscillators to sensors effectively, it is crucial to eliminate these nonlinear effects. The nonlinearities caused by the TL pose a barrier to using RTD oscillators in sensor applications. These nonlinearities can significantly affect the sensor's performance. Simulation and experimental results showed that the nonlinearities due to TL can be significantly eliminated by choosing the low resonator characteristic impedance. However, variation of output power and change in fundamental frequency was observed both in simulation and experiments. Variation of output power can be attributed to the reflection of signal with constructive and destructive interference. Moreover, a change in stub length has an impact on the equivalent value of the LC resonator which results in a change of fundamental frequency.

In Chapter 3, the operating principle of FDSM based AD converters and sensors was discussed. The integration of analog-to-digital conversion is essential for modern digital systems, particularly in enhancing the functionality and versatility of sensors. High-performance sensors demand superior ADCs, and delta-sigma modulation ADCs (DSADCs) are highly valued for their high-resolution capabilities. Conventional DSADCs face limitations due to their integrator and feedback DAC components. FDSM is a promising alternative that uses a voltage-controlled oscillator (VCO) to convert an analog signal to a frequency-modulated intermediate signal, which is then converted to a pulse-density-modulated digital signal. This method eliminates feedback loops and DACs, resulting in increased bandwidth, dynamic range, signal-to-noise ratio, and resolution. Furthermore, using variable frequency oscillators instead of VCOs can greatly improve sensor performance. RTD-based THz oscillators can be used to provide high-performance sensors by

simply replacing the VCO in the FDSM. As an example of the FDSM sensors, the stylus profiler was discussed. A novel type of displacement sensor was proposed based on the FDSM. A cylindrical cavity resonator with a diaphragm at one end of the cavity was used for the variable frequency oscillator, which is a core of the FDSM. This can be applied to a stylus surface profiler and an AFM, when a probe tip is set at the diaphragm. To demonstrate basic operation, I fabricated a stylus surface profiler. A good surface profile was successfully obtained with this device. A 10 nm depth trench was measured together with a 10 μm trench in a single scan without gain control. This result clearly demonstrates the extremely wide dynamic range of the FDSM displacement sensor. Additionally, it depicted that the performance of FDSM sensors strongly depends on the frequency modulation width. It implies that the higher oscillation frequency is preferable since the modulation ratio remains constant in most cases. So, the high-performance unprecedented sensors can be realized by using RTD-based THz oscillators.

In Chapter 4, the concept of an FDSM-based SNFTM circuit using RTD oscillators equipped with a probe tip for imaging was proposed. This concept was designed to operate the SNFTM circuit in the THz range. Direct sampling of high-frequency signals in this range is challenging. To address this issue, two methods for transforming THz signals into low-frequency signals were proposed. First, the SMOBILE using a pair of RTDs with frequency-based input/output isolation for under-sampling is proposed. The circuit simulation demonstrated proper operation at 500 GHz input with a 10 GHz complementary clock signal for sampling. Moreover, the basic operation was experimentally demonstrated showing good eye opening which indicates a large phase margin. Second, the SNFTM employing RTD SOM is proposed where the downconversion is achieved with the simple RTD oscillator circuit working as a SOM. The Simulation results showed this method works well for observing frequency change by down-converting the signal. However, the

nonlinearities put a hindrance in observing the frequency change which was induced by the transmission line used to facilitate the connection to the probe tip in the SNFTM circuit. This was confirmed by simulating the circuit with and without a transmission line. By eliminating the TL from the circuit, a clear frequency change was observed by plotting the FFT of output signals. Choosing a low characteristic impedance of the resonator circuit is one of the solutions to avoid the TL nonlinearities. Finally, to verify the basic working principle of the SNFTM experimentally, a prototype device was fabricated in the microwave frequency region for ease of measurement. A very clear image of Phoenix-Hall was obtained by scanning the surface of a 10-yen coin. It was demonstrated that a high-resolution image beyond the diffraction limit can be obtained with this prototype device.

Since the RTD is a promising candidate among various THz sources. So, the findings of this thesis carry great importance in realizing the THz range sensor applications of RTD oscillators in conjunction with the FDSM technique.

Acknowledgements

I am deeply grateful to Allah Almighty, the compassionate and merciful, the sole creator and Lord of the universe, the source of all knowledge and wisdom. His boundless mercy, countless blessings, and infinite guidance have been my greatest support throughout this journey. Without His grace, I would not have had the strength or courage to complete this study and dissertation. I thank Him for bestowing upon me the perseverance and resilience needed to overcome the challenges I faced.

I extend my utmost tributes and profound gratitude to the Holy Prophet Hazrat Muhammad (Peace be upon Him). His exemplary moral and spiritual teachings have illuminated my path, inspiring me to strive for excellence in all aspects of life. The love and wisdom imparted by the Holy Prophet Hazrat Muhammad (Peace be upon Him) have been a constant source of enlightenment and motivation, shaping my character and guiding me toward success. May His teachings continue to guide and bless us all.

Words cannot adequately express my gratitude to my family. I dedicate this dissertation to my parents, whose unwavering love, prayers, and support have been invaluable blessings from Allah. Despite not having a strong financial background, they have always stood by me, providing everything I needed to pursue my dreams. Their sacrifices, encouragement, and belief in my abilities have been the driving forces behind my academic journey. Without their endless support and motivation, this achievement would not have been possible. I am eternally grateful for their boundless love and dedication.

My heartfelt thanks go to my former supervisor, Professor Koichi Maezawa. His kindness and support throughout my Master's and Ph.D. journey have been invaluable. During my five-year stay in the Microelectronics Laboratory at the University of Toyama, Professor Maezawa's unwavering

patience, insightful feedback, and constant encouragement have been instrumental in the successful completion of my research. The intelligent and intellectual discussions during our monthly seminars provided deep insights into my research. His stimulating guidance, moral support, and genuine interest have greatly improved this manuscript. I am deeply grateful for his dedication to my academic and personal growth.

I am deeply indebted to my current supervisor, Professor Masayuki Mori, who has been exceptionally helpful in every matter. His dexterous guidance and valuable suggestions have been indispensable throughout my studies, research, and daily life in Japan. His continuous support, insightful advice, and thoughtful mentorship have not only enhanced my academic work but also enriched my personal and professional development. I am profoundly grateful for his unwavering commitment to my success and well-being. I am so grateful to Prof. Shigeki Naka and Prof. Safumi Suzuki for serving as the referees of my thesis defense. Their valuable comments were instrumental for me to complete this thesis.

I also want to express my sincere thanks to Mr. Ueda, a staff member of nanoelectronics lab, university of Toyama, for his invaluable help and thoughtful advice during my experiments. His expertise, particularly in bonding wires required for circuit fabrication, has been instrumental in the success of my research. Also, special thanks to all students of my laboratory who never hesitated to help me in my research as well as in documentation, especially, Motomura-San, Ohtera-San, Kato-San, Aizawa-San, Nishita-San, Ueki-San, Nakamura-San, Matsuura-San, Mr. Nakazaki, Kawai-Kun, and Tamura-Kun.

I am extremely thankful for the scholarship support provided by the Otsuka Toshimi Scholarship Foundation and the Rotary Yoneyama Memorial Foundation, as well as the research grant provided

by the Marubun Research Promotion Foundation. Their generous support has greatly facilitated the completion of this dissertation.

I am also deeply grateful to my elder brother, Dr. Muhammad Shahzad, whose financial support for my journey to Japan is unforgettable. His unwavering love and encouragement have always made me proud. My sisters, with their endless love and prayers, are a great blessing, providing constant support and inspiration throughout my academic endeavors.

I would like to express my sincere gratitude to one of my seniors, Dr. Allah Nawaz, Post-doctoral Research Fellow at the Joslin Diabetes Center, Harvard Medical School. His support in helping me secure admission to the University of Toyama, Japan, is invaluable and cannot be repaid. He went above and beyond to assist me in settling into life in Japan when I was feeling completely lost and overwhelmed. His guidance and support were crucial during that time, and I am forever grateful for his kindness and generosity.

I would like to express my deepest gratitude to my childhood best friend, Abdul Rehman Mirza, whose unwavering support and friendship have been a constant source of strength throughout this journey. Your belief in me, from our earliest days together to this moment, has meant more than words can say. Thank you for always being there, through every challenge and success.

While living in Toyama, Japan, the companionship and love from Dr. Tanvir Ahmed, Dr. Zakki Ahmed, Dr. Ishtiaq Jeelani, Dr. Muhammad Bilal, Dr. Aamir Sharif, Dr. Muhammad Rahil, Dr. Abdul Hayee, Dr. Khaleeq Ahmed, Dr. Bilal Ahmed Mir, Mr. Tahir Iqbal, Dr. Shahdil Ibrahim, Abrar Ahmed, Waseem Abbass, Muhammad Irshad, Shaikh Shoeb, and Muaz Fahri Anggara are beyond words.

My deepest gratitude also goes to those who indirectly contributed to this research. Your kindness means a lot to me.

May Allah bless all of you with long, prosperous, and happy lives (Aameen).

Umer Farooq

Bibliography

[1] D. M. Mittleman, S. Hunsche, L. Boivin, and M. C. Nuss, “T-ray tomography,” *Optics Letters, Vol. 22, Issue 12, pp. 904-906*, vol.22, no. 12, pp.904–906, Jun. 1997.

[2] K. C. Huang and Z. Wang, “Terahertz terabit wireless communication,” *IEEE Microw Mag*, vol.12, no. 4, pp.108–116, Jun. 2011.

[3] J. F. O’Hara, S. Ekin, W. Choi, and I. Song, “A Perspective on Terahertz Next-Generation Wireless Communications,” *Technologies 2019, Vol. 7, Page 43*, vol.7, no. 2, p.43, Jun. 2019.

[4] A. Gong, Y. Qiu, X. Chen, Z. Zhao, L. Xia, and Y. Shao, “Biomedical applications of terahertz technology,” *Appl Spectrosc Rev*, vol.55, no. 5, pp.418–438, May 2020.

[5] D. M. Mittleman, M. Gupta, R. Neelamani, R. G. Baraniuk, J. V. Rudd, and M. Koch, “Recent advances in terahertz imaging,” *Appl Phys B*, vol.68, no. 6, pp.1085–1094, 1999.

[6] M.-A. Brun, F. Formanek, A. Yasuda, M. Sekine, N. Ando, and Y. Eishii, “Terahertz imaging applied to cancer diagnosis,” *Phys Med Biol*, vol.55, no. 16, p.4615, 2010.

[7] G. Tzydynzhapov, P. Gusikhin, V. Muravev, A. Dremin, Y. Nefyodov, and I. Kukushkin, “New Real-Time Sub-Terahertz Security Body Scanner,” *J Infrared Millim Terahertz Waves*, vol.41, no. 6, pp.632–641, Jun. 2020.

[8] Y. C. Shen, “Terahertz pulsed spectroscopy and imaging for pharmaceutical applications: A review,” *Int J Pharm*, vol.417, no. 1–2, pp.48–60, Sep. 2011.

[9] G. P. Williams, “Filling the THz gap—high power sources and applications,” *Reports on Progress in Physics*, vol.69, no. 2, p.301, Dec. 2005.

[10] T. Nagatsuma, G. Ducournau, and C. C. Renaud, “Advances in terahertz communications accelerated by photonics,” *Nature Photonics 2016 10:6*, vol.10, no. 6, pp.371–379, May 2016.

[11] R. A. Lewis, “A review of terahertz sources,” *J Phys D Appl Phys*, vol.47, no. 37, p.374001, Aug. 2014.

[12] K. Maezawa, “Resonant Tunneling Diodes,” *Wiley Encyclopedia of Electrical and Electronics Engineering*, pp.1–7, 1999.

[13] R. Izumi, S. Suzuki, and M. Asada, “1.98 THz resonant-tunneling-diode oscillator with reduced conduction loss by thick antenna electrode,” 2017 42nd International Conference on Infrared, Millimeter, and Terahertz Waves (IRMMW-THz), pp.1–2, 2017.

[14] T. Shiode, T. Mukai, M. Kawamura, and T. Nagatsuma, "Giga-bit wireless communication at 300 GHz using resonant tunneling diode detector," Asia-Pacific Microwave Conference 2011, pp.1122–1125, 2011.

[15] N. Oshima, K. Hashimoto, S. Suzuki, and M. Asada, "Wireless data transmission of 34 Gbit/s at a 500-GHz range using resonant-tunnelling-diode terahertz oscillator," *Electron Lett*, vol.52, no. 22, pp.1897–1898, 2016.

[16] N. Oshima, K. Hashimoto, S. Suzuki, and M. Asada, "Terahertz wireless data transmission with frequency and polarization division multiplexing using resonant-tunneling-diode oscillators," *IEEE Trans Terahertz Sci Technol*, vol.7, no. 5, pp.593–598, 2017.

[17] M. J. Ogorzalek, Chaos and complexity in nonlinear electronic circuits, vol.22. World Scientific, 1997.

[18] H. G. Schuster and W. Just, Deterministic chaos: an introduction. John Wiley & Sons, 2006.

[19] H. Dedieu and M. Ogorzałek, "Chaos-based signal processing," *International Journal of Bifurcation and Chaos*, vol.10, no. 04, pp.737–748, 2000.

[20] A. Argyris, D. Syvridis, L. Larger, V. Annovazzi-Lodi, P. Colet, I. Fischer, J. Garcia-Ojalvo, C. R. Mirasso, L. Pesquera, and K. A. Shore, "Chaos-based communications at high bit rates using commercial fibre-optic links," *Nature*, vol.438, no. 7066, pp.343–346, 2005.

[21] K. Murali, H. Yu, V. Varadan, and H. Leung, "Secure communication using a chaos based signal encryption scheme," *IEEE Transactions on Consumer Electronics*, vol.47, no. 4, pp.709–714, 2001.

[22] A. A. Zaher, "Duffing oscillators for secure communication," *Computers & Electrical Engineering*, vol.71, pp.77–92, 2018.

[23] S. Callegari, R. Rovatti, and G. Setti, "Embeddable ADC-based true random number generator for cryptographic applications exploiting nonlinear signal processing and chaos," *IEEE transactions on signal processing*, vol.53, no. 2, pp.793–805, 2005.

[24] M. P. Kennedy and G. Kolumban, "Digital communications using chaos," *Signal Processing*, vol.80, no. 7, pp.1307–1320, 2000.

[25] S. Li, A. Sanyal, K. Lee, Y. Yoon, X. Tang, Y. Zhong, K. Ragab, and N. Sun, "Advances in Voltage-Controlled-Oscillator-Based ΔΣ ADCs," *IEICE Transactions on Electronics*, vol.E102.C, no. 7, pp.509–519, Jul. 2019.

[26] A. Iwata, N. Sakimura, M. Nagata, and T. Morie, "The architecture of delta sigma analog-to-digital converters using a voltage-controlled oscillator as a multibit quantizer," *IEEE*

Transactions on Circuits and Systems II: Analog and Digital Signal Processing, vol.46, no. 7, pp.941–945, 1999.

[27] M. Hovin, A. Olsen, T. S. Lande, and C. Toumazou, "Delta-sigma modulators using frequency-modulated intermediate values," *IEEE J Solid-State Circuits*, vol.32, no. 1, pp.13–22, 1997.

[28] K. Maezawa and M. Mori, "Effects of Oscillator Phase Noise on Frequency Delta Sigma Modulators with a High Oversampling Ratio for Sensor Applications," *IEICE Transactions on Electronics*, vol.E104.C, no. 9, pp.463–466, Sep. 2021.

[29] M. Tonouchi, "Cutting-edge terahertz technology," *Nature Photonics 2007 1:2*, vol.1, no. 2, pp.97–105, Feb. 2007.

[30] T. Hochrein, "Markets, Availability, Notice, and Technical Performance of Terahertz Systems: Historic Development, Present, and Trends," *J Infrared Millim Terahertz Waves*, vol.36, no. 3, pp.235–254, Mar. 2015.

[31] T. Robin, C. Bouye, and J. Cochard, "Terahertz applications: trends and challenges," *https://doi.org/10.1117/12.2043284*, vol.8985, pp.143–148, Mar. 2014.

[32] T. Nagatsuma, "Terahertz technologies: present and future," *IEICE Electronics Express*, vol.8, no. 14, pp.1127–1142, 2011.

[33] P. H. Siegel, "THz Technology: An Overview," *https://doi.org/10.1142/S0129156403001776*, vol.13, no. 2, pp.351–394, May 2012.

[34] P. H. Siegel, "Terahertz technology," *IEEE Trans Microw Theory Tech*, vol.50, no. 3, pp.910–928, Mar. 2002.

[35] N. Kida, T. Miyamoto, and H. Okamoto, "Emission of Terahertz Electromagnetic Waves: A New Spectroscopic Method to Investigate Physical Properties of Solids," *https://doi.org/10.7566/JPSJ.91.112001*, vol.91, no. 11, Oct. 2022.

[36] T. Amini, F. Jahangiri, Z. Ameri, and M. A. Hemmatian, "A Review of Feasible Applications of THz Waves in Medical Diagnostics and Treatments: Feasible Applications of THz Waves in Medicine," *J Lasers Med Sci*, vol.12, no. 1, pp.e92–e92, Dec. 2021.

[37] L. Yu, L. Hao, T. Meiqiong, H. Jiaoqi, L. Wei, D. Jinying, C. Xueping, F. Weiling, and Z. Yang, "The medical application of terahertz technology in non-invasive detection of cells and tissues: opportunities and challenges," *RSC Adv*, vol.9, no. 17, pp.9354–9363, Mar. 2019.

[38] S. J. Jo, S. Y. Yoon, J. Y. Lee, K. T. Kim, S. Jung, J. Park, G. S. Park, W. Y. Park, and O. Kwon, "Biological effects of femtosecond-terahertz pulses on C57BL/6 mouse skin," *Ann Dermatol*, vol.26, no. 1, pp.129–132, 2014.

[39] B. S. Alexandrov, K. Ø. Rasmussen, A. R. Bishop, A. Usheva, L. B. Alexandrov, S. Chong, Y. Dagon, L. G. Booshehri, C. H. Mielke, M. L. Phipps, J. S. Martinez, H.-T. Chen, and G. Rodriguez, "Non-thermal effects of terahertz radiation on gene expression in mouse stem cells," *Biomed Opt Express*, vol.2, no. 9, pp.2679–2689, Sep. 2011.

[40] L. Zhao, Y.-H. Hao, and R.-Y. Peng, "Advances in the biological effects of terahertz wave radiation," *Military Medical Research 2014 1:1*, vol.1, no. 1, pp.1–4, Dec. 2014.

[41] S. W. Smye, J. M. Chamberlain, A. J. Fitzgerald, and E. Berry, "The interaction between Terahertz radiation and biological tissue," *Phys Med Biol*, vol.46, no. 9, p.R101, Aug. 2001.

[42] M. Tamosiunaite, S. Tamosiunas, M. Z. and G. Valusis, M. Tamosiunaite, S. Tamosiunas, and M. Z. and G. Valusis, "Atmospheric Attenuation of the Terahertz Wireless Networks," *Broadband Communications Networks - Recent Advances and Lessons from Practice*, Dec. 2017.

[43] T. Nagatsuma, K. Oogimoto, Y. Inubushi, and J. Hirokawa, "Practical considerations of terahertz communications for short distance applications," *Nano Commun Netw*, vol.10, pp.1–12, Dec. 2016.

[44] A. Batra, J. Barowski, D. Damyanov, M. Wiemeler, I. Rolfes, T. Schultze, J. C. Balzer, D. Göhringer, and T. Kaiser, "Short-Range SAR Imaging From GHz to THz Waves," *IEEE Journal of Microwaves*, vol.1, no. 2, pp.574–585, Apr. 2021.

[45] M. C. Beard, G. M. Turner, and C. A. Schmuttenmaer, "Terahertz spectroscopy," *Journal of Physical Chemistry B*, vol.106, no. 29, pp.7146–7159, Jul. 2002.

[46] G. Li, R. V Mikhaylovskiy, K. A. Grishunin, J. D. Costa, T. Rasing, and A. V Kimel, "Laser induced THz emission from femtosecond photocurrents in Co/ZnO/Pt and Co/Cu/Pt multilayers," *J Phys D Appl Phys*, vol.51, no. 13, p.134001, 2018.

[47] J. P. Guillet, B. Recur, L. Frederique, B. Bousquet, L. Canioni, I. Manek-Hönninger, P. Desbarats, and P. Mounaix, "Review of terahertz tomography techniques," *J Infrared Millim Terahertz Waves*, vol.35, no. 4, pp.382–411, Feb. 2014.

[48] V. Y. Fedorov and S. Tzortzakis, "Powerful terahertz waves from long-wavelength infrared laser filaments," *Light: Science & Applications 2020 9:1*, vol.9, no. 1, pp.1–16, Nov. 2020.

[49] A. Dobroiu, M. Yamashita, Y. N. Ohshima, Y. Morita, C. Otani, and K. Kawase, "Terahertz imaging system based on a backward-wave oscillator," *Applied Optics, Vol. 43, Issue 30, pp. 5637-5646*, vol.43, no. 30, pp.5637–5646, Oct. 2004.

[50] D. Clery, "Sensing: Brainstorming their way to an imaging revolution," *Science (1979)*, vol.297, no. 5582, pp.761–763, Aug. 2002.

[51] D. L. Woolard, E. R. Brown, M. Pepper, and M. Kemp, "Terahertz frequency sensing and imaging: A time of reckoning future applications?," *Proceedings of the IEEE*, vol.93, no. 10, pp.1722–1743, 2005.

[52] R. Knipper, A. Brahm, E. Heinz, T. May, G. Notni, H. G. Meyer, A. Tunnermann, and J. Popp, "THz absorption in fabric and its impact on body scanning for security application," *IEEE Trans Terahertz Sci Technol*, vol.5, no. 6, pp.999–1004, Nov. 2015.

[53] C. Corsi and F. Sizov, THz and security applications: detectors, sources and associated electronics for THz applications. Springer, 2014.

[54] H. Cheon, H. J. Yang, and J. H. Son, "Toward Clinical Cancer Imaging Using Terahertz Spectroscopy," *IEEE Journal of Selected Topics in Quantum Electronics*, vol.23, no. 4, Jul. 2017.

[55] Y. Peng, C. Shi, X. Wu, Y. Zhu, and S. Zhuang, "Terahertz Imaging and Spectroscopy in Cancer Diagnostics: A Technical Review," *BME Front*, vol.2020, Jan. 2020.

[56] M. Gezimati and G. Singh, "Advances in terahertz technology for cancer detection applications," *Opt Quantum Electron*, vol.55, no. 2, pp.1–38, Feb. 2023.

[57] S. Koenig, D. Lopez-Diaz, J. Antes, F. Boes, R. Henneberger, A. Leuther, A. Tessmann, R. Schmogrow, D. Hillerkuss, R. Palmer, T. Zwick, C. Koos, W. Freude, O. Ambacher, J. Leuthold, and I. Kallfass, "Wireless sub-THz communication system with high data rate," *Nature Photonics 2013 7:12*, vol.7, no. 12, pp.977–981, Oct. 2013.

[58] H. Elayan, O. Amin, R. M. Shubair, and M. S. Alouini, "Terahertz communication: The opportunities of wireless technology beyond 5G," *Proceedings - 2018 International Conference on Advanced Communication Technologies and Networking, CommNet 2018*, pp.1–5, May 2018.

[59] A. Y. Pawar, D. D. Sonawane, K. B. Erande, and D. V. Derle, "Terahertz technology and its applications," *Drug Invention Today*, vol.5, no. 2, pp.157–163, Jun. 2013.

[60] P. Shumyatsky and R. R. Alfano, "Terahertz sources," *https://doi.org/10.1117/1.3554742*, vol.16, no. 3, p.033001, Mar. 2011.

[61] H. J. Song and T. Nagatsuma, "Present and future of terahertz communications," *IEEE Trans Terahertz Sci Technol*, vol.1, no. 1, pp.256–263, Sep. 2011.

[62] M. A. Dem'yanenko, D. G. Esaev, B. A. Knyazev, G. N. Kulipanov, and N. A. Vinokurov, "Imaging with a 90 framess microbolometer focal plane array and high-power terahertz free electron laser," *Appl Phys Lett*, vol.92, no. 13, Mar. 2008.

[63] B. A. Knyazev, G. N. Kulipanov, and N. A. Vinokurov, “Novosibirsk terahertz free electron laser: instrumentation development and experimental achievements,” *Meas Sci Technol*, vol.21, no. 5, p.054017, 2010.

[64] G. Dodel, “On the history of far-infrared (FIR) gas lasers: Thirty-five years of research and application,” *Infrared Phys Technol*, vol.40, no. 3, pp.127–139, Jun. 1999.

[65] W. He, C. R. Donaldson, L. Zhang, K. Ronald, P. McElhinney, and A. W. Cross, “High power wideband gyrotron backward wave oscillator operating towards the terahertz region,” *Phys Rev Lett*, vol.110, no. 16, p.165101, Apr. 2013.

[66] X. Xu, Y. Wei, F. Shen, H. Yin, J. Xu, Y. Gong, and W. Wang, “A watt-class 1-THz backward-wave oscillator based on sine waveguide,” *Phys Plasmas*, vol.19, no. 1, Jan. 2012.

[67] M. Mineo and C. Paoloni, “Corrugated rectangular waveguide tunable backward wave oscillator for terahertz applications,” *IEEE Trans Electron Devices*, vol.57, no. 6, pp.1481–1484, Jun. 2010.

[68] V. L. Bratman, Y. K. Kalynov, and V. N. Manuilov, “Large-orbit gyrotron operation in the terahertz frequency range,” *Phys Rev Lett*, vol.102, no. 24, p.245101, Jun. 2009.

[69] T. Idehara, T. Saito, I. Ogawa, S. Mitsudo, Y. Tatematsu, La Agusu, H. Mori, and S. Kobayashi, “Development of terahertz FU CW Gyrotron series for DNP,” *Appl Magn Reson*, vol.34, no. 3–4, pp.265–275, Aug. 2008.

[70] H. Ito, F. Nakajima, T. Furuta, and T. Ishibashi, “Continuous THz-wave generation using antenna-integrated uni-travelling-carrier photodiodes,” *Semicond Sci Technol*, vol.20, no. 7, p.S191, 2005.

[71] N. Shimizu, N. Watanabe, T. Furuta, and T. Ishibashi, “InP-InGaAs uni-traveling-carrier photodiode with improved 3-dB bandwidth of over 150 GHz,” *IEEE Photonics Technology Letters*, vol.10, no. 3, pp.412–414, Mar. 1998.

[72] M. Asada and S. Suzuki, “Terahertz Emitter Using Resonant-Tunneling Diode and Applications,” *Sensors 2021, Vol. 21, Page 1384*, vol.21, no. 4, p.1384, Feb. 2021.

[73] S. Komiyama, “Far-Infrared Emission from Population-Inverted Hot-Carrier System in <math xmlns="http://www.w3.org/1998/Math/MathML" display="inline"><mi>p</mi></math>-Ge,” *Phys Rev Lett*, vol.48, no. 4, p.271, Jan. 1982.

[74] R. Köhler, A. Tredicucci, F. Beltram, H. E. Beere, E. H. Linfield, A. G. Davies, D. A. Ritchie, R. C. Iotti, and F. Rossi, “Terahertz semiconductor-heterostructure laser,” *Nature 2002 417:6885*, vol.417, no. 6885, pp.156–159, May 2002.

[75] Y. Jin, Y. Jin, J. L. Reno, and S. Kumar, “Phase-locked terahertz plasmonic laser array with 2 W output power in a single spectral mode,” *Optica, Vol. 7, Issue 6, pp. 708-715*, vol.7, no. 6, pp.708–715, Jun. 2020.

[76] L. H. Li, L. Chen, J. R. Freeman, M. Salih, P. Dean, A. G. Davies, and E. H. Linfield, “Multi-Watt high-power THz frequency quantum cascade lasers,” *Electron Lett*, vol.53, no. 12, pp.799–800, Jun. 2017.

[77] A. Khalatpour, A. K. Paulsen, C. Deimert, Z. R. Wasilewski, and Q. Hu, “High-power portable terahertz laser systems,” *Nature Photonics 2020 15:1*, vol.15, no. 1, pp.16–20, Nov. 2020.

[78] B. S. Williams, “Terahertz quantum-cascade lasers,” *Nature Photonics 2007 1:9*, vol.1, no. 9, pp.517–525, Sep. 2007.

[79] K. Fujita, “Room temperature terahertz nonlinear quantum cascade lasers and their applications,” *International Conference on Infrared, Millimeter, and Terahertz Waves, IRMMW-THz*, vol.2020-November, pp.329–330, Nov. 2020.

[80] K. Fujita, S. Jung, Y. Jiang, J. H. Kim, A. Nakanishi, A. Ito, M. Hitaka, T. Edamura, and M. A. Belkin, “Recent progress in terahertz difference-frequency quantum cascade laser sources,” *Nanophotonics*, vol.7, no. 11, pp.1795–1817, Nov. 2018.

[81] Q. Lu and M. Razeghi, “Recent Advances in Room Temperature, High-Power Terahertz Quantum Cascade Laser Sources Based on Difference-Frequency Generation,” *Photonics 2016, Vol. 3, Page 42*, vol.3, no. 3, p.42, Jul. 2016.

[82] M. A. Belkin, F. Capasso, A. Belyanin, D. L. Sivco, A. Y. Cho, D. C. Oakley, C. J. Vineis, and G. W. Turner, “Terahertz quantum-cascade-laser source based on intracavity difference-frequency generation,” *Nature Photonics 2007 1:5*, vol.1, no. 5, pp.288–292, May 2007.

[83] S. Banerjee, “THz Solid-State Source Based on IMPATT Devices,” *Terahertz Biomedical and Healthcare Technologies: Materials to Devices*, pp.1–41, Jan. 2020.

[84] J. Nishizawa, P. Płotka, T. Kurabayashi, and H. Makabe, “706-GHz GaAs CW fundamental-mode TUNNETT diodes fabricated with molecular layer epitaxy,” *physica status solidi c*, vol.5, no. 9, pp.2802–2804, Jul. 2008.

[85] H. Eisele and R. Kamoua, “Submillimeter-wave InP Gunn devices,” *IEEE Trans Microw Theory Tech*, vol.52, no. 10, pp.2371–2378, Oct. 2004.

[86] H. Eisele, “480GHz oscillator with an InP Gunn device,” *Electron Lett*, vol.46, no. 6, pp.422–423, 2010.

[87] W. R. Deal, X. B. Mei, V. Radisic, K. Leong, S. Sarkozy, B. Gorospe, J. Lee, P. H. Liu, W. Yoshida, J. Zhou, M. Lange, J. Uyeda, and R. Lai, "Demonstration of a 0.48 THz amplifier module using InP HEMT transistors," *IEEE Microwave and Wireless Components Letters*, vol.20, no. 5, pp.289–291, May 2010.

[88] X. Mei, W. Yoshida, M. Lange, J. Lee, J. Zhou, P. H. Liu, K. Leong, A. Zamora, J. Padilla, S. Sarkozy, R. Lai, and W. R. Deal, "First Demonstration of Amplification at 1 THz Using 25-nm InP High Electron Mobility Transistor Process," *IEEE Electron Device Letters*, vol.36, no. 4, pp.327–329, Apr. 2015.

[89] J. Yun, J. Kim, D. Yoon, and J. S. Rieh, "645-GHz InP heterojunction bipolar transistor harmonic oscillator," *Electron Lett*, vol.53, no. 22, pp.1475–1477, Oct. 2017.

[90] J. Yun, J. Kim, and J. S. Rieh, "A 280-GHz 10-dBm Signal Source Based on InP HBT Technology," *IEEE Microwave and Wireless Components Letters*, vol.27, no. 2, pp.159–161, Feb. 2017.

[91] J. Yun, D. Yoon, H. Kim, and J. S. Rieh, "300-GHz InP HBT oscillators based on common-base cross-coupled topology," *IEEE Trans Microw Theory Tech*, vol.62, no. 12, pp.3053–3064, Dec. 2014.

[92] W. Steyaert and P. Reynaert, "A 0.54 THz signal generator in 40 nm bulk CMOS with 22 GHz tuning range and integrated planar antenna," *IEEE J Solid-State Circuits*, vol.49, no. 7, pp.1617–1626, 2014.

[93] Y. Koyama, R. Sekiguchi, and T. Ouchi, "Oscillations up to 1.40 THz from resonant-tunneling-diode-based oscillators with integrated patch antennas," *Applied Physics Express*, vol.6, no. 6, Jun. 2013.

[94] M. Feiginov, H. Kanaya, S. Suzuki, and M. Asada, "Operation of resonant-tunneling diodes with strong back injection from the collector at frequencies up to 1.46 THz," *Appl Phys Lett*, vol.104, no. 24, Jun. 2014.

[95] M. Feiginov, C. Sydlo, O. Cojocari, and P. Meissner, "Resonant-tunnelling-diode oscillators operating at frequencies above 1.1 THz," *Appl Phys Lett*, vol.99, no. 23, Dec. 2011.

[96] E. R. Brown, J. R. Söderström, C. D. Parker, L. J. Mahoney, K. M. Molvar, and T. C. McGill, "Oscillations up to 712 GHz in InAs/AlSb resonant-tunneling diodes," *Appl Phys Lett*, vol.58, no. 20, pp.2291–2293, 1991.

[97] S. Suzuki, M. Asada, A. Teranishi, H. Sugiyama, and H. Yokoyama, "Fundamental oscillation of resonant tunneling diodes above 1 THz at room temperature," *Appl Phys Lett*, vol.97, no. 24, Dec. 2010.

[98] A. Al-Khalidi, K. H. Alharbi, J. Wang, R. Morariu, L. Wang, A. Khalid, J. M. L. Figueiredo, and E. Wasige, "Resonant Tunneling Diode Terahertz Sources with up to 1 mW Output Power in the J-Band," *IEEE Trans Terahertz Sci Technol*, vol.10, no. 2, pp.150–157, Mar. 2020.

[99] J. Lee, M. Kim, and K. Yang, "A 1.52 THz RTD Triple-Push Oscillator with a μw-Level Output Power," *IEEE Trans Terahertz Sci Technol*, vol.6, no. 2, pp.336–340, Mar. 2016.

[100] M. Reddy, S. C. Martin, A. C. Molnar, R. E. Muller, R. P. Smith, P. H. Siegel, M. J. Mondry, M. J. W. Rodwell, H. Kroemer, and S. J. Allen, "Monolithic Schottky-collector resonant tunnel diode oscillator arrays to 650 GHz," *IEEE Electron Device Letters*, vol.18, no. 5, pp.218–221, May 1997.

[101] M. Bezhko, S. Suzuki, and M. Asada, "Frequency increase in resonant-tunneling diode cavity-type terahertz oscillator by simulation-based structure optimization," *Jpn J Appl Phys*, vol.59, no. 3, p.032004, Mar. 2020.

[102] K. Kobayashi, S. Suzuki, F. Han, H. Tanaka, H. Fujikata, and M. Asada, "Analysis of a high-power resonant-tunneling-diode terahertz oscillator integrated with a rectangular cavity resonator," *Jpn J Appl Phys*, vol.59, no. 5, p.050907, May 2020.

[103] K. Tsuruda, Y. Nishida, T. Mukai, K. Terumoto, Y. Miyamae, Y. Oku, and K. Nakahara, "Development of Practical Terahertz Packages for Resonant Tunneling Diode Oscillators and Detectors," *2020 IEEE International Symposium on Radio-Frequency Integration Technology, RFIT 2020*, pp.193–195, Sep. 2020.

[104] S. Suzuki, M. Shiraishi, H. Shibayama, and M. Asada, "High-power operation of terahertz oscillators with resonant tunneling diodes using impedance-matched antennas and array configuration," *IEEE Journal on Selected Topics in Quantum Electronics*, vol.19, no. 1, pp.136–143, 2013.

[105] K. Kasagi, S. Suzuki, and M. Asada, "Large-scale array of resonant-tunneling-diode terahertz oscillators for high output power at 1 THz," *J Appl Phys*, vol.125, no. 15, Apr. 2019.

[106] R. Tsu and L. Esaki, "Tunneling in a finite superlattice," *Appl Phys Lett*, vol.22, no. 11, pp.562–564, Jun. 1973.

[107] L. L. Chang, L. Esaki, and R. Tsu, "Resonant tunneling in semiconductor double barriers," *Appl Phys Lett*, vol.24, no. 12, pp.593–595, Jun. 1974.

[108] M. Tsuchiya, H. Sakaki, and J. Yoshino, "Room Temperature Observation of Differential Negative Resistance in an AlAs/GaAs/AlAs Resonant Tunneling Diode," *Jpn J Appl Phys*, vol.24, no. 6A, p.L466, 1985.

[109] E. R. Brown, J. R. Söderström, C. D. Parker, L. J. Mahoney, K. M. Molvar, and T. C. McGill, "Oscillations up to 712 GHz in InAs/AlSb resonant-tunneling diodes," *Appl Phys Lett*, vol.58, no. 20, pp.2291–2293, May 1991.

[110] S. Suzuki, A. Teranishi, K. Hinata, M. Asada, H. Sugiyama, and H. Yokoyama, "Fundamental oscillation up to 831 GHz in GaInAs/AlAs resonant tuneling diode," *Conference Proceedings - International Conference on Indium Phosphide and Related Materials*, pp.192–195, 2009.

[111] S. Suzuki, M. Asada, A. Teranishi, H. Sugiyama, and H. Yokoyama, "Fundamental oscillation of resonant tunneling diodes above 1 THz at room temperature," *Appl Phys Lett*, vol.97, no. 24, Dec. 2010.

[112] H. Kanaya, H. Shibayama, R. Sogabe, S. Suzuki, and M. Asada, "Fundamental oscillation up to 1.31 THz in resonant tunneling diodes with thin well and barriers," *Applied Physics Express*, vol.5, no. 12, p.124101, Dec. 2012.

[113] M. Feiginov, H. Kanaya, S. Suzuki, and M. Asada, "1.46 THz RTD oscillators with strong back injection from collector," *International Conference on Infrared, Millimeter, and Terahertz Waves, IRMMW-THz*, Nov. 2014.

[114] T. Maekawa, H. Kanaya, S. Suzuki, and M. Asada, "Frequency increase in terahertz oscillation of resonant tunnelling diode up to 1.55 THz by reduced slot-antenna length," *Electron Lett*, vol.50, no. 17, pp.1214–1216, Aug. 2014.

[115] T. Maekawa, H. Kanaya, S. Suzuki, and M. Asada, "Oscillation up to 1.92 THz in resonant tunneling diode by reduced conduction loss," *Applied Physics Express*, vol.9, no. 2, p.024101, Feb. 2016.

[116] S. Kitagawa, S. Suzuki, and M. Asada, "Wide frequency-tunable resonant tunnelling diode terahertz oscillators using varactor diodes," *Electron Lett*, vol.52, no. 6, pp.479–481, Mar. 2016.

[117] S. Kitagawa, S. Suzuki, and M. Asada, "650-GHz resonant-tunneling-diode VCO with wide tuning range using varactor diode," *IEEE Electron Device Letters*, vol.35, no. 12, pp.1215–1217, Dec. 2014.

[118] M. Shiraishi, H. Shibayama, K. Ishigaki, S. Suzuki, M. Asada, H. Sugiyama, and H. Yokoyama, "High Output Power (∼400 μW) Oscillators at around 550 GHz Using Resonant Tunneling Diodes with Graded Emitter and Thin Barriers," *Applied Physics Express*, vol.4, no. 6, Jun. 2011.

[119] S. Suzuki, M. Shiraishi, H. Shibayama, and M. Asada, "High-power operation of terahertz oscillators with resonant tunneling diodes using impedance-matched antennas and array

configuration," *IEEE Journal on Selected Topics in Quantum Electronics*, vol.19, no. 1, pp.136–143, 2013.

[120] K. Kobayashi, S. Suzuki, F. Han, H. Tanaka, H. Fujikata, and M. Asada, "Analysis of a high-power resonant-tunneling-diode terahertz oscillator integrated with a rectangular cavity resonator," *Jpn J Appl Phys*, vol.59, no. 5, p.050907, May 2020.

[121] H. Fujikata, H. Tanaka, F. Han, A. Ishikawa, S. Suzuki, and M. Asada, "Terahertz Oscillator using Rectangular-Cavity Resonator and Large-Area RTD with Heat Dissipation Structure," *International Conference on Infrared, Millimeter, and Terahertz Waves, IRMMW-THz*, vol.2022-August, 2022.

[122] K. Kasagi, S. Suzuki, and M. Asada, "Large-scale array of resonant-tunneling-diode terahertz oscillators for high output power at 1 THz," *J Appl Phys*, vol.125, no. 15, Apr. 2019.

[123] Y. Koyama, Y. Kitazawa, K. Yukimasa, T. Uchida, T. Yoshioka, K. Fujimoto, T. Sato, J. Iba, K. Sakurai, and T. Ichikawa, "A High-Power Terahertz Source Over 10 mW at 0.45 THz Using an Active Antenna Array With Integrated Patch Antennas and Resonant-Tunneling Diodes," *IEEE Trans Terahertz Sci Technol*, 2022.

[124] S. Iwamatsu, Y. Nishida, M. Fujita, and T. Nagatsuma, "Terahertz coherent oscillator integrated with slot-ring antenna using two resonant tunneling diodes," *Applied Physics Express*, vol.14, no. 3, p.034001, Jan. 2021.

[125] K. Okamoto, K. Tsuruda, S. Diebold, S. Hisatake, M. Fujita, and T. Nagatsuma, "Terahertz Sensor Using Photonic Crystal Cavity and Resonant Tunneling Diodes," *J Infrared Millim Terahertz Waves*, vol.38, no. 9, pp.1085–1097, Sep. 2017.

[126] S. Kitagawa, M. Mizuno, S. Saito, K. Ogino, S. Suzuki, and M. Asada, "Frequency-tunable resonant-tunneling-diode terahertz oscillators applied to absorbance measurement," *Jpn J Appl Phys*, vol.56, no. 5, p.058002, May 2017.

[127] A. Dobroiu, Y. Shirakawa, S. Suzuki, M. Asada, and H. Ito, "Subcarrier Frequency-Modulated Continuous-Wave Radar in the Terahertz Range Based on a Resonant-Tunneling-Diode Oscillator," *Sensors 2020, Vol. 20, Page 6848*, vol.20, no. 23, p.6848, Nov. 2020.

[128] L. Li, W. Zhang, Y. Liang, S.-G. Choi, M. Han, Y.-H. Baek, al -, Q. Zhang, L. Ma, J. Ren, A. Dobroiu, R. Wakasugi, Y. Shirakawa, S. Suzuki, and M. Asada, "Amplitude-modulated continuous-wave radar in the terahertz range using lock-in phase measurement," *Meas Sci Technol*, vol.31, no. 10, p.105001, Jul. 2020.

[129] A. Dobroiu, R. Wakasugi, Y. Shirakawa, S. Suzuki, and M. Asada, "Absolute and Precise Terahertz-Wave Radar Based on an Amplitude-Modulated Resonant-Tunneling-Diode Oscillator," *Photonics 2018, Vol. 5, Page 52*, vol.5, no. 4, p.52, Nov. 2018.

[130] S. Diebold, K. Nishio, Y. Nishida, J. Y. Kim, K. Tsuruda, T. Mukai, M. Fujita, and T. Nagatsuma, "High-speed error-free wireless data transmission using a terahertz resonant tunnelling diode transmitter and receiver," *Electron Lett*, vol.52, no. 24, pp.1999–2001, Nov. 2016.

[131] N. Oshima, K. Hashimoto, S. Suzuki, and M. Asada, "Terahertz wireless data transmission with frequency and polarization division multiplexing using resonant-tunneling-diode oscillators," *IEEE Trans Terahertz Sci Technol*, vol.7, no. 5, pp.593–598, Sep. 2017.

[132] T. Miyamoto, A. Yamaguchi, and T. Mukai, "Terahertz imaging system with resonant tunneling diodes," *Jpn J Appl Phys*, vol.55, no. 3, p.032201, Mar. 2016.

[133] T. Tajika, Y. Kakutani, M. Mori, and K. Maezawa, "Experimental demonstration of strain detection using resonant tunneling delta-sigma modulation sensors," *Physica status solidi (A)*, vol.214, no. 3, p.1600548, 2017.

[134] K. Maezawa, T. Ito, and M. Mori, "Delta-sigma modulation microphone sensors employing a resonant tunneling diode with a suspended microstrip resonator," *Sensor Review*, vol.40, no. 5, pp.535–542, 2020.

[135] K. Maezawa and M. Mori, "Possibilities of large voltage swing hard-type oscillators based on series-connected resonant tunneling diodes," *IEICE Transactions on Electronics*, vol.101, no. 5, pp.305–310, 2018.

[136] S. C. Martin, R. E. Muller, and R. P. Smith, "Bias Stabilization for Resonant Tunnel Diode Oscillators," *IEEE Microwave and Guided Wave Letters*, vol.5, no. 7, pp.219–221, 1995.

[137] C. Kidner, I. Mehdi, J. R. East, and G. I. Haddad, "Power and Stability Limitations of Resonant Tunneling Diodes," *IEEE Trans Microw Theory Tech*, vol.38, no. 7, pp.864–872, 1990.

[138] H. L. Swinney, "Observations of order and chaos in nonlinear systems," *Physica D*, vol.7, no. 1–3, pp.3–15, May 1983.

[139] C. Sparrow, "The Lorenz Equations: Bifurcations, Chaos, and Strange Attractors," vol.41, 1982.

[140] E. Glasner and B. Weiss, "Sensitive dependence on initial conditions," *Nonlinearity*, vol.6, no. 6, p.1067, Nov. 1993.

[141] J. S. Pethkar and A. M. Selvam, "Nonlinear Dynamics and Chaos: Applications for Prediction of Weather and Climate," *ArXiv*, p.physics/0104056, Apr. 2001.

[142] D. Lathrop, “Nonlinear Dynamics and Chaos: With Applications to Physics, Biology, Chemistry, and Engineering,” *Phys Today*, vol.68, no. 4, pp.54–55, Apr. 2015.

[143] S. Boccaletti, C. Grebogi, Y.-C. Lai, H. Mancini, and D. Maza, “The control of chaos: theory and applications,” *Phys Rep*, vol.329, no. 3, pp.103–197, 2000.

[144] T. Endo and T. Saito, “Chaos in electrical and electronic circuits and systems,” *IEICE TRANSACTIONS (1976-1990)*, vol.73, no. 6, pp.763–771, 1990.

[145] C. P. Silva and A. M. Young, “Introduction to chaos-based communications and signal processing,” 2000 IEEE Aerospace Conference. Proceedings (Cat. No. 00TH8484), vol.1, pp.279–299, 2000.

[146] E. Yavuz, R. Yazıcı, M. C. Kasapbaşı, and E. Yamaç, “A chaos-based image encryption algorithm with simple logical functions,” *Computers & Electrical Engineering*, vol.54, pp.471–483, 2016.

[147] A. Basiri, N. Behnam, R. De Rooij, L. Hochstein, L. Kosewski, J. Reynolds, and C. Rosenthal, “Chaos engineering,” *IEEE Softw*, vol.33, no. 3, pp.35–41, 2016.

[148] K. Aihara and R. Katayama, “Chaos engineering in Japan,” *Commun ACM*, vol.38, no. 11, pp.103–107, 1995.

[149] R. Katayama, Y. Kajitani, K. Kuwata, and Y. Nishida, “Developing tools and methods for applications incorporating neuro, fuzzy and chaos technology,” *Comput Ind Eng*, vol.24, no. 4, pp.579–592, 1993.

[150] K. Aihara, “Chaos engineering and its application to parallel distributed processing with chaotic neural networks,” *Proceedings of the IEEE*, vol.90, no. 5, pp.919–930, 2002.

[151] X. Zang, S. Iqbal, Y. Zhu, X. Liu, and J. Zhao, “Applications of chaotic dynamics in robotics,” *Int J Adv Robot Syst*, vol.13, no. 2, p.60, 2016.

[152] J. L. P. Felix, E. L. Silva, J. M. Balthazar, A. M. Tusset, A. M. Bueno, and R. Brasil, “On nonlinear dynamics and control of a robotic arm with chaos,” MATEC Web of Conferences, vol.16, p.05002, 2014.

[153] U. Nehmzow and K. Walker, “Quantitative description of robot–environment interaction using chaos theory,” *Rob Auton Syst*, vol.53, no. 3–4, pp.177–193, 2005.

[154] J. Yu and J. Yu, “Application of Chaotic Encryption Technology in Terahertz Communication,” *Broadband Terahertz Communication Technologies*, pp.235–244, 2021.

[155] D. R. Gulevich, V. P. Koshelets, and F. V Kusmartsev, “Bridging the terahertz gap for chaotic sources with superconducting junctions,” *Phys Rev B*, vol.99, no. 6, p.060501, 2019.

[156] E. A. Sobakinskaya, A. L. Pankratov, and V. L. Vaks, "Dynamics of a quantum two-level system under the action of phase-diffusion field," *Phys Lett A*, vol.376, no. 4, pp.265–269, 2012.

[157] E. Sobakinskaya, V. L. Vaks, N. Kinev, M. Ji, M. Y. Li, H. B. Wang, and V. P. Koshelets, "High-resolution terahertz spectroscopy with a noise radiation source based on high-Tc superconductors," *J Phys D Appl Phys*, vol.50, no. 3, p.035305, 2016.

[158] V. L. Vaks, E. G. Domracheva, M. B. Chernyaeva, S. I. Pripolzin, L. S. Revin, I. V Tretjyakov, V. A. Anfertev, and A. A. Yablokov, "Methods and approaches of high resolution spectroscopy for analytical applications," *Opt Quantum Electron*, vol.49, pp.1–10, 2017.

[159] H. Sun, Z. Yang, N. V Kinev, O. S. Kiselev, Y. Lv, Y. Huang, L. Hao, X. Zhou, M. Ji, and X. Tu, "Terahertz spectroscopy of dilute gases using Bi 2 Sr 2 CaCu 2 O 8+ δ intrinsic Josephson-junction stacks," *Phys Rev Appl*, vol.8, no. 5, p.054005, 2017.

[160] H.-P. Ren, M. S. Baptista, and C. Grebogi, "Wireless communication with chaos," *Phys Rev Lett*, vol.110, no. 18, p.184101, 2013.

[161] S. Hayes, C. Grebogi, and E. Ott, "Communicating with chaos," *Phys Rev Lett*, vol.70, no. 20, p.3031, 1993.

[162] J. PETRŽELA, Z. HRUBOŠ, and T. GOTTHANS, "Modeling Deterministic Chaos Using Electronic Circuits.," *Radioengineering*, vol.20, no. 2, 2011.

[163] A. Semenov, "Reviewing the mathemetical models and electrical circuits of deterministic chaos transistor oscillators," 2016 International Siberian Conference on Control and Communications (SIBCON), pp.1–6, 2016.

[164] G. Chen and T. Ueta, Chaos in circuits and systems, vol.11. World Scientific, 2002.

[165] K. Aihara, "Chaos and its applications," *Procedia IUTAM*, vol.5, no. 0, pp.199–203, 2012.

[166] E. Ott, C. Grebogi, and J. A. Yorke, "Controlling chaos," *Phys Rev Lett*, vol.64, no. 11, p.1196, 1990.

[167] S. Hayes, C. Grebogi, E. Ott, and A. Mark, "Experimental control of chaos for communication," *Phys Rev Lett*, vol.73, no. 13, p.1781, 1994.

[168] L. Kocarev, K. S. Halle, K. Eckert, L. O. Chua, and U. Parlitz, "Experimental demonstration of secure communications via chaotic synchronization," *International Journal of Bifurcation and Chaos*, vol.2, no. 03, pp.709–713, 1992.

[169] K. Maezawa, Y. Kawano, Y. Ohno, S. Kishimoto, and T. Mizutani, "Direct observation of high-frequency chaos signals from the resonant tunneling chaos generator," *Jpn J Appl Phys*, vol.43, no. 8R, p.5235, 2004.

[170] K. Maezawa, Y. Komoto, S. Kishimoto, T. Mizutani, M. Takakusaki, and H. Nakata, "Controlling high-frequency chaos in resonant tunneling chaos generator circuits," *IEICE Electronics Express*, vol.2, no. 12, pp.368–372, 2005.

[171] Y. Ueda and N. Akamatsu, "Chaotically transitional phenomena in the forced negative-resistance oscillator," *IEEE Trans Circuits Syst*, vol.28, no. 3, pp.217–224, 1981.

[172] Y. Kawano, Y. Ohno, S. Kishimoto, K. Maezawa, and T. Mizutani, "High-speed operation of a novel frequency divider using resonant tunneling chaos circuit," *Jpn J Appl Phys*, vol.41, no. 2S, p.1150, 2002.

[173] Y. K. Y. Kawano, S. K. S. Kishimoto, K. M. K. Maezawa, and T. M. T. Mizutani, "Resonant tunneling chaos generator for high-speed/low-power frequency divider," *Jpn J Appl Phys*, vol.38, no. 11B, p.L1321, 1999.

[174] Y. Kawano, Y. Ohno, S. Kishimoto, K. Maezawa, T. Mizutani, and K. Sano, "88 GHz dynamic 2: 1 frequency divider using resonant tunnelling chaos circuit," *Electron Lett*, vol.39, no. 21, p.1, 2003.

[175] Y. K. Y. Kawano, S. K. S. Kishimoto, K. M. K. Maezawa, and T. M. T. Mizutani, "Robust operation of a novel frequency divider using resonant tunneling chaos circuit," *Jpn J Appl Phys*, vol.39, no. 6R, p.3334, 2000.

[176] J. N. Schulman, H. J. De Los Santos, and D. H. Chow, "Physics-based RTD current-voltage equation," *IEEE Electron Device Letters*, vol.17, no. 5, pp.220–222, 1996.

[177] A. Venkatesan, S. Parthasarathy, and M. Lakshmanan, "Occurrence of multiple period-doubling bifurcation route to chaos in periodically pulsed chaotic dynamical systems," *Chaos Solitons Fractals*, vol.18, no. 4, pp.891–898, 2003.

[178] N. Tufillaro, "An experimental approach to nonlinear dynamics and chaos," *ScienceOpen Preprints*, 2024.

[179] A. M. Fraser and H. L. Swinney, "Independent coordinates for strange attractors from mutual information," *Phys Rev A (Coll Park)*, vol.33, no. 2, p.1134, 1986.

[180] David. Ruelle, "Chaotic evolution and strange attractors : the statistical analysis of time series for deterministic nonlinear systems," p.96, 1989.

[181] C. K. Volos, I. M. Kyprianidis, and I. N. Stouboulos, "Experimental study of a nonlinear circuit described by Duffing's equation," 2006.

[182] J.-C. Roux, R. H. Simoyi, and H. L. Swinney, "Observation of a strange attractor," *Physica D*, vol.8, no. 1–2, pp.257–266, 1983.

[183] A. Wolf, J. B. Swift, H. L. Swinney, and J. A. Vastano, "Determining Lyapunov exponents from a time series," *Physica D*, vol.16, no. 3, pp.285–317, 1985.

[184] S. Ramo, J. R. Whinnery, and T. Van Duzer, Fields and waves in communication electronics. John Wiley & Sons, 1994.

[185] D. M. Pozar, "Microwave engineering, johnwiley & sons," *Inc., New York*, 2005.

[186] D. K. Cheng, Field and wave electromagnetics. Pearson Education India, 1989.

[187] J. N. Blakely, L. Illing, and D. J. Gauthier, "High-Speed Chaos in an Optical Feedback System With Flexible Timescales," *IEEE J Quantum Electron*, vol.40, no. 3, pp.299–305, Mar. 2004.

[188] V. Dronov, M. R. Hendrey, T. M. Antonsen, and E. Ott, "Communication with a chaotic traveling wave tube microwave generator," *Chaos*, vol.14, no. 1, pp.30–37, 2004.

[189] V. S. Udaltsov, L. Larger, J. P. Goedgebuer, M. W. Lee, E. Genin, and W. T. Rhodes, "Bandpass chaotic dynamics of electronic oscillator operating with delayed nonlinear feedback," *IEEE Transactions on Circuits and Systems I: Fundamental Theory and Applications*, vol.49, no. 7, pp.1006–1009, Jul. 2002.

[190] A. N. Sharkovsky, "Chaos from a time-delayed Chua's circuit," *IEEE Transactions on Circuits and Systems I: Fundamental Theory and Applications*, vol.40, no. 10, pp.781–783, 1993.

[191] J. N. Blakely and N. J. Corron, "Experimental observation of delay-induced radio frequency chaos in a transmission line oscillator," *Chaos: An Interdisciplinary Journal of Nonlinear Science*, vol.14, no. 4, pp.1035–1041, 2004.

[192] K. Ozawa, K. Isogai, H. Nakano, and H. Okazaki, "Formal Chaos existing conditions on a transmission line circuit with a piecewise linear resistor," *Applied Sciences*, vol.11, no. 20, p.9672, 2021.

[193] L. Corti, G. Miano, and L. Verolino, "Bifurcations and chaos in transmission lines," *ARCHIV FUER ELEKTROTECHNIK*, vol.79, pp.165–171, 1996.

[194] M. Asada and S. Suzuki, "Room-temperature oscillation of resonant tunneling diodes close to 2 THz and their functions for various applications," *J Infrared Millim Terahertz Waves*, vol.37, pp.1185–1198, 2016.

[195] S. R. Norsworthy, R. Schreier, G. C. Temes, and I. Circuits, "Delta-sigma data converters : theory, design, and simulation," 1997.

[196] R. Schreier and G. C. Temes, Understanding delta-sigma data converters, vol.74. IEEE press Piscataway, NJ, 2005.

[197] J. C. Candy, "A Use of Limit Cycle Oscillations to Obtain Robust Analog-to-Digital Converters," *IEEE Transactions on Communications*, vol.22, no. 3, pp.298–305, 1974.

[198] M. Z. Straayer and M. H. Perrott, "A 12-bit, 10-MHz bandwidth, continuous-time ΣΔ ADC with a 5-bit, 950-MS/s VCO-based quantizer," *IEEE J Solid-State Circuits*, vol.43, no. 4, pp.805–814, Jan. 2008.

[199] M. Park and M. H. Perrott, "A VCO-based analog-to-digital converter with second-order sigma-delta noise shaping," *Proceedings - IEEE International Symposium on Circuits and Systems*, pp.3130–3133, 2009.

[200] M. Voelker, S. Pashmineh, J. Hauer, and M. Ortmanns, "Current feedback linearization applied to oscillator based ADCs," *IEEE Transactions on Circuits and Systems I: Regular Papers*, vol.61, no. 11, pp.3066–3074, Nov. 2014.

[201] K. Lee, Y. Yoon, and N. Sun, "A Scaling-Friendly Low-Power Small-Area ΔΣ ADC with VCO-Based Integrator and Intrinsic Mismatch Shaping Capability," *IEEE J Emerg Sel Top Circuits Syst*, vol.5, no. 4, pp.561–573, Dec. 2015.

[202] S. Li, A. Sanyal, K. Lee, Y. Yoon, X. Tang, Y. Zhong, K. Ragab, and N. Sun, "Advances in voltage-controlled-oscillator-based δσ ADCs," *IEICE Transactions on Electronics*, vol.E102C, no. 7, pp.509–529, 2019.

[203] X.-L. Huang, "Analog and Digital Communications," *Encyclopedia of Wireless Networks*, pp.1–3, 2018.

[204] R. Dastres and M. Soori, "A Review in Advanced Digital Signal Processing Systems," *International Journal of Electrical and Computer Engineering*, Mar. 2021.

[205] R. K. Rao Yarlagadda, "Analog and digital signals and systems," *Analog and Digital Signals and Systems*, pp.1–540, 2010.

[206] C. E. Shannon, "Communication in the Presence of Noise," *Proceedings of the IRE*, vol.37, no. 1, pp.10–21, 1949.

[207] A. V Oppenheim and R. W. Schafer, "Digital Signal Processing Prentice-Hall," *Englewood Cliffs, NJ*, vol.19752, pp.26–30, 1975.

[208] J. G. Proakis, Digital signal processing: principles, algorithms, and applications, 4/E. Pearson Education India, 2007.

[209] R. G. Lyons, Understanding digital signal processing, 3/E. Pearson Education India, 1997.

[210] W. Kester, Data conversion handbook. Newnes, 2005.

[211] M. J. M. Pelgrom, "Analog-to-Digital Conversion," *Analog-to-Digital Conversion*, pp.325–418, 2013.

[212] B. Razavi, "Principles of data conversion system design," *(No Title)*, 1994.

[213] A. Papoulis, “Generalized Sampling Expansion,” *IEEE Trans Circuits Syst*, vol.24, no. 11, pp.652–654, 1977.

[214] J. C. Candy, “A Use of Double Integration in Sigma Delta Modulation,” *IEEE Transactions on Communications*, vol.33, no. 3, pp.249–258, 1985.

[215] J. C. Candy, “Decimation for Sigma Delta Modulation,” *IEEE Transactions on Communications*, vol.34, no. 1, pp.72–76, 1986.

[216] R. Schreier and G. C. Temes, Understanding delta-sigma data converters, vol.74. IEEE press Piscataway, NJ, 2005.

[217] W. Kester, “Oversampling interpolating dacs,” *MT-017, tutorial documents, Analog Devices, Inc. available at http://www. analog. com/static/imported-files/tutorials/MT-017. pdf*, 2009.

[218] K. Maezawa, M. Mori, and H. Andoh, “Noise floor reduction in frequency delta-sigma modulation microphone sensors,” *Sensors*, vol.21, no. 10, May 2021.

[219] S. Li, A. Sanyal, K. Lee, Y. Yoon, X. Tang, Y. Zhong, K. Ragab, and N. Sun, “Advances in Voltage-Controlled-Oscillator-Based ΔΣ ADCs,” *IEICE Transactions on Electronics*, vol.E102.C, no. 7, pp.509–519, Jul. 2019.

[220] A. Iwata, N. Sakimura, M. Nagata, and T. Morie, “The architecture of delta sigma analog-to-digital converters using a voltage-controlled oscillator as a multibit quantizer,” *IEEE Transactions on Circuits and Systems II: Analog and Digital Signal Processing*, vol.46, no. 7, pp.941–945, Jul. 1999.

[221] M. Høvin, A. Olsen, T. S. Lande, and C. Toumazou, “Delta-sigma modulators using frequency-modulated intermediate values,” *IEEE J Solid-State Circuits*, vol.32, no. 1, pp.13–21, 1997.

[222] S. Fujino, Y. Mizuno, K. Takaoka, J. Nakano, M. Mori, and K. Maezawa, “Experimental demonstration of noise shaping in the digital microphone employing frequency ΔΣ modulation,” *IEICE Trans. Electron.(Jpn. Ed.)*, vol.96, pp.554–555, 2013.

[223] K. Maezawa, S. Fujino, T. Yamaoka, and M. Mori, “Delta-sigma modulation microphone sensors using microwave cavity resonator,” *Electron Lett*, vol.52, no. 20, pp.1651–1652, Sep. 2016.

[224] K. Maezawa, T. Ito, and M. Mori, “Delta-sigma modulation microphone sensors employing a resonant tunneling diode with a suspended microstrip resonator,” *Sensor Review*, vol.40, no. 5, pp.535–542, Oct. 2020.

[225] K. Maezawa and M. Mori, "Effects of oscillator phase noise on frequency delta sigma modulators with a high oversampling ratio for sensor applications," *IEICE Transactions on Electronics*, vol.104, no. 9, pp.463–466, Sep. 2021.

[226] B. Liu, "Transducers for Sound and Vibration-FEM Based Design," 2001.

[227] M. Asada and S. Suzuki, "Compact THz oscillators with resonant tunneling diodes and application to high-capacity wireless communications," *ICECom 2013 - Conference Proceedings: 21st International Conference on Applied Electromagnetics and Communications*, 2013.

[228] A. Oshiro, N. Nishigami, T. Yamamoto, Y. Nishida, J. Webber, M. Fujita, and T. Nagatsuma, "PAM4 48-Gbit/s wireless communication using a resonant tunneling diode in the 300-GHz band," *IEICE Electronics Express*, vol.19, no. 2, pp.20210494–20210494, Jan. 2022.

[229] R. M. Abdallah, A. A. S. Dessouki, and M. H. Aly, "The Resonant Tunneling Diode characterization for high frequency communication systems," *Microelectronics J*, vol.75, pp.1–14, May 2018.

[230] D. Cimbri, J. Wang, A. Al-Khalidi, and E. Wasige, "Resonant Tunneling Diodes High-Speed Terahertz Wireless Communications -A Review," *IEEE Trans Terahertz Sci Technol*, vol.12, no. 3, pp.226–244, May 2022.

[231] B. Ferguson and X. C. Zhang, "Materials for terahertz science and technology," *Nature Materials 2002 1:1*, vol.1, no. 1, pp.26–33, Sep. 2002.

[232] Ruth M Woodward, Bryan E Cole, Vincent P Wallace, Richard J Pye, Donald D Arnone, Edmund H Linfield, and Michael Pepper, "Terahertz pulse imaging in reflection geometry of human skin cancer and skin tissue," *Phys Med Biol*, vol.47, no. 21, p.3853, 2002.

[233] M. Brucherseifer, M. Nagel, P. Haring Bolivar, H. Kurz, A. Bosserhoff, and R. Büttner, "Label-free probing of the binding state of DNA by time-domain terahertz sensing," *Appl Phys Lett*, vol.77, no. 24, pp.4049–4051, Dec. 2000.

[234] S. Hunsche, M. Koch, I. Brener, and M. C. Nuss, "THz near-field imaging," *Opt Commun*, vol.150, no. 1–6, pp.22–26, May 1998.

[235] E. Castro-Camus, M. Koch, and D. M. Mittleman, "Recent advances in terahertz imaging: 1999 to 2021," *Applied Physics B 2021 128:1*, vol.128, no. 1, pp.1–10, Dec. 2021.

[236] H. X. Liu, J. Q. Yao, Y. Y. Wang, D. G. Xu, and Y. X. He, "Review of THz near-field imaging," *Journal of Infrared and Millimeter Waves, Vol. 35, Issue 3, pp. 300 - 309*, vol.35, no. 3, p.300, Jun. 2016.

[237] M. Tabib-Azar, T. Zhang, and S. R. LeClair, "Self-oscillating evanescent microwave probes for nondestructive evaluations of materials," *IEEE Trans Instrum Meas*, vol.51, no. 5, pp.1126–1132, Oct. 2002.

[238] S. Diebold, K. Tsuruda, J.-Y. Kim, T. Mukai, M. Fujita, and T. Nagatsuma, "A terahertz monolithic integrated resonant tunneling diode oscillator and mixer circuit," *https://doi.org/10.1117/12.2225209*, vol.9856, pp.91–96, Apr. 2016.

[239] N. V. Alkeev, S. V. Averin, A. A. Dorofeev, N. B. Gladysheva, and M. Y. Torgashin, "GaAs/AlAs resonant-tunneling diode for subharmonic mixers," *Russian Microelectronics*, vol.39, no. 5, pp.331–339, Sep. 2010.

[240] Y. Yokoyama, Y. Ohno, S. Kishimoto, K. Maezawa, and T. Mizutani, "A delta-sigma analog-to-digital converter using resonant tunneling diodes," *Jpn J Appl Phys*, vol.40, no. 10A, p.L1005, 2001.

[241] K. Maezawa, M. Sakou, W. Matsubara, and T. Mizutani, "Resonant tunnelling delta sigma modulator suitable for high-speed operation," *norma*, vol.60, no. 80, p.100, 2006.

[242] K. Maezawa and T. Mizutani, "InP-based resonant tunnelnig diode/HEMT integrated circuits for ultrahigh-speed operation," 2006 International Conference on Indium Phosphide and Related Materials Conference Proceedings, pp.252–257, 2006.

[243] K. M. K. Maezawa, H. M. H. Matsuzaki, T. A. T. Akeyoshi, J. O. J. Osaka, M. Y. M. Yamamoto, and T. O. T. Otsuji, "A novel delayed flip-flop circuit using resonant tunneling logic gates," *Jpn J Appl Phys*, vol.37, no. 2B, p.L212, 1998.

[244] H. Matsuzaki, H. Fukuyama, and T. Enoki, "Analysis of transient response and operating speed of MOBILE," *IEEE Trans Electron Devices*, vol.51, no. 4, pp.616–622, Apr. 2004.

[245] Y. Nishida, N. Nishigami, S. Diebold, J. Kim, M. Fujita, and T. Nagatsuma, "Terahertz coherent receiver using a single resonant tunnelling diode," *Scientific Reports 2019 9:1*, vol.9, no. 1, pp.1–9, Dec. 2019.

[246] W. Chen, J. Sun, S. Gao, J. J. Cheng, J. Wang, and Y. Todo, "Using a single dendritic neuron to forecast tourist arrivals to Japan," *IEICE Trans Inf Syst*, vol.E100D, no. 1, pp.190–202, Jan. 2017.

[247] F. Takens, "Detecting strange attractors in turbulence," Dynamical Systems and Turbulence, Warwick 1980: proceedings of a symposium held at the University of Warwick 1979/80, pp.366–381, 2006.

[248] P. Grassberger and I. Procaccia, "Estimation of the Kolmogorov entropy from a chaotic signal," *Phys Rev A (Coll Park)*, vol.28, no. 4, p.2591, Oct. 1983.

[249] H. D. I. Abarbanel, "Analysis of Observed Chaotic Data," 1996.

[250] P. Shang, X. Na, and S. Kamae, “Chaotic analysis of time series in the sediment transport phenomenon,” *Chaos Solitons Fractals*, vol.41, no. 1, pp.368–379, Jul. 2009.

[251] I. K. Yakasai, P. E. Abas, and F. Begum, “Review of porous core photonic crystal fibers for terahertz waveguiding,” *Optik (Stuttg)*, vol.229, p.166284, Mar. 2021.

[252] M. Asada and S. Suzuki, “Terahertz Emitter Using Resonant-Tunneling Diode and Applications,” *Sensors 2021, Vol. 21, Page 1384*, vol.21, no. 4, p.1384, Feb. 2021.

[253] K. Maezawa, “Resonant Tunneling Diodes,” *Wiley Encyclopedia of Electrical and Electronics Engineering*, pp.1–7, Sep. 2014.

Appendix A: RTD Fabrication process

	Material			Thicness(nm)	(Å)	(Å)	(Å)	Si-diping(㎝)	備考
20	In 0.5	Ga 0.5	As	25.0	250			10*10 19	
19	In 0.5	Ga 0.5	As	80.0	800			10*10 18	
18	In 0.53	Ga 0.47	As	1.5	15			undoped	
17	Al	As		1.6	16			undoped	
16	In0.53	Ga0.47	As	1.3	13			undoped	RTD
15	In	As		1.8	18	2956		undoped	layer
14	In0.53	Ga0.47	As	1.3	13			undoped	
13	Al	As		1.6	16			undoped	
12	In0.53	Ga.47	As	1.5	15			undoped	
11	In0.53	Ga0.47	As	80.0	800		5726	10*10 18	
10	In0.53	Ga0.47	As	100.0	1000			10*10 19	
9	Al	As		2.0	20	20		undoped	
8	In0.53	Ga0.47	As	20.0	200			10*10 19	
7	In0.49	Al0.51	As	15.0	150			10*10 19	
6	In0.52	Al0.48	As	20.0	200			undoped	HEMT
5	In0.49	Al0.51	As	3.0	30	2750		10*10 19	layer
4	In0.52	Al0.48	As	2.0	20	1750		undoped	
3	In0.53	Ga0.47	As	15.0	150			undoped	
2	In0.52	Al0.48	As	200.0	2000			undoped	

Layers details of the used Substrate.

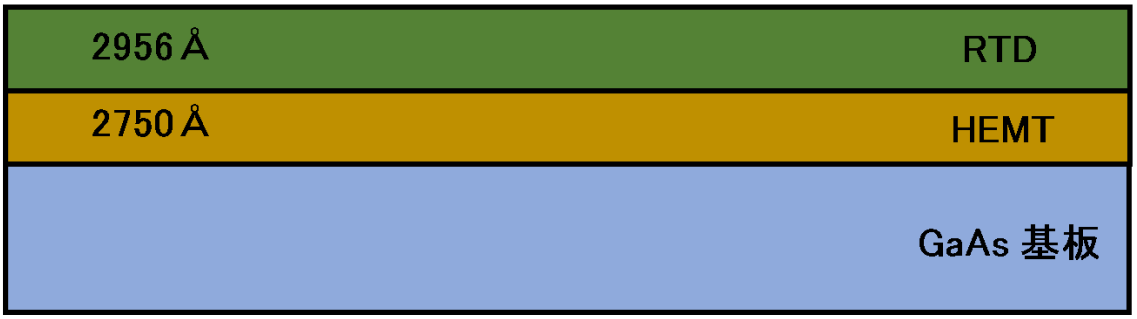

Cross-sectional view of the substrate

Process

1	TRENCH Layer 1
1.1	Substrate Cutting and Numbering
1.2	Substrate cleaning (lead dummy, 2 main boards, etching rate measurement)
1.2.1	Acetone Ultrasonic Cleaning Low 5 min room temperature
1.2.2	Blow N_2
1.2.3	Semicoclean Ultrasonic Cleaning Low 5 min room temperature (Only at the beginning will it be strongly cleaned with Semicoclean ultrasound)
1.2.4	Rinse 3 tanks 5 sec 5 sec 60 sec
1.2.5	Blow N_2
1.2.6	Electric furnace dry bake 130 °C 5 min (dry)
1.3	Positive resist coating on dummy substrates and main substrates
1.3.1	Blow N_2 2000 rpm 10 sec (sample surface clean)
1.3.2	OAP coating 5000 rpm 50 sec (resist adhesion)
1.3.3	S1805 Dispensing 5000 rpm 50 sec
1.3.4	Pre-bake 115 °C 1 min
1.3.5	Exposure File Name: RTDWB3R1 L0 18 mW 100 %
1.3.6	PEB bake : 115 °C 1 min
1.3.7	Developed 2 min20 sec CD-26Developer
1.3.8	Rinse 3 tanks 5 sec 5 sec 60 sec
1.3.9	Blow N_2
1.3.10	Host bake 115 °C 1 min (liquid dry)
1.3.11	Microscopic observation (longitudinal and horizontal dimension measurement)
1.4	Etching rate measurement (etching rate measurement sample)
1.4.1	S1805 Application Brush Coating
1.4.2	Pre-bake 115 °C 1 min
1.4.3	Pre-etching Etching solution$H_2SO_4 : H_2O_2 : H_2O = (1:10:1) \times 1/30$ 2 min49 sec (4726 Å sharpening) Etching temperature with glass thermometer 20 °C Fluorescent light
1.4.4	Rinse 3 tanks 5 sec 5 sec 60 sec
1.4.5	Blow N_2
1.4.6	Prior resist removal (etching rate measurement sample)
1.4.7	Acetone Spray
1.4.8	Acetone Ultrasonic Cleaning Low 5min Room Temperature
1.4.9	Blow N_2
1.4.10	Leading step measurement Etched step measurement
1.4.11	Find the actual etching time
1.5	Cleaning of dummy boards and main substrates
1.5.1	Descum ashing (resist residue removal at low temperatures) (Room temperature: RT 3 min 500 cc/min)
1.5.2	Semicoclean Cleaning 1 min Room Temperature

1.5.3	Rinse 3 tanks 5 sec 5 sec 60 sec
1.5.4	Blow N_2
1.6	Etching of dummy substrates and main substrates
1.6.1	etching Etching solution$H_2SO_4 : H_2O_2 : H_2O = (1:10:1) \times 1/30$ 2 min49 sec (4726 Å sharpening) Etching temperature with glass thermometer 20 °C Fluorescent light
1.6.2	Rinse 3 tanks 5 sec 5 sec 60 sec
1.6.3	Blow N_2
1.6.4	Resist removal of dummy substrates and main substrates
1.6.5	Acetone Spray
1.6.6	Acetone Ultrasonic Cleaning Low 5 min room temperature
1.6.7	Blow N_2
1.6.8	Microscopic observation (longitudinal and horizontal dimension measurement)
1.6.9	Ashing (resist removal with high-temperature ozone) (80 ℃ 10 min 500 cc/min)
1.6.10	Microscopic observation (longitudinal and horizontal dimension measurement)
1.6.11	Step measurement (etching rate measurement sample)
2	RESIST HB1 (Resist Hard Bake) Layer 2
2.1	Cleaning of dummy boards and main substrates
2.1.2	Acetone Ultrasonic Cleaning Low 5 min room temperature
2.1.3	Blow N_2
2.1.4	Semicoclean Cleaning 1 min Room Temperature
2.1.5	Rinse 3 tanks 5 sec 5 sec 60 sec
2.1.6	Blow N_2
2.1.7	Electric furnace dry bake 130 °C 5 min (dry)
2.2	Positive resist coating on dummy substrates and main substrates
2.2.1	Blow N_2 2000 rpm 10 sec (sample surface clean)
2.2.2	OAP coating 5000 rpm 50 sec (resist adhesion)
2.2.3	S1805 Dispensing 5000 rpm 50 sec
2.2.4	Pre-bake 115 °C 1 min
2.2.5	Exposure File Name: RTDWB3R1 L1 B&W Invert 18 mW 100 % Inverted 3000 μm
2.2.6	PEB bake: 115 °C 1 min
2.2.7	Develop 30 sec CD-26Developer after the pattern appears
2.2.8	Rinse 3 tanks 5 sec 5 sec 60 sec
2.2.9	Blow N_2
2.2.10	Host bake 115 °C 1 min (liquid dry)
2.2.11	Microscopic observation (longitudinal and horizontal dimension measurement)
2.3	Resist Hard Bake (Resist Cure)
2.3.1	Electric furnaces bake 200 °C 60 min
2.3.2	Microscopic observation

3	EMITTER Layer 3
3.1	Cleaning of dummy boards and main substrates
3.1.2	Acetone Ultrasonic Cleaning Low 5 min room temperature
3.1.3	Blow N_2
3.1.4	Semicoclean Cleaning 1 min Room Temperature
3.1.5	Rinse 3 tanks 5 sec 5 sec 60 sec
3.1.6	Blow N_2
3.1.7	Electric furnace dry bake 130 °C 5 min (dry)
3.2	Positive resist coating on dummy substrate and main substrate (double coating)
3.2.1	Blow N_2 2000 rpm 10 sec (sample surface clean)
3.2.2	OAP coating 5000 rpm 50 sec (resist adhesion)
3.2.3	PMGI SF6 dispensing 5000 rpm 50 sec
3.2.4	Pre-bake 250 °C 5 min
3.2.5	Allow to cool until it returns to room temperature
3.2.6	S1805 Dispensing 5000 rpm 50 sec
3.2.7	Pre-bake 115 °C 1 min
3.2.8	Exposure File Name: RTDWB3R1 L2 18 mW 100%
3.2.9	PEB bake: 115 °C 1 min
3.2.10	Developed 2 min20 sec CD-26Developer
3.2.11	Rinse 3 tanks 5 sec 5 sec 60 sec
3.2.12	Blow N_2
3.2.13	Host bake 115 °C 1 min (liquid dry)
3.2.14	Microscopic observation (longitudinal and horizontal dimension measurement)
3.3	Pre-deposition cleaning
3.3.1	Descum ashing (resist residue removal at low temperatures) (Room temperature: RT 3 min 500 cc/min)
3.3.2	Semicoclean Cleaning 1 min Room Temperature
3.3.3	Rinse 3 tanks 5 sec 5 sec 60 sec
3.3.4	Blow N_2
3.4	Deposition
3.4.1	Vapor deposition Ti: 200 Å / Au: 4000 Å (total 4200 Å)
3.4.2	Acetone wetting 12 h
3.5	Lift-off
3.5.1	Acetone spray (sprayed in lift-off beaker liquid)
3.5.2	Visual inspection (confirmation that vapor deposition is removed in acetone solution)
3.5.3	Remover PG Ultrasonic Cleaning Low 10 min Ambient Temperature (PMGI SF6 resist stripping of sacrificial tanks)
3.5.4	IPA Rinse Ultrasonic Cleaning Low 5 min Normal Temperature
3.5.5	Acetone Ultrasonic Cleaning Low 5 min room temperature
3.5.6	Blow N_2
3.5.7	Microscopic observation
3.5.8	Sintering 250 °C 5 min (Stabilization of contact resistance)

3.5.9	Microscopic observation
3.5.10	Step measurement (measurement of vapor deposition film thickness with Si dummy substrate 4200 Å:420 nm)
3.6	RIE
3.6.1	RIE (Reactive Ion Etching) Condition: 50 W O_2:20 ml/min 2 min
3.6.2	Microscopic observation
3.7	Mesa etching
3.7.1	Etching rate measurement (etching rate measurement sample)
3.7.2	S1805 Application Brush Coating
3.7.3	Pre-bake 115 °C 1 min
3.7.4	Pre-etching Etching solution$H_2SO_4 : H_2O_2 : H_2O = (1:10:1) \times 1/30$ 1 min15 sec (1956 Å sharpening) Etching temperature with glass thermometer 20 °C Fluorescent lamp light
3.7.5	Rinse 3 tanks 5 sec 5 sec 60 sec
3.7.6	Blow N_2
3.7.7	Leading step measurement Etched step measurement
3.7.8	Find the actual etching time
3.7.9	Cleaning of dummy boards and main substrates
3.7.10	Descum ashing (resist residue removal at low temperatures) (Room temperature: RT 3 min 500 cc/min)
3.7.11	Etching of dummy substrates and main substrates
3.7.12	etching Etching solution$H_2SO_4 : H_2O_2 : H_2O = (1:10:1) \times 1/30$ 1 min15 sec (1956 Å sharpening) Etching temperature with glass thermometer 20 °C Fluorescent lamp light
3.7.13	Rinse 3 tanks 5 sec 5 sec 60 sec
3.7.14	Blow N_2
3.7.15	Microscopic observation
3.7.16	Step measurement (etching rate measurement sample)
4	ISOLATION Layer 4
4.1	Cleaning of dummy boards and main substrates
4.1.1	Acetone Ultrasonic Cleaning Low 5 min room temperature
4.1.2	Blow N_2
4.1.3	Electric furnace dry bake 130 °C 5 min (dry)
4.2	Positive resist coating on dummy substrates and main substrates
4.2.1	Blow N_2 2000 rpm 10 sec (sample surface clean)
4.2.2	OAP coating 5000 rpm 50 sec (resist adhesion)
4.2.3	S1805 Dispensing 5000 rpm 50 sec
4.2.4	Pre-bake 115 °C 1 min
4.2.5	Exposure File Name: RTDWB3R1 L3 B&W Invert 18 mW 100 % Inverted 3000 μm
4.2.6	PEB bake: 115 °C 1 min

4.2.7	Develop 30 sec CD-26Developer after the pattern appears
4.2.8	Rinse 3 tanks 5 sec 5 sec 60 sec
4.2.9	Blow N_2
4.2.10	Host bake 115 °C 1 min (liquid dry)
4.2.11	Microscopic observation (longitudinal and horizontal dimension measurement)
4.3	Etching rate measurement (etching rate measurement sample)
4.3.1	S1805 Application Brush Coating
4.3.2	Pre-bake 115 °C 1 min
4.3.3	Pre-etching Etching solution$H_2SO_4 : H_2O_2 : H_2O = (1:10:1) \times 1/30$ 1 min49 sec (2750 Å sharpening) Etching temperature with glass thermometer 20 °C Fluorescent lamp lighting
4.3.4	Rinse 3 tanks 5 sec 5 sec 60 sec
4.3.5	Blow N_2
4.3.6	Prior resist removal (etching rate measurement sample)
4.3.7	Acetone Spray
4.3.8	Acetone Ultrasonic Cleaning Low 5 min room temperature
4.3.9	Blow N_2
4.3.10	Leading step measurement Etched step measurement
4.3.11	Find the actual etching time
4.4	Cleaning of dummy boards and main substrates
4.4.1	Descum ashing (resist residue removal at low temperatures) (Room temperature: RT 3 min 500 cc/min)
4.5	Etching of dummy substrates and main substrates
4.5.1	etching Etching solution$H_2SO_4 : H_2O_2 : H_2O = (1:10:1) \times 1/30$ 2 min49 sec (4726 Å sharpening) Etching temperature with glass thermometer 20 °C Fluorescent light
4.5.2	Rinse 3 tanks 5 sec 5 sec 60 sec
4.5.3	Blow N_2
4.5.4	Resist removal of dummy substrates and main substrates
4.5.5	Acetone Spray
4.5.6	Acetone Ultrasonic Cleaning Low 5 min room temperature
4.5.7	Blow N_2
4.5.8	Microscopic observation
4.5.9	Descum (resist residue removal at low temperatures) (50 ℃ 5 min 500 cc/min)
4.5.10	Microscopic observation
4.5.11	Step measurement (etching rate measurement sample)
5	COLLECTER L5
5.1	Cleaning of dummy boards and main substrates
5.1.1	Acetone Ultrasonic Cleaning Low 5 min room temperature
5.1.2	Blow N_2
5.1.3	Electric furnace dry bake 130 °C 5 min (dry)

5.2	Positive resist coating on dummy substrate and main substrate (double coating)
5.2.1	Blow N_2 2000 rpm 10 sec (sample surface clean)
5.2.2	OAP coating 5000 rpm 50 sec (resist adhesion)
5.2.3	PMGI SF6 dispensing 5000 rpm 50 sec
5.2.4	Pre-bake 250 °C 5 min
5.2.5	Allow to cool until it returns to room temperature
5.2.6	S1805 Dispensing 5000 rpm 50 sec
5.2.7	Pre-bake 115 °C 1 min
5.2.8	Exposure File Name: RTDWB3R1 L4 18 mW 100 %
5.2.9	PEB Bake: 115 °C 1min
5.2.10	Develop 30 sec CD-26Developer after the pattern appears
5.2.11	Rinse 3 tanks 5 sec 5 sec 60 sec
5.2.12	Blow N_2
5.2.13	Host bake 115 °C 1 min (liquid dry)
5.2.14	Microscopic observation (longitudinal and horizontal dimension measurement)
5.2.15	Pre-deposition cleaning
5.2.16	Death combing (resist residue removal at low temperatures) (Room temperature: RT 3 min 500 cc/min)
5.3	Deposition
5.3.1	Vapor deposition Ti: 200 Å / Au: 4000 Å (total 4200 Å)
5.3.2	Acetone wetting 12 h
5.4	Lift-off
5.4.1	Acetone spray (sprayed in lift-off beaker liquid)
5.4.2	Visual inspection (confirmation that vapor deposition is removed in acetone solution)
5.4.3	Remover PG Ultrasonic Cleaning Low 10 min Ambient Temperature (PMGI SF6 resist stripping of sacrificial tanks)
5.4.4	IPA Rinse Ultrasonic Cleaning 5min Normal Temperature
5.4.5	Acetone Ultrasonic Cleaning Low 5 min room temperature
5.4.6	Blow N_2
5.4.7	Microscopic observation
5.4.8	Sintering 250 °C 5 min (Stabilization of contact resistance)
5.4.9	Microscopic observation
5.4.10	Step measurement (measurement of vapor deposition film thickness with Si dummy substrate 4200 Å:420 nm)

Appendix B : Calculation of Lyapunov Exponent Using the Wolf Method

1. Introduction

The Lyapunov exponent measures the average rate at which consecutive trajectories converge or diverge in a dynamical system. It offers insight into both system stability and chaotic behavior. The Wolff method is an effective approach for determining the maximal Lyapunov exponent from a time series.

2. Methodology

The calculation of Largest Lyapunov exponent using Wolf method include following steps:

1. Prepare time series data
2. Time delay calculation using mutual information method
3. Embedding dimension calculation using Grassberger – Procaccia method
4. Phase space reconstruction based on Takens's theorem
5. Calculate largest Lyapunov exponent

3. Largest Lyapunov exponent calculation method using time series

The detail of calculations is discussed in the following section. This is adopted from [246].

5.1.2 Input time series data:

Assume x_t is a one-dimensional time series at time t (t = 1, 2, 3,...). First, the input x_t is normalized to the range of [0,1] using the following equation:

$$y_t = \frac{x_t - MIN(x_t)}{MAX(x_t) - MIN(x_t)}$$

Where y_t is the normalized data to address the issue of inconsistent values within time series data, and MAX (MIN) gives the vector's maximum (minimal) value.

5.1.3 Time delay, embedding dimension and phase space reconstruction:

Phase space reconstruction (PSR) is the basis of chaotic time series and is widely used in nonlinear system analysis. It is a theory that derives geometrical and topological information about dynamical attractors from observations. In order to analyze time series, Takens [247] introduced the delayed coordinate method of PSR. He also demonstrated how PSR may expand time series into an m-dimensional embedding space while maintaining the topology of chaotically attracted high-dimensional dynamical systems.

In PSR, two parameters, the delay τ and the embedding size m, are very important. In theory, any value of τ is suitable for determining the delay time. However, the appearance of the reconstructed attractor depends strongly on the choice of embedding lag. To reconstruct the phase space, appropriate embedding dimension (m) and delay (τ) are used. The Grassberger-

Procaccia algorithm [248] determines the embedding size m, whereas the mutual information function [179] calculates the time delay τ.

The value for which the mutual information has its first minimum is used to determine the time delay τ [68]. I(y, y_τ) is the mutual information between two time series: $y = \{y_{t_1}, y_{t_2}, \dots, y_{t_N}\}$, $y_\tau = \{y_{t_{1+\tau}}, y_{t_{2+\tau}}, \dots, y_{t_{N+\tau}}\}$. I(y, yτ) can be represented as

$$I(\tau) = I(y, y_\tau) = H(y) + H(y_\tau) - H(y, y_\tau)$$

where H(y) and H(y_τ) illustrates the entropy of y and y_τ respectively. H(y, y_τ) denotes the mutual entropy of y and yτ. Generally, the ideal delay time for PSR is often determined by taking the initial minimal mutual information.

After finding the time delay, the embedding dimension is computed using the Grassberger-Procaccia algorithm. Initially, the correlation integral C(r) is computed as follows:

$$C(r) = \frac{2}{N_m(N_m) - 1} \sum_{1 \le i \le j \le N_m} \varphi\left(r - |y_i - y_j|\right)$$

where Nm is equal to N − τ (m − 1), φ (·) is the Heaviside function, and r is the chosen radius. With each increase in the embedding dimension m, the correlative dimension D(m) (D(m) = ln(C(r))/ln(r)) rises and eventually approaches to a saturation value. The value at which D(m) initially obtains a stable value is the embedding dimension.

A matrix (P, T)′for the normalized time series yt, t = 1,..., N can be used to represent a reconstructed phase space as follow

$$P = \begin{pmatrix} y_1 & y_2 & \cdots & y_{N-1-\tau(m-1)} \\ y_{1+\tau} & y_{2+\tau} & \cdots & y_{N-1-\tau(m-2)} \\ & & \cdots & \\ y_{1+\tau(m-1)} & y_{2+\tau(m-1)} & \cdots & y_{N-1} \end{pmatrix}$$

$$T = \left(y_{2+\tau(m-1)}, y_{3+\tau(m-1)}, \cdots, y_N\right)$$

5.1.4 Largest Lyapunov exponent calculation:

The Lyapunov exponents of the time series, which can quantitatively describe the chaotic attractor, must be computed in order to determine whether the signal is chaotic or not. Lyapunov exponents define the rate at which minor perturbations increase or shrink in different directions in the orbital phase space. When the Lyapunov exponent is positive, the time series considered as chaotic [183]. In this study, the Wolf method [183] is used to calculate the maximum Lyapunov exponents of the chaotic time series. It is assumed that the initial time is t_0, the first reconstructed phase point is y_{t_0}, where the minimum length between y_{t_0} and the neighboring phase points is L_0. In the case where the time is t_1, $\grave{L_0} = \left\|y_{t_1} - y_{t_0}\right\|$, the distance $\grave{L_0} > \varepsilon$ has a positive threshold value determined by taking into account the evolution of the two phase points. We shall substitute $\grave{L_0}$ if we find another phase point, $y_{t_1}^1$, where $L^1 = \|y_{t_1} - y_{t_1}^1\| < \grave{L_0}$. This calculating method is ultimately carried out until y_t reaches the end of the time series y_N. As a result, the largest Lyapunov exponent can be determined as the function below.

$$\lambda_{max} = \frac{1}{t_m - t_0} \sum_{i=0}^{m} ln \frac{\grave{L_i}}{L_i}$$

In a chaotic system, we can only anticipate the time series over short intervals. In theory, the length of the intervals can be found using the reciprocal Lyapunov exponent [249], [250].

$$\Delta t = \frac{1}{\lambda_{max}}$$

When the largest Lyapunov exponent is greater than zero, the system becomes chaotic. If it is greater than one, the predictable limit is smaller than the sampling frequency. Therefore, the predictions of the chaotic time series are useful only in the case that the chaotic system exhibiting the largest Lyapunov exponent lies in the range of zero to one. Long-term forecasts become achievable when the positive exponent approaches zero.

Publication list

- **Journal paper**
  1. **Umer Farooq**, Masayuki Mori, Koichi Maezawa, "Experimental Characterization of Resonant Tunneling Chaos Generator Circuits in Microwave Frequency Range", IEICE Transactions on Electronics, E106-C NO. 5, 174-183, 2023 May. https://doi.org/10.1587/transele.2022ECP5037

  2. Koichi Maezawa, **Umer Farooq**, Masayuki Mori, "A Novel Displacement Sensor Based on a Frequency Delta-Sigma Modulator and its Application to a Stylus Surface Profiler", IEICE Transactions on Electronics, E106-C, NO. 9, 486-490, 2023 Sep. https://doi.org/10.1587/transele.2022ECS6013

  3. **Umer Farooq**, Masayuki Mori, Koichi Maezawa. " Strong nonlinear effects of a transmission line stub on resonant tunneling diode oscillators." IEICE Transactions on Electronics, E108-C, NO. 1, - , 2025 Jan. https://doi.org/10.1587/transele.2024ECS6002
- **International Conferences**
  1. **Umer Farooq**, Masayuki Mori, Koichi Maezawa. "A microwave chaos generator circuit employing a resonant tunneling diode.", 2nd International Electronic Conference - Enabling Nanoelectronics, session Integrated circuits MDPI: Basel, Switzerland, 1–31 October 2021.

  2. **Umer Farooq**, Masayuki Mori, and Koichi Maezawa, “A symmetric-type monostable-bistable transition logic element (SMOBILE) with frequency-based I/O isolation for THz-signal under-sampling”, 14th Topical Workshop on Heterostructure

Microelectronics (TWHM 2022), Hiroshima, Japan, 29 Aug – 1 Sep 2022. (Short Presentation & Poster Presentation)

3. **Umer Farooq**, Masayuki Mori, and Koichi Maezawa, "A frequency delta-sigma modulation (FDSM) based scanning near-field THz microscope employing a resonant tunneling diode (RTD) – Proposal and demonstration in microwave frequency range –", 15th Topical Workshop on Heterostructure Microelectronics (TWHM 2024), Miyagi, Japan, Aug 26-29, 2024. (Short Presentation & Poster Presentation)